Astrophysikalisches Institut Potsdam
Arbeitsgruppe “Magnetohydrodynamik”

INTERSTELLAR TURBULENCE DRIVEN BY MAGNETO-ROTATIONAL INSTABILITY

Dissertation
zur Erlangung des akademischen Grades
“doctor rerum naturalium”
(Dr. rer. nat.)
in der Wissenschaftsdisziplin Astrophysik

eingereicht an der
Mathematisch-Naturwissenschaftlichen Fakultät
der Universität Potsdam

von
Natalia Dziourkevitch

Potsdam, im Februar 2005

Contents

Introduction

Galaxies are among the most fascinating objects in the sky. Strong emission from structures built early in the history of the universe, such as quasi-stellar objects (QSO), give us some hints about the physical processes shaping young galaxies. Galaxies closer to us and evolved over a longer time scale show a variety of forms, interactions and active regions, resulting from long internal evolution and galaxy collisions. To obtain detailed observational information, huge investments went into powerful telescopes. But the more detailed these observations become, the more questions appear to be answered by theory. There is also a permanent growth of computing power for numerical experiments. This allows to include a growing number of physical processes acting on an extended range of scales.

There are no two identical spiral galaxies in the sky - every one shows us a different face and has its own individual history. It therefore becomes more and more difficult for an individual theoreticians to incorporate all the detected effects and details into one coherent large scale picture. Thus, a personal scientific contribution is just a small stone in the huge puzzle of the Universe.

Observations detect magnetic fields inside and outside the Milky Way, starting with globules ($\sim$ 1 parsec), filaments, clouds, superbubbles, spiral arms, nearby galaxies, superclusters, and ending with the Cosmological Universe's Background Surface at $\sim$ 8 Teraparsecs (Valleé 1997). This work is concerned with a common property of every galaxy – the galactic global magnetic field. It was observed to be of the same strength for both young and old galaxies. The magnetic fields are coupled to the interstellar matter (ISM) and may be one of the causes for the turbulence detected in the ISM.

In the first chapter I shall give a brief overview of the galactic global magnetic field properties. The dynamo mechanism (a well-known theoretical explanation of the global magnetic fields) will be briefly described. The success of dynamo-amplification of the magnetic fields depends on the properties of ISM. ISM phases and their distribution in a galactic disk, as well as the report about observed properties of the turbulent density, velocity and magnetic fields are therefore given. As a summary of the first chapter we shall formulate the motivation for a magneto-rotational instability (MRI) investigation in the galactic disk.

Chapter 2 is devoted to the description of observed rotation laws for the galaxies. The topic deserves our attention as far as the radial variation of galactic rotation is a cause for existence of MRI. Many years of galactic rotation law studies leave nevertheless many questions open, they will be discussed in this work.

In Chapter 3 we explain the physical mechanism of the magneto-rotational instability. We give the simplest derivation of an instability criterion for the MRI. Most of the previous results have been obtained for Keplerian disks. A summary of both linear study and local simulations is given.

In Chapter 4 we give the numerical code description. The magneto-hydrodynamical code ZeusMP has been used for 3D global simulations of the gaseous galactic disks. There are plenty of alternative codes, therefore we have to justify our choice for ZeusMP. The description of the model, boundary condition choice and numerical difficulties are discussed as well.

Chapters 5 and 6 contain the main results and the summary.

Chapter 1

Magnetic fields of spiral galaxies

1.1 Global magnetic fields

Each spiral galaxy has both unique features and others that are common with most other galaxies. Therefore, we shall distinguish between the features driven by a very specific (for a given galaxy) process and features created by a common physical mechanism. The common features are:

- magnetic field strength is $\simeq 10\ \mu\mathrm{G}$,
- magnetic spiral arms are parallel to optical ones (if the latter are clearly present),
- magnetic field lines have pitch angles from 10^{o} to 40^{o} (in plane),
- magnetic fields have mixed spiral structure (MSS) or axisymmetric spiral structure (ASS) (bisymmetric structure is reported only for M 81),
- evidence for the magnetic quadrupole (or the mixture of it with a dipole),
- magnetic fields are concentrated in the midplane,
- significant magnetic fields exist in the very young galaxies.

We derive most of the listed features from the radio observation data for nearby spiral galaxies, which are presented in Table 1.1 and Table 1.2 (R. Beck 2000). The magnetic field structures are given both for face-on and edge-on objects.

A theoretical finding of the physical mechanism for the fast magnetic field amplification is requested not only for nearby spiral galaxies. Magnetic fields of about $1\mu\mathrm{G}$ are observed in extremely young galaxies (Kronberg et al. 1992, Lesch & Hanasz 2003). The magnetic fields are required to be strongly amplified on short time-scales because of the observed magnetization of very young (0.5 Gyr) galaxies.

The amplitude of the magnetic field is a derived and not directly observed value. We use the fact that the energetic charged particles (cosmic rays) emit a

Table 1.1: Radio polarization observations and magnetic field structures of normal galaxies with low or moderate inclination (Beck 2000). Instruments: E: Effelsberg 100m; A: Australia Telescope Compact Array; V: Very Large Array; P: Parkes 64m; W: Westerbork Synthesis Radio Telescope. Notations: ASS: axisymmetric spiral structure (m=0 dynamo mode) dominates; BSS: bisymmetric spiral structure (m=1 dynamo mode) dominates; MSS: mixed modes

galaxy	wavelength [cm]	field structure
M33	E 21, 18, 11, 6, 2.8	spiral
M51	W 21, 6	
	E 6, 2.8	MSS, magneto-ionic halo,
	V 20,18,6	inter-arm fields
M81	E 6, 2.8	BSS+weaker ASS,
	V 20,6	inter-arm fields
M83	E 6, 2.8	MSS and $\parallel$ bar
	V 20,6, A 13	magnetic arms
M101	E 11, 6	spiral
NGC 1097	V 22, 18, 6, 3.5	$\parallel$ gas flow, nuclear spiral
NGC 1365	V 22, 18, 6, 3.5	$\parallel$ gas flow
NGC 1566	A 20, 13, 6	spiral, inter-arm fields
NGC 1672	A 20, 13, 6	spiral, inter-arm fields
NGC 2276	V 20,6	spiral, BSS?
NGC 2442	A 13, 6	spiral, $\parallel$ bar
NGC 2903	E 6, 2.8 , V 18, 20	spiral
NGC 2997	V 20, 6, 3.5, A 13	spiral, ASS in inner region
NGC 3521	E 2.8	spiral
NGC 3627	E 2.8	$\parallel$ dust line
	V 6, 3.5	anomalous magnetic arm
NGC 4254	E 6, 2.8 V 20, 6, 3.5	spiral, $\parallel$ compression region
NGC 4258	W+V 21 E 6, 2.8	$\parallel$ anomalous arm
	V 20, 6, 3.5	planar spiral jet?
NGC 4414	V 6, 3.5	spiral, MSS?
NGC 4449	E 6, 2.8	$\parallel$ optical filament
	V 6, 3.5	spiral
NGC 4535	V 22, 18, 6, 3.5	spiral
NGC 5055	E 2.8	spiral, $\parallel$ dust filaments
NGC 6822	E 6	isolated patches
NGC 6946	E 11, 6, 2.8	spiral,
	V 22, 18, 6, 3.5	MSS, magnetic arms
NGC 7479	V 22, 18, 6, 3.5	extra-planar spiral ‘jet’?
NGC 7552	A 6	spiral, $\perp$ bar
IC 10	E 6	$\parallel$ local compression region
IC 342	E 11, 6 V 20, 6, 3.5	ASS, magnetic spiral arms

Table 1.2: Radio polarization observations and magnetic field structures of (almost) edge-on galaxies (Beck 2000). (E, P, V, ASS, BSS: see Table 1.1)

galaxy	wavelength [cm]	field structure
M31	E 21, 11, 6	ASS (+ weaker BSS),
	V 20, 6	spiral (inner region)
M82	V 6, 3.6	halo, radial field
M104	V 20, 6	$\|\|$ disk
NGC 55	V 20	
NGC253	P 6	
	V 20, 6	$\|\|$ plane, ASS
	E 6, 2.8	spurs inclined to plane
NGC 891	V 20, 6	$\|\|$ spurs inclined to plane
	E 6, 2.8	
	W 49	
NGC 1808	V 20, 6	spurs $\perp$ plane
NGC 3079	V 6	extra-planar jet?
NGC 3628	V 20, 6	$\|\|$ plane
	E 6, 2.8	spurs inclined to plane
NGC 4565	V 20, 6	$\|\|$ plane
	E 6, 2.8	
NGC 4631	E 6, 2.8	$\|\|$ plane (outer region)
	V 20, 6	$\perp$ plane (inner region)
	V 22, 18	halo, dipolar field
NGC 4666	V 20, 6	halo, field inclined to plane
	E 6, 2.8	
NGC 4945	P 6	extensions $\perp$ plane
NGC 5775	V 6	$\|\|$ plane
NGC 5907	V 20	
	E 6	$\|\|$ plane
NGC 7331	V 20, 6	
	E 6, 2.8	almost $\|\|$ plane
Circinus	A 13, 6	$\perp$ northern plume

lot of energy while spiraling around the magnetic lines within a galaxy. An intensity of the synchrotron emission $j_{\rm sync}$ is measured directly and related to the strength of the magnetic field, $j_{\rm sync} \sim E_{\rm CR}B^2$. If the cosmic rays can be assumed to be in an equipartition with the magnetic fields, then by definition the cosmic ray energy density, $E_{\rm CR}$, is proportional to B^2. Therefore, the magnetic field strength is assumed to be proportional to the intensity as $B \sim j_{\rm sync}^{-4}$.

The energy density of the magnetic field $E_{\rm mag}$ (estimated from an equipartition with CR) is found to be in an equipartition with the turbulent kinetic energy density $E_{\rm T,kin}$. Therefore, for spiral galaxies we employ the widely accepted equipartition condition,

$$E_{\rm T,kin} \simeq E_{\rm mag} \simeq E_{\rm CR}. \tag{1.1}$$

Usually, it is justified to estimate the equipartition magnetic field

$$B_{\rm eq} = \sqrt{\mu_0 \rho}\, u_{\rm T}, \tag{1.2}$$

using the observed gas density ρ and the velocity dispersion $u_{\rm T} = \sqrt{\langle \boldsymbol{u}'^2 \rangle}$, which can be measured for a galaxy. For example, for $u_{\rm T} = 10{\rm km/s}$ and density $\rho = 10^{-24}{\rm g/cm^3}$ the equipartition field is $3.5 \times 10^{-6}{\rm G}$. Obviously, the magnetic fields are too weak to affect the galactic rotation, whereas the dynamical importance on the turbulence scales can not be neglected.

Synchrotron emission in a purely regular magnetic field should be totally polarized. In reality, the galactic magnetic fields have both mean and turbulent components, $\boldsymbol{B} = \boldsymbol{B}_{\rm reg} + \boldsymbol{B}_{\rm T}$. The degree of the synchrotron emission polarization is telling us about the contribution of the turbulent magnetic fields. Usually, $B_{\rm T}/B_{\rm reg} \sim 2$. Typically, the turbulent magnetic fields are dominating in the optical spiral arms, whereas the regular component is typically concentrated in the inter-arm regions (with rare exceptions).

The interpretation of the radio-polarization data of spiral galaxies reveals the existence of large-scale magnetic fields with very specific properties. Their explanation is of considerable interest. In particular, there is a problem of understanding the relation between the particle flow and the magnetic fields. We are looking forward to the next generation of radio telescopes, with 100 times increased sensitivity, which will present to us the full wealth of magnetic structures in galaxies. Fortunately, the power of supercomputers allow us to start already with the numerical simulations, in an attempt to explain some of the problems mentioned or even to predict some features to be observed in future with better resolution and sensitivity.

In spite of many similarities, each galaxy shows individual traits and complication of magnetic fields patterns (spurs, spiral arms, blobs, cross-arms and axial flows). Radio maps with higher resolution show now more details of the magnetic structures, which seemed to be much more coherent and regular on previous maps with less resolution.

1.1.1 Magnetic pitch angles and field strength

The pitch angle $p = \tan^{-1}(B_{\rm R}/B_\phi)$ reflects the ratio of the radial to the toroidal magnetic field components. Up to now, dynamo mechanism is the most successful theory to explain large-scale magnetic fields up to now, although the dynamos of $\alpha\Omega$-type are characterized by very small pitch angles (Section 1.2), e.g. $\sim 0.05^{\rm o}$ (for example solar dynamo). Pitch angles of $10 - 40^{\rm o}$ are reported for nearby spiral galaxies (Fig. 1.1). The magnetic pitch angles have a tendency to decrease outwards (Beck 1993). Typically, the regular magnetic fields repeat the optical spiral pattern of a galaxy. The torus of regular magnetic fields (shown as the polarized intensity, Fig. 1.2) of M 31 is correlated with the optical structure (Berkhuijsen et al. 1993). The 'arms' of the regular magnetic field in NGC 6946 are following the shape of the optical arms. Regular fields are reported to be about 10μG, whereas the turbulent magnetic fields are 15μG (Beck & Hoernes 1996). M51 (Whirlpool galaxy) is an example of a galaxy with strong density waves, bright spiral arms and 'grand design' structure. The magnetic field strength is about 10μG in inter-arm regions and 30μG along the optical arms in dust lanes (Fig. 1.3). The magnetic fields in such regions can be compressed and sheared by the gas flow in spiral arms and bars (Elstner et al. 2000, Otmianowska-Mazur et al. 2002). Here it is not the pitch angle but the strength of magnetic fields which remains a mystery. What has generated the magnetic fields of, say, about $\sim 10\mu$G between the optical spiral arms which can be compressed along the dust lanes up to the observed values? The question is still not answered. Further, there are the regular magnetic fields between the optical arms. It is not quite clear how the magnetic fields are generated there. The plot of polarized intensity would give an impression of dynamo action (because of the seemingly coherent field), but it is very probable that the magnetic fields are not coherent. Faraday rotation pictures show the reversals of

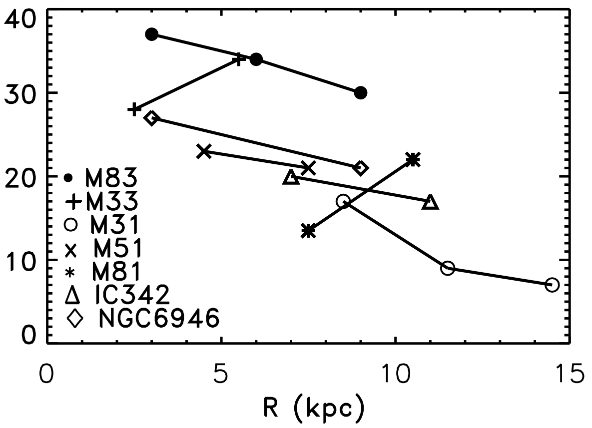

Figure 1.1: Observed radial variation of field pitch angles (Beck 1993)

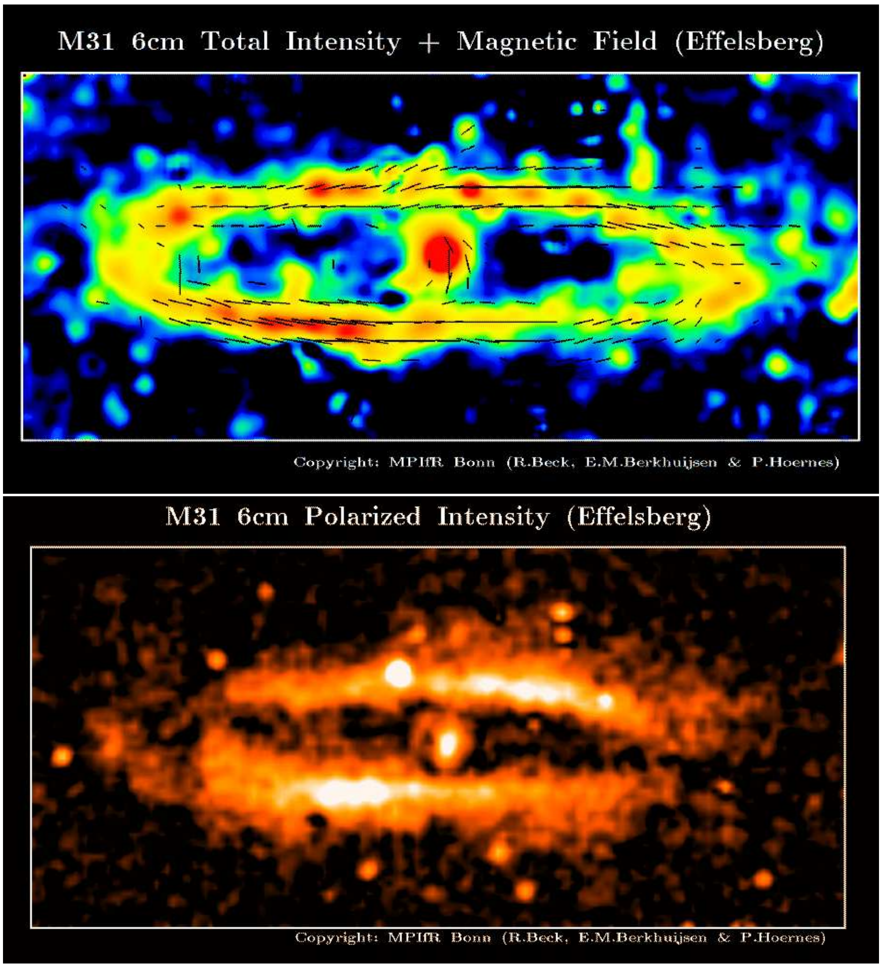

Figure 1.2: M31: Total intensity plus magnetic fields (top) and polarized intensity (bottom). Credit: MPIfR Bonn (R. Beck et al.)

the radial and azimuthal magnetic field components B_R and B_ϕ (from discussion with A. Fletcher). Reversals on kpc scales were reported for the Milky Way in the papers of Simard-Normandin & Kronberg (1979) for $R = 8.0$ kpc (confirmed by Lyne & Smith 1989), Rand & Lyne (1994) for $R = 5.5$ kpc and Han et al. (2002) for $R \sim 3$ kpc. The results of Brown et al. (2003) show no evidence for reversals in the outer Galaxy. Similarly, there are no further reports about reversals in other nearby galaxies. In spite of uncertainties in the observations, the question of origin and importance of magnetic field reversals is still an interesting one.

Another interesting example is NGC 4414, where the magnetic pitch angle cannot be due to galactic radial flows (Fig. 1.4), Soida et al. 2002. NGC 4414 is a face-on (inclination 55^o) flocculent galaxy. The gas surface densities are high and similar to those in M 51, M 100 and NGC 5055. There is evidence of dynamical processes producing spiral structures (Thornley & Mundy 1997), yet the end result

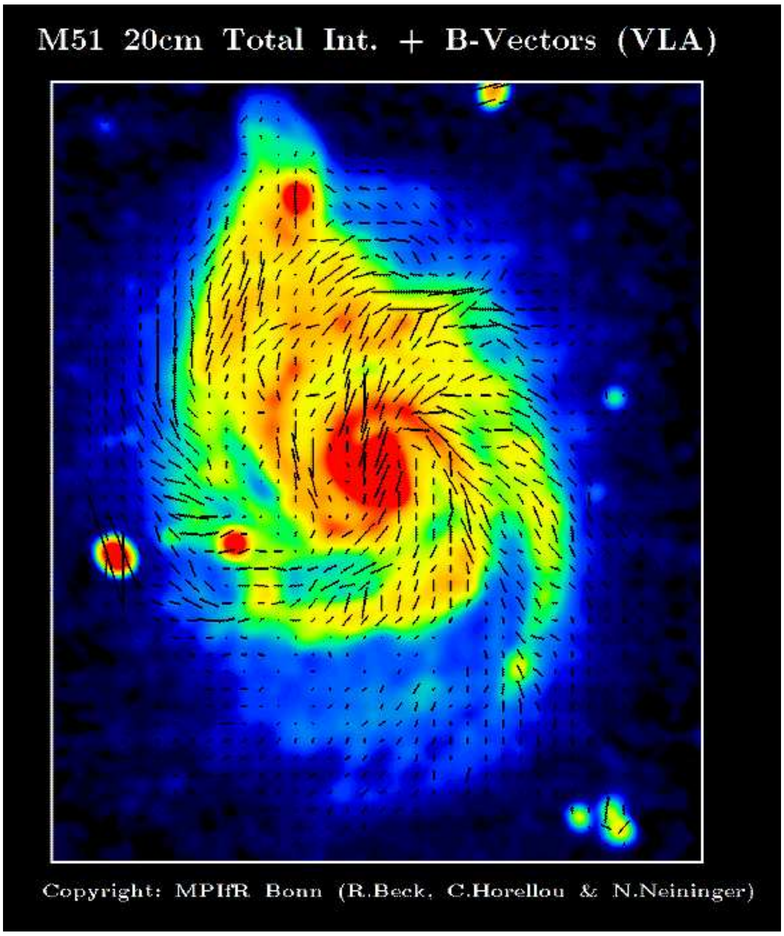

Figure 1.3: M51: Total intensity plus vectors of magnetic fields. Credit: MPIfR Bonn (R. Beck et al.)

is *not* a grand-design spiral. The poorly organized structure in NGC 4414 may be explained by its isolation (no companion, whereas M 51, M 100 and NGC 5055 all have companions). There is a suggestion of a rough, four-arm structure and a ring of tightly wound arms near the center at a radius $\simeq 2\,\mathrm{kpc}$ (dark-grey regions on the Fig. 1.4). The magnetic fields have a global structure, with the regular component $\langle \boldsymbol{B}_{\rm reg}\rangle = 4 \pm 1\mu$G and the turbulent one $(\langle \boldsymbol{B}_{\rm T}^2\rangle)^{-1/2} = 15 \pm 4\mu$G. The average ratio $\langle \boldsymbol{B}_{\rm reg}\rangle/(\langle \boldsymbol{B}_{\rm T}^2\rangle)^{-1/2}$ is 0.25. The magnetic pitch angles are quite large ($40^{\rm o} - 45^{\rm o}$), in a view of the absent radial flows (Soida et al. 2002). The interesting detail is that the largest pitch angles are in the very inner part of the disk ($R < 1.4$ kpc), which corresponds to the 'rigid rotation' part of the rotation curve (Sakamoto 1996). As far as NGC 4414 is not a star-burst galaxy and having no radial flows, we have to find an explanation for its large turbulent magnetic fields and large pitch angles.

The large pitch angles are the most characteristic property of magnetic fields

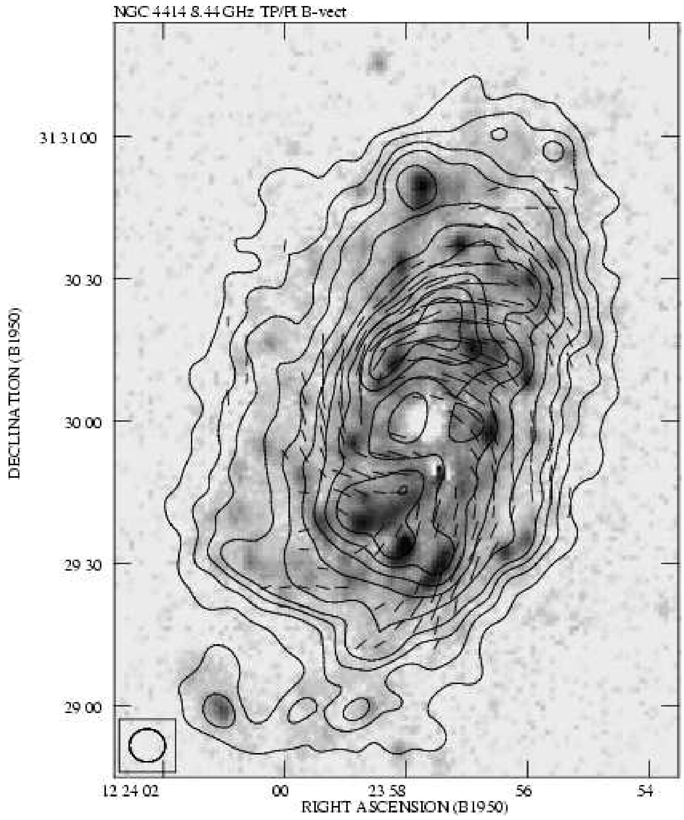

Figure 1.4: Total power map of NGC 4414 at 8.44 GHz with polarization-vectors superimposed onto the H_α image from Pogge (1989), see Soida et al. (2002)

in galaxies. Therefore, the galactic dynamo (if it is indeed the most powerful magnetic field amplification mechanism) has to be quite different from the solar/stellar $\alpha\Omega$-dynamo which gives a pitch angle of about -1° (Brandenburg, Moss, Tuominen 1992).

1.1.2 Axisymmetry

Although, as a rule, the spiral structure has a non-axisymmetric geometry, the global magnetic field is classified as axisymmetrical (ASS) if the magnetic polarity does not reverse along the azimuth. Table 1.1 and Table 1.2 show that there are only two examples which might be considered bisymmetric (BSS) (Beck 2000). M 81 is the only but uncertain (from discussions with R. Beck) example of a dominant BSS ($\sin(\phi)$ variation of magnetic field directions, two arms). Another (doubtful) example of a seemingly BSS galaxy is NGC 4631, edge-on. Dynamo theory predicts an ASS structure to appear at first (for objects with strong shear), while BSS is a mode which can be developed only for specific C_α, C_Ω values (where C_Ω has to be small compared to C_α and the α-tensor must be anisotropic).

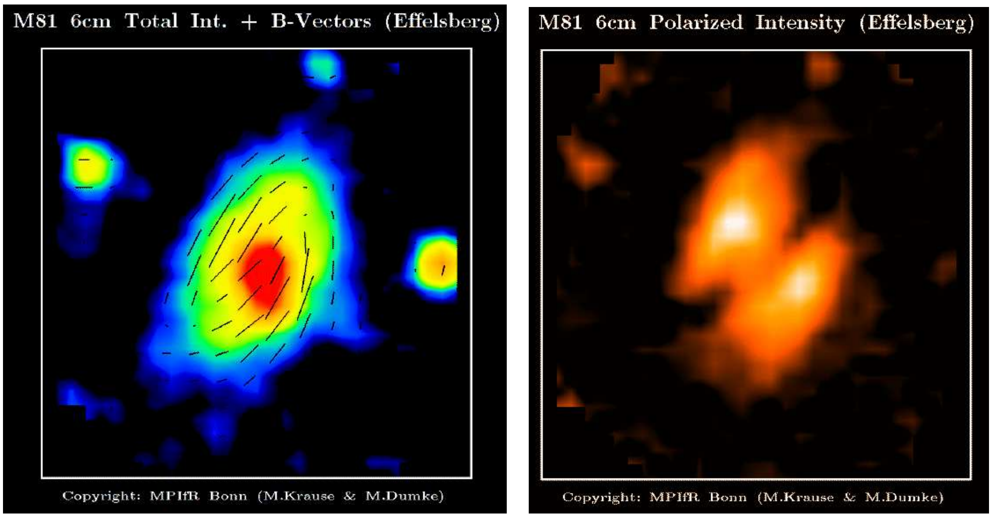

Figure 1.5: M 81. Total intensity plus magnetic fields (left) and polarized intensity (right). Credit: MPIfR Bonn (R. Beck et al.)

The dimensionless dynamo numbers C_α and C_Ω are given in Section 1.2.1 and represent the amplification of magnetic fields due to helical turbulence and to disk rotation, respectively.

As for the edge-on galaxy NGC 4631, the maps in polarized emission give the impression of a proper dipole, which is *not* a case. The map of rotation measure does not show the expected (for a dipole) changes in magnetic field directions. Therefore, instead of having a nice example of a dynamo producing the dipole, we must suggest the strong B_z to be due to a galactic wind blown away from star-forming regions. The comparison between the velocity diagram (Golla & Wielebinski 1994) and the total intensity map suggests a connection between rotation of the galaxy and its magnetic field orientation in the halo. The magnetic fields are perpendicular to the plane only above the central rigidly rotating region. Meanwhile, the number of known galaxies with a vertical magnetic field structure is growing (Tüllmann et al. 2000).

M 31 (Andromeda galaxy) is the best studied ASS example. It is showing beautifully regular magnetic fields organized in an axisymmetrical ‘ring’ structure (Fig. 1.2). The magnetic torus turns this galaxy in to the best galactic dynamo candidate (Beck 2000). The small pitch angles ($\sim 10^o$) are consistent with low SN activity observed in M 31. Nevertheless, we know nothing about its history. For a successful dynamo operation we may suggest that there were many more of supernovae to create a strong turbulence during last few Gyr. Actually, M 31 is an example of an *extraordinary* situation in a spiral galaxy, with the ratio of the transverse components of the regular to the turbulent magnetic fields of ≥ 1.4.

M51 (Whirlpool galaxy) as well as NGC 6949 are examples of strongly mixed modes (MSS) (Beck 2000). The latter is an isolated spiral galaxy, without density

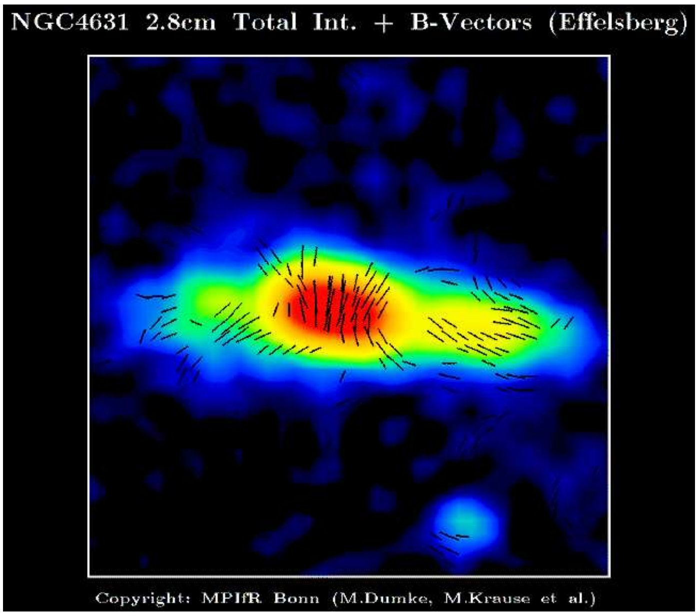

Figure 1.6: NGC 4631: Total intensity plus magnetic fields. Credit: MPIfR Bonn (R. Beck et al.)

waves. Therefore, it is another good example for applying the dynamo theory. A certain success in modeling the dynamo-excited magnetic arms in NGC 6949 has been obtained by Rohde & Elstner (1998).

However, for most galaxies it is more complicated to interpret the origin of the magnetic fields then it is for M 51, M 81, M 31, NGC 4631. There is no single opinion about preference between quadrupole or dipole symmetry with the respect to a galactic plane. Most of Faraday rotation plots (for both face-on and inclined galaxies) show that here should be at least a mix of both symmetries. But there are no observed edge-on examples with a clear dipolar or quadrupolar magnetic fields.

1.1.3 Questions waiting to answer

Many questions have been already answered by dynamo theory, for example the questions:

i) Why the magnetic fields are following the optical spiral arms?

ii) How to produce necessarily magnetic quadrupolar fields?

iii) Which structure (ASS or BSS) is resulting from theory?

However, it is doubtful, whether the following questions can be answered by dynamo theory alone.

iv) How to get the mean magnetic field amplified to about 10 μG within 1–2 Gyr?

v) How to achieve the pitch angle between -10^{o} till -40^{o} within 1–2 Gyr?

vi) How to get the vertical magnetic fields?

The vertical magnetic fields can be supported by dynamo-driven mean-field configuration, either dipolar or quadrupolar. Questions iv) and v) would be answered completely, if it was not for the time-limit (1–2 Gyr). Only very special types of dynamo are sufficiently fast to amplify the magnetic fields and produce the large pitch angles (Section 1.2.2).
The following questions are addressed to the theory which should explain how to create the turbulence:

i) How do reversals appear?

ii) Which fast mechanism is amplifying the magnetic fields in extremely young galaxies?

iii) Which is the slope of the spectrum of the turbulent magnetic fields?

iv) Is it possible to obtain large pitch angles through the instabilities?

The Parker instability driven dynamo has been investigated by Hanasz et al. (1993, 1997, 1998, 2004). The idea of the galactic dynamo driven by galactic cosmic rays (CRs) accelerated in supernova remnants has first appeared in Parker (1992). Complete 3D magnetohydrodynamic simulations by Hanasz et al. (2004) contain a network of interacting forces: the buoyancy force of CRs, the Coriolis force, the differential rotation, and the magnetic reconnection. Parker (1992) estimated that such a dynamo would be able to amplify the magnetic field on $\sim 10^8$ yr; the result of Hanasz et al. (2004) is the growth of magnetic field with the e-folding time about 250 Myr. The resulting pitch angle is small compared to observed value, the obtained radial magnetic field component is only one tenth of azimuthal one. The initial azimuthal magnetic field has been pre-assumed, what leaves the question of the galactic magnetic field origin as still open one.

1.2 The galactic dynamo

The theory of magnetohydrodynamics describes the fluid mechanics of plasma and the behavior of its magnetic fields. Derived from Maxwell's equations for the electromagnetic fields and combining with the equations of hydrodynamics, we have the following system of equations.
Conservation laws of mass,

$$\frac{D\rho}{Dt} + \rho\nabla \cdot \boldsymbol{u} = 0, \tag{1.3}$$

of momentum,

$$\rho\frac{D\boldsymbol{u}}{Dt} = -\nabla P - \rho\nabla\Psi + F, \tag{1.4}$$

together with the induction equation

$$\frac{\partial \boldsymbol{B}}{\partial t} = \nabla \times \left(\boldsymbol{u} \times \boldsymbol{B} - \frac{1}{4\pi\sigma}\nabla \times \boldsymbol{B}\right). \tag{1.5}$$

Ψ is the gravitational potential, and F is the Lorentz force which normally can be split into two terms: magnetic pressure and magnetic tension. The Lagrangian derivative D/Dt, ∇ and $\nabla \times \boldsymbol{B}$ operators are given in Appendix 1. The gas pressure, P, can be a very complicate expression, due to the different atomic and molecular phases. The simplest case is the isothermal one, $P = c_\mathrm{s}^2\rho$ (where c_s is a sound speed), for one gaseous phase. For cases with more physics included, the equation for inner energy e should be solved

$$\frac{D}{Dt}\frac{e}{\rho} = -P\nabla\cdot\boldsymbol{u} - \mathcal{F}, \tag{1.6}$$

where $\mathcal{F}$ describes the radiative losses. The diffusion term in the induction equation can be ignored if the diffusion time-scale is much longer than the flow time-scale. In this case a useful picture emerges in which the magnetic field lines are frozen into the plasma. Matter is therefore threaded on the field lines which are advected and distorted by the flow. In the other extreme, the velocity term is small and the induction equation becomes purely diffusive, so matter can move freely across the field lines.

Kinematic theory is appropriate when the magnetic force only has a small effect on the motions. The velocity solution of non-magnetic momentum equation can be then used for the induction equation to calculate $\boldsymbol{B}$.

In Section 1.2.1 a short introduction into the mean-field dynamo mechanism of magnetic field amplification is given, with an overview of the successes of dynamo theory and the remaining open questions.

1.2.1 Mean-field dynamo theory

Introduction. Dynamo theory describes how magnetic fields can be amplified and sustained by fluid motions, in the presence of dissipation. Certain conditions are necessary for dynamo actions, and various types of dynamos can be defined.

Let us consider the total magnetic and velocity fields as the sum of mean fields and fluctuations

$$\boldsymbol{B} = \langle\boldsymbol{B}\rangle + \boldsymbol{B'}, \qquad \boldsymbol{u} = \langle\boldsymbol{u}\rangle + \boldsymbol{u'}. \tag{1.7}$$

After substitution of the expressions for magnetic and velocity fields and after averaging, the linearized mean-field induction equation is

$$\frac{\partial\langle\boldsymbol{B}\rangle}{\partial t} = \mathrm{curl}\left(\langle\boldsymbol{u}\rangle \times \langle\boldsymbol{B}\rangle + \langle\boldsymbol{u'} \times \boldsymbol{B'}\rangle - \frac{1}{4\pi\sigma}\mathrm{curl}\langle\boldsymbol{B}\rangle\right). \tag{1.8}$$

The turbulent electromotive force, $\boldsymbol{\mathcal{E}} = \langle \boldsymbol{u'} \times \boldsymbol{B'} \rangle$, can be changed in space only when $\langle \boldsymbol{B} \rangle$ or its first derivative has been changed (see the last equation). Therefore, the turbulent electromotive force $\boldsymbol{\mathcal{E}} = \langle \boldsymbol{u'} \times \boldsymbol{B'} \rangle$ is split into its non-diffusive and diffusive components, where only terms of the first order in $\langle \boldsymbol{B} \rangle$ are left:

$$\boldsymbol{\mathcal{E}} = \alpha \langle \boldsymbol{B} \rangle - \eta_{\mathrm{T}} \mathrm{curl} \langle \boldsymbol{B} \rangle. \tag{1.9}$$

Tensors α and η_{T} are determined by the turbulent field $\boldsymbol{u'}$.
For non-mirror symmetrical turbulence we have a turbulent electromotive force $\alpha\langle \boldsymbol{B} \rangle$, which is parallel $(\alpha > 0)$ or antiparallel $(\alpha < 0)$ to the mean magnetic field. This effect is called α-effect.

$$\frac{\partial \langle \boldsymbol{B} \rangle}{\partial t} = \mathrm{curl} \left(\langle \boldsymbol{u} \rangle \times \langle \boldsymbol{B} \rangle + \alpha \langle \boldsymbol{B} \rangle - \mathrm{curl} \langle \boldsymbol{B} \rangle \left(\frac{1}{4\pi\sigma} + \eta_{\mathrm{T}} \right) \right). \tag{1.10}$$

The α and η_{T} tensors. Analytical expressions. To derive α and η_{T} tensors, one needs to consider the induction equation for the fluctuating part of the magnetic field (Krause & Rädler 1980). The relation $\langle \boldsymbol{u} \rangle = 0$ was assumed for simplicity.

$$\frac{\partial \boldsymbol{B'}}{\partial t} - \frac{1}{4\pi\sigma} \Delta \boldsymbol{B'} - \mathrm{curl}(\boldsymbol{u'} \times \boldsymbol{B'} - \langle \boldsymbol{u'} \times \boldsymbol{B'} \rangle) = \mathrm{curl}(\boldsymbol{u'} \times \langle \boldsymbol{B} \rangle). \tag{1.11}$$

Neglecting all second order terms, one is left with

$$\boldsymbol{B'}(\boldsymbol{r}, t) = \boldsymbol{B'}(\boldsymbol{r}, t_0) + \int_{t_0}^{t} \left[\mathrm{curl}(\boldsymbol{u'} \times \langle \boldsymbol{B} \rangle) + \frac{1}{4\pi\sigma} \Delta \boldsymbol{B'} \right] dt, \tag{1.12}$$

where $\boldsymbol{r}$ is the space vector. Then the electromotive force can be calculated as the $\boldsymbol{B'}(\boldsymbol{r}, t)$ from last formula multiplied with $\boldsymbol{u'}(\boldsymbol{r}, t)$ and averaging afterwards.

$$\boldsymbol{\mathcal{E}}(\boldsymbol{r}, t) = \int_{t_0}^{t} \langle \boldsymbol{u'}(\boldsymbol{r}, t) \times \left[\mathrm{curl}(\boldsymbol{u'} \times \langle \boldsymbol{B} \rangle) + \frac{1}{4\pi\sigma} \Delta \boldsymbol{B'} \right] \rangle dt. \tag{1.13}$$

Solution for the high-conductivity case:

$$\alpha = -\frac{1}{3} \int_{0}^{\infty} \langle \boldsymbol{u'}(\boldsymbol{r}, t) \cdot \mathrm{curl}\, \boldsymbol{u'}(\boldsymbol{r}, t - \tau) \rangle dt, \tag{1.14}$$

$$\eta_{\mathrm{T}} = \frac{1}{3} \int_{0}^{\infty} \langle \boldsymbol{u'}(\boldsymbol{r}, t) \cdot \boldsymbol{u'}(\boldsymbol{r}, t - \tau) \rangle dt. \tag{1.15}$$

The helicity $\mathcal{H}$ (pseudo-scalar) is

$$\mathcal{H} = \langle \boldsymbol{u'} \cdot \mathrm{curl}\, \boldsymbol{u'} \rangle. \tag{1.16}$$

The helicity is an important characteristic of the turbulence $\boldsymbol{u'}$: $h = 0$ for mirror-symmetric turbulence. If $\mathcal{H} = 0$ or mirror symmetry holds for any time moment, then the $\alpha-$term is equal to zero (Eq. (1.14)).

The simplification with neglecting of the terms of second and higher order of fluctuations is valid only if $\partial \boldsymbol{B'}/\partial t$ or $\Delta \boldsymbol{B'}/4\pi\sigma$ are large as compared with $\mathrm{curl}(\boldsymbol{u'} \times \boldsymbol{B'} - \langle \boldsymbol{u'} \times \boldsymbol{B'} \rangle)$. It happens, if

$$\min(\mathrm{Rm}, \mathrm{S}) \ll 1, \tag{1.17}$$

where the magnetic Reynolds number and Strouhal number are

$$\mathrm{Rm} = \mu\sigma\sqrt{\langle \boldsymbol{u'}^2 \rangle}\lambda_{\mathrm{corr}}, \tag{1.18}$$

$$\mathrm{S} = \sqrt{\langle \boldsymbol{u'}^2 \rangle}\frac{\tau_{\mathrm{corr}}}{\lambda_{\mathrm{corr}}}, \tag{1.19}$$

where λ_{corr} and τ_{corr} are characteristic length and time. The numbers are connected as

$$\mathrm{Rm} = \frac{\mu\sigma\lambda_{\mathrm{corr}}^2}{\tau_{\mathrm{corr}}}\mathrm{S}. \tag{1.20}$$

The second possible simplification is possible by choosing a conductivity limit. In the **high conductivity limit** we have the $S \ll 1$ condition, and for the **low-conductivity limit** $\mathrm{Rm} \ll 1$.

The structure of the alpha-tensor. The integration needed for the representation of the electromotive force $\boldsymbol{\mathcal{E}}(\boldsymbol{r}, t)$ is a hard task. It was done by Kitchatinov & Rüdiger (1992) with the help of Fourier analysis for the case of small Strouhal numbers.

The resulting α tensor splits into two parts which separately involve the effects of the inhomogeneities of turbulence intensity and density:

$$\alpha = \alpha^u + \alpha^\rho. \tag{1.21}$$

Both tensors have the same structure

$$\alpha_{im}^\rho = -\delta_{im}(\boldsymbol{\Omega}\cdot\boldsymbol{G})\alpha_1^\rho - (\Omega_m G_i + \Omega_i G_m)\alpha_2^\rho - (\Omega_m G_i - \Omega_i G_m)\alpha_3^\rho - \frac{\Omega_i\Omega_m}{\Omega^2}(\boldsymbol{\Omega}\cdot\boldsymbol{G})\alpha_4^\rho, \tag{1.22}$$

$$\alpha_{im}^u = -\delta_{im}(\boldsymbol{\Omega}\cdot\boldsymbol{U})\alpha_1^u - (\Omega_m U_i + \Omega_i U_m)\alpha_2^u - (\Omega_m U_i - \Omega_i U_m)\alpha_3^u - \frac{\Omega_i\Omega_m}{\Omega^2}(\boldsymbol{\Omega}\cdot\boldsymbol{U})\alpha_4^u, \tag{1.23}$$

$$\alpha_3^u = \alpha_3^\rho, \tag{1.24}$$

where $\boldsymbol{U} = \nabla \log\left(\sqrt{\langle \boldsymbol{u}'^2 \rangle}\right)$, $\boldsymbol{G} = \nabla \log \rho$. The α_n^ρ and α_n^u (for $n = 1, 2, 3, 4$) are integrals of turbulent intensities and Coriolis numbers $\Omega^* = 2\tau\Omega$ over ω, k. The equality $\alpha_3^u = \alpha_3^\rho$ means that both inhomogeneities can be combined in a common gradient, $\nabla \log(\rho u_{\mathrm{T}})$, in the antisymmetric part of the α-tensor. The turbulent velocity u_{T} is defined as $u_{\mathrm{T}} = \sqrt{\langle \boldsymbol{u}'^2 \rangle}$. For the axisymmetric geometry of a star this antisymmetric part corresponds to a transport of the mean magnetic field in the azimuthal direction similar to the inducing action of differential rotation.

Differential rotation, however, is more powerful than the antisymmetric part of the α-tensor, so the latter is most probably of minor importance.

Relative contributions of the two basic inhomogeneities depend on the angular velocity. For this reason the **weight factor** S was introduced in Kitchatinov & Rüdiger (1992), it characterizes the relative contribution of the density inhomogeneity in the α-coefficient

$$\alpha = -\alpha_1^u \Omega \nabla \log(\rho^S u_\mathrm{T}). \tag{1.25}$$

The alpha-tensor exists only in inhomogeneous fluids. It forms a pseudo-tensor. The symmetric part (the 'alpha-effect') can only exist in rotating turbulence fields. That is not the case for the antisymmetric part of the tensor, which occurs already in non-rotating turbulence. It was generally shown in Krause & Rädler (1980), that it 'almost always' vanishes for homogeneous fields (except higher order correlations are involved). The general expressions are too bulky, so it is therefore more convenient to continue the discussion for individual astrophysical applications.

Application for α-effect in shear flows. An accretion disk can only exist if there is an instability which transports the angular momentum outwards, or, in other words, the turbulent viscosity is positive. Brandenburg & Schmitt (1998) propose an interesting argument for magnetic shear flows that for positive viscosity the dynamo-α must be negative in the upper disk plane. The sign is important because in α-dynamos the sign of the α-effect directs the resulting geometry. The most easily excited mode has quadrupolar geometry for positive α-effect and has dipolar geometry for negative α-effect (Torkelsson & Brandenburg 1994a,b). Rüdiger et al. (1995), working with positive α-effect, found only solutions with the quadrupolar symmetry dominating. The more desired magnetic geometry is a dipolar one (negative α-effect), because it is odd with respect to the equator, the poloidal field lines are supporting jets and outflows. Maxima of the toroidal fields are located in the halo (Rekowski et al. 2000). A quasi-linear second-order correlation-approximation provides the surprising result that the *minus* between kinetic helicity and α-effect (see Eq. (1.14)) disappears but nevertheless the α-effect proves to be positive again (Rüdiger et al. 2000). As the only possibility to find *negative* α-effects, we must consider differential rotation, i.e. the inclusion of a shear. Indeed, for a sufficiently high shear rate the dynamo- changes its sign and even takes the desired negative values for the case of Kepler rotation (Rüdiger & Pipin 2000),

$$\alpha_{\phi\phi} = -(\boldsymbol{G}\cdot\boldsymbol{\Omega})\left(\alpha_1 + \alpha_2 \frac{\partial \ln \Omega}{\partial \ln R}\right). \tag{1.26}$$

For a Kepler disk with its vertical gravity, $g_z = -\Omega^2 z$, the Eq. (1.26) transforms to

$$\alpha_{\phi\phi} = -\frac{z\Omega^3}{5}\frac{\tau_\mathrm{corr}^2}{c_\mathrm{s}^2}\frac{\langle B^{(0)2}\rangle}{\mu\rho}, \tag{1.27}$$

where c_s is a sound speed, $\boldsymbol{B}^{(0)}$ is the original prescribed magnetic field (fluctuating). For rigid rotation the α-effect proves to be positive in the upper disk plane and negative in the lower disk plane. The opposite is true for Kepler flows. The dynamo-α becomes negative in the upper disk plane and positive in the lower disk plane. Again the results comply with the results of the numerical simulations by (Brandenburg et al. 1996). Both density stratification and differential rotation are important for the α-dynamo in astrophysical sheared disks. As one can see from Eq. (1.26), the dynamo can work without the differential rotation.

Application for galactic dynamos. If the Ω-containing terms can be neglected in α-tensor (α^2-dynamo), then the resulting global magnetic field is stable one and never oscillating, whereas the solutions of $\alpha\Omega$-dynamo are oscillating. An illuminating example of kinematic dynamo theory for the cycle periods is a **dynamo wave** solution. Within the local approach, the (galactic) disk of thickness H can be imitated with the Cartesian box. In plane Cartesian geometry we consider a mean magnetic field to be subjected to a strong shear flow with α-dynamo effect taken into account. All quantities vary only in the z-direction with the given wave number (1D dynamo). The amplitude equations can then be written as

$$\dot{A} + A = C_\alpha B, \quad \dot{B} + B = \mathrm{i} C_\Omega A, \tag{1.28}$$

with A representing the poloidal magnetic field component and B the toroidal component. The $C_\Omega \gg C_\alpha$ assumption has been used. C_α and C_Ω are called the *dynamo coefficients*. C_α is the normalized α, and C_Ω is the normalized rotation,

$$C_\alpha = \frac{\alpha H}{\eta_T}, \quad C_\Omega = \frac{\Omega H^2}{\eta_T}. \tag{1.29}$$

Magnetic energy is scaled with a critical dynamo number D,

$$D = C_\alpha C_\Omega. \tag{1.30}$$

Assuming $A \sim \exp(-\mathrm{i}\omega t)$, $B \sim \exp(-\mathrm{i}\omega t)$, the Eq. (1.28) leads to the simple quadratic equation. The eigenfrequency is the complex number

$$\omega_\mathrm{cyc} = \sqrt{\frac{D}{2}} + i \left(1 - \sqrt{\frac{D}{2}}\right). \tag{1.31}$$

A marginal solution of the magnetic field is thus found for a dynamo number $D = 2$. In this case the field is not steady but oscillates with the frequency (dimensionless) $\omega_\mathrm{cyc} = 1$ (Rüdiger & Hollerbach 2004). Detailed investigation of 1D dynamo one can find in Parker (1971).

The system of equations (1.28) can be solved in a different way by excluding the frequency. It is easy to show that the following relation results for the pitch angle,

$$\tan p = \frac{A}{B} = \left(\frac{C_\alpha}{C_\Omega}\right)^{1/2}. \tag{1.32}$$

Assuming usual galactic parameters $\alpha = 10\,\mathrm{km/s}$, $H = 1\,\mathrm{kpc}$ and $\Omega = 100\,\mathrm{Gyr}^{-1}$, one can estimate the pitch angle to be about 18°. The estimation is valid until saturation of the dynamo. Growing magnetic fields are affecting the turbulence and, as a result, one has to take into account the feedback of magnetic field expressed in quenching of α-tensor and magnetic diffusivity η_{T}. Detailed description for the quenching functions will be given in the following paragraphs. In terms of the pitch angles, the quenching of the alpha-tensor leads to the decrease of p to zero for the vanishing magnetic diffusivity,

$$\tan p = \frac{\sqrt{D_{\mathrm{crit}}}}{C_{\Omega}} \sim \eta_{\mathrm{T}}. \tag{1.33}$$

The parameters, such as turbulence and η_{T}, are badly known for galaxies. The most popular source for turbulence in ISM is stellar ‘activity’. The analytical work was done by Ferrière (1992, 1993a, 1993b, 1996, 1998) to derive the analytical expressions for alpha and η_{T} coefficients with supernova explosions (SN) and superbubbles (SBs) as the main drivers of turbulence. The magnetic diffusivity is found to be quite small, which results in a vanishing pitch angle.

The tensorial form of α is usually quite complicate. Strong anisotropic α-tensor (vanishing α_{zz} component for fast rotating disks) appeared first in analytical papers by Moffatt (1970) and Rüdiger (1978), then in the analytical estimation of α due to SN/SB in galactic disks (Ferrière 1992). It was found that SBs are much more efficient than the isolated supernovae at removing magnetic flux from the Galactic disk. And, finally, α_{zz} is found to vanish in the case of SBs when for simplicity they are taken to be cylindrical. The result is that **‘northern’ $\alpha_{\phi\phi}$ is positive**. Remarkable work was also done by Kaisig et al. (1993), the α_{zz} component was calculated for the known SN explosion rate. The influence of the density distribution proved to be surprisingly small. The component α_{zz} **is always negative at the north and positive at the south of the disk**.

The full anisotropic α-tensor for a differentially rotating disk with density stratification (modeling of galactic disk) has the following form (Elstner et al. 1996):

$$\alpha_{ij} = -\left(\alpha^{\rho}_{ij}\frac{\partial \log \rho}{\partial z} + \alpha^{u}_{ij}\frac{\partial \log u'}{\partial z}\right)\langle u'^2\rangle \tau_{\mathrm{corr}}, \tag{1.34}$$

with

$$\alpha^{\rho} = \begin{pmatrix} \frac{2}{5}\Omega^{*}\tilde{\psi} & -U^{\mathrm{buo}} & 0 \\ U^{\mathrm{buo}} & \frac{2}{5}\Omega^{*}\tilde{\psi} & 0 \\ 0 & 0 & -\frac{2}{15}\Omega^{*}\tilde{\psi}_z \end{pmatrix}, \tag{1.35}$$

$$\alpha^{u} = \begin{pmatrix} \frac{4}{15}\Omega^{*}\tilde{\psi} & -U^{\mathrm{dia}} & 0 \\ U^{\mathrm{dia}} & \frac{4}{15}\Omega^{*}\tilde{\psi} & 0 \\ 0 & 0 & -\frac{8}{15}\Omega^{*}\tilde{\psi}_z \end{pmatrix}, \tag{1.36}$$

$$\tilde{\psi} = \psi + \frac{15}{8}\frac{\bar{B}_z^2}{B^2}\psi_1, \qquad \tilde{\psi}_z = \psi_z - \frac{15}{16}\frac{\bar{B}_z^2}{B^2}\psi_1. \tag{1.37}$$

The α-quenching functions ψ are given in Rüdiger & Kitchatinov (1993). $U^{\rm buo}$ is a magnetic-advection velocity often called the magnetic buoyancy,

$$U^{\rm buo} = \frac{1}{8\beta^2}\left(\frac{3+5\beta^2}{(1+\beta^2)^2} + \frac{3}{\beta}\tan^{-1}\beta\right), \tag{1.38}$$

where

$$\beta = \langle B\rangle / B_{\rm eq}, \tag{1.39}$$

$B_{\rm eq}$ is the equipartition field. The diamagnetic effect takes place when the magnetic field is transported with an effective velocity

$$U^{\rm dia} = \frac{1}{2\beta^2}\left(-\frac{1}{1+\beta^2} + \frac{1}{\beta}\tan^{-1}\beta\right). \tag{1.40}$$

The mean-field induction equation has been solved with a 2D time-stepping code for a turbulent flow and a given galactic rotation (Elstner at al. 1995). The free parameters in the model are the quantities representing the vertical structure and 'mixing-time' $\tau_{\rm corr}$. The latter strongly influences the characteristics of the resulting magnetic field. Short correlation times provide a steady quadrupole while longer correlation times provide an oscillating dipole. If the magnetic feedback also concerns the eddy diffusivity tensor, only the oscillating solutions remain realistic with the periods of 1 Gyr.

Quenching functions. The quenching process is connected with the preservation of the total magnetic helicity in media with the high magnetic Reynolds numbers (Berger & Field 1984, Brandenburg et al. 2002). The α-tensor includes a consistent feedback mechanism of the magnetic field, but usually one neglects the feedback onto the eddy diffusivity (Elstner et al. 1995). Some authors insisted (Kitchatinov & Rüdiger 1992) that "... it makes no sense to apply several quenching descriptions of the α-effect if it is not clear that the corresponding turbulence model leads to a reasonable $\eta_{\rm T}$ quenching".

The solution for EMF must be found which is excluding the infinite growth of $B \to \infty$. Therefore, in strong-field limit only those terms of EMF should be retained which do not depend on the magnetic field amplitude at all. The quenching functions, mentioned in galactic dynamo applications, have the following form (Rüdiger et al. 1993). The function ψ is of major importance because it describes the magnetic quenching of the $\alpha_{\phi\phi}$-coefficient which is essential for the $\alpha\Omega$-dynamo,

$$\alpha_{\phi\phi} = \alpha_0 \psi(\beta). \tag{1.41}$$

α_0 here stands for the 'non-magnetic' value, i.e. $\beta = 0$. The quenching functions for Eq. (1.37) are

$$\psi(\beta) = \frac{15}{32\beta^4}\left(1 - \frac{4\beta^2}{3(1+\beta^2)^2} - \frac{1-\beta^2}{\beta}\tan^{-1}\beta\right), \tag{1.42}$$

$$\psi_1(\beta) = \frac{1}{4\beta^4}\left(\beta^2 - 5 + \frac{2\beta^2}{3(1+\beta^2)} + \frac{4\beta^4(3\beta^2-1)}{3(1+\beta^2)} + \frac{5+\beta^4}{\beta}\tan^{-1}\beta\right). \tag{1.43}$$

The expression for ψ_z is extremely bulky and given in Rüdiger & Kitchatinov (1993). In the weak-field case we have

$$\psi(\beta) = 1 - \frac{12}{7}\beta^2, \quad \psi_1(\beta) = \frac{40}{21}\beta^2, \quad \psi_z \to 1. \tag{1.44}$$

In the opposite limit of strong fields, $\beta \gg 1$,

$$\psi(\beta) = \frac{15\pi}{64\beta^3}, \quad \psi_1(\beta) = \frac{\pi}{8\beta}, \quad \psi_z(\beta) = -\frac{1}{2}\Psi(\beta) + \frac{3\pi}{25\beta}. \tag{1.45}$$

Therefore, one can see that the quenching is strongly anisotropic.

1.2.2 Success and limitations of the galactic dynamo theory

In galaxies there are four most important ingredients which must be present for the dynamo to work: vertical density and turbulence stratification, differential rotation, eddy diffusivity and an initial magnetic field (seed field). Dynamo theory would be the most successful if it was not for uncomfortable values of these ingredients.

Nonlinear winding of the seed field due to differential rotation was the simplest idea for explaining the magnetic pitch angle. Let us consider a galactic gaseous disk with spiral arms and presence of the vertical magnetic field. α-tensor was set to zero, but buoyancy forces and eddy diffusivity were allowed to work. The simulations of Rohde & Elstner (1998) showed that indeed the winding up would take place. The only problem is that a magnetic pitch angle comparable to the 'optical' pitch angle will survive for a very short time only. The seed field would decay. The life-time is 210 Myr according to Rohde et al. (1999). 200 Myr is the result of Otmianowska-Mazur & Chiba (1995) which is similar to Parker's estimate (1979). In the early epoch the magnetic fields are placed between the optical arms, which fits to the observations. Rather quickly, however, the magnetic arms are wound up until the pitch angle is zero. The pitch angles reach zero faster than the magnetic fields decay. The conclusion here is that the winding up of the seed field cannot give the observable magnetic fields and the correct pitch angles within 1–2 Gyr.

Seed field problem. The typical growth rate of a dynamo is $\leq 1\ \mathrm{Gyr}^{-1}$. As an example, after 2.5 Gyr the field will be amplified from 10^{-8}G to 10^{-6}G only. Therefore, the initial fields for a dynamo should be larger than 10^{-8}G. There is no contradiction with observations, though one must explain which mechanism was sufficiently fast to amplify the magnetic fields up to 10^{-8}G. In the early universe a seed field of 10^{-18}G was suggested by Hanasz & Lesch (1997). In order to form a quadrupolar geometry of the dynamo-induced fields the seed field must already have a small quadrupolar component.

The battery effect, caused by the early collapse of the material to the galactic midplane, forms electrical currents with equatorial symmetry, so the corresponding magnetic fields have no chance to be quadrupolar (Krause & Beck 1998). Ruzmaikin, Shukurov & Sokoloff (1988) discuss the possibility of magnetic field amplification by the collapsing proto-galactic cloud. The field might be compressed from 10^{-10}G to 10^{-7}G, but cannot serve as quadrupole.

The theory of small-scale dynamo (Poezd et al. 1993; Beck et al. 1994) can work for really small fields. Such dynamo, which also needs a seed field, will provide a value 10^{-8}G in only 10 Myr. The dipolar part will decay and quadrupolar part, if it exists, will be amplified.

Parker instability driven dynamo studies give very interesting results too. As it was mentioned in Sec. 1.1.3, the idea of the galactic dynamo driven by galactic cosmic rays (CRs) belongs to Parker (1992). Parker (1992) estimated that such a dynamo would be able to amplify the magnetic field on $\sim 10^8$ yr; the result of Hanasz et al. (2004) is the growth of magnetic field with the e-folding time about 250 Myr. Calculations of dynamo coefficients in Parker unstable disks have been done by Hanasz & Lesch (1993, 1997, 1998, 2000). The sign of α-effect is negative in the disk and the dynamo number D is therefore positive. The sign of α-effect is changing to the opposite from disk to halo. In Otmianowska-Mazur (2003) the time-dependent tensors of α and magnetic diffusivity η have been calculated from the same MHD model as in Hanasz (2000).

The most difficult problem of the working dynamo is the back-reaction of the growing magnetic field on the turbulent gas motion. Such feedback is called quenching and has been described in Sect. 1.2.1. Quenching can destroy completely the action of the turbulent dynamo. Externally forced numerical simulations taking into account back-reaction of the magnetic field to the turbulent motions (Cattaneo & Vainshtein 1991, Vainshtein & Cattaneo 1992, Brandenburg & Dobler 2001) showed that the Lorentz force strongly suppressed the turbulent dynamo action. This adds the reason to look for the new amplification mechanisms in the astrophysical disks.

Quadrupolar seed fields should be generated by some physical mechanism. A magneto-rotational instability is a very good candidate (see Chapter 3). Magneto-rotational instability (MRI) is a powerful and fast mechanism to generate strong magnetic fields of a few μG). MRI is free to appear under most galactic physical conditions with the only requirement: the angular frequency of galactic rotation decreasing outwards. The condition is fulfilled for *any* spiral galaxy. The energy source for MRI is the differential rotation. A very weak external vertical magnetic flux is enough for the seed field. A *quadrupolar* magnetic field geometry can be developed by MRI from the vertical initial or external field due to differential rotation, as it will be shown in Chapter 5. External magnetic fields for a galaxy are not necessary small. The strength of magnetic fields in clusters of galaxies is reported to be up to a few μG as in the Coma cluster (Thierbach, Klein & Wielebinski 2003).

The questions which are left open by dynamo theory are the following.

i) How to obtain the field amplification sufficiently fast in 1–2 Gyr?

ii) How to generate the quadrupolar part of observed galactic magnetic fields?

1.3 Magnetic turbulence

Interstellar magnetic fields are revealed by cosmic-ray electrons, spiraling around the field lines and emitting synchrotron radiation, the dominant contribution to radio continuum emission at centimeter and decimeter wavelengths. The relative contribution of thermal emission is generally small, on average 10–20% at centimeter wavelengths, and becomes negligible at decimeter wavelengths. Synchrotron emission gives the information about the magnetic turbulent and mean fields. The observation of magnetic fields via synchrotron emission is limited by the cosmic-ray electrons diffusion length which is about $\simeq 1\,\mathrm{kpc}$ from their birthplaces in star-forming regions. Thus strong, but invisible magnetic fields may still exist far away from radio-bright regions.

In the case of a completely regular magnetic field, most of the synchrotron emission is highly linearly polarized (74%). Turbulent magnetic fields are the cause for geometrical depolarization, independently from wavelength. So the radio maps are showing total magnetic fields, both regular and turbulent components, and maps of polarized intensity show *resolved* regular magnetic fields.

If an ionized gas of density n_e is mixed with the magnetic field having a net component B_{parallel} to the line of sight (e.g. regular field), the polarization plane is Faraday rotated by the angle

$$\Delta\phi[\mathrm{rad}] = \lambda^2[\mathrm{m}^2]\mathrm{RM}[\mathrm{rad\ m}^{-2}], \tag{1.46}$$

where RM is the rotation measure and λ is the wavelength used for magnetic field detection. Its sign indicates the direction of B_{parallel} along the line of sight.

A useful tool for analyzing observed fields is the *structure function* (Beck et al. 1999)

$$D_I(\delta\Theta) = \langle [I(\Theta) - I(\Theta + \delta\Theta)]^2 \rangle, \tag{1.47}$$

where Θ and $\delta\Theta$ are position angle and angular separation between two points in a map, while I is the observed distribution of any quantity (total intensity, polarized intensity, rotation measure, emission measure, thermal emission, ...). The predicted slope of the magnetic energy spectrum in a $\log D_I - \log\delta\Theta$ plot is $s = 5/3$ for projected 3-D Kolmogorov turbulence, $s = 2/3$ for 2-D turbulence (thin sheets) and $s = 0$ for a smooth distribution or in case of white noise. The impact of strong magnetic fields on the plasma can render its two-dimensional turbulence.

Table 1.3 provides us with interesting information about magnetic field structures for the example of NGC 6946.

Table 1.3: Structure function slopes for NGC 6946 (Beck et al. 1999) for the total intensity (TP), polarized intensity (PI), rotation measure (RM), Stokes Q, Stokes U, thermal emission (TH)

	Map	Slope	Angular scale (‘)	Dimension of structures
TP	6 cm	1.14±0.05	0.5-5.0	2-D + 3-D?
PI	6 cm	0.66±0.02	0.5-5.0	2-D
Q	6 cm	0.60±0.03	0.5-3.5	2-D
U	6 cm	0.67±0.02	0.5-3.5	2-D
RM	(3cm/6cm)	(0.73)	0.5-1.5	2-D
		1.24±0.10	2.5-5.0	(2+3)-D
		3.0±0.9	5.0-7.0	true 3-D?
TH	3 cm	0.62±0.07	0.5-2.0	2-D
		3.9±0.2	2.0-4.0	true 3-D?

The maps of polarized intensity, Stokes Q, Stokes U and thermal emission show 2-D turbulence ($s \simeq 2/3$) on scales of 0’.5 to 5’.0, the typical size of arm fragments. In the total intensity map, 2-D and 3-D turbulence seems to be mixed ($2/3 < s < 5/3$). The distribution of position angle shows less structure ($s < 2/3$). The structure functions of rotation measure and thermal emission steepen considerably towards largest scales to values $s > 5/3$, suggesting pure 3-D turbulence on these scales. At least from the slope of the PI structure function we can conclude that the regular fields are organized in thin sheets. An explanation of this fact is still needed.

The turbulent velocity field was widely studied by Green (1993) with PPV (position-position-velocity) data cubes analysis. The wavenumbers span from $\sim 1/3\ \mathrm{pc}^{-1}$ for the closest slices to $1/200\ \mathrm{pc}^{-1}$ for distant ones. The result is the following: The turbulence energy spectrum is close to the Kolmogorov slope with $s = [1.5 - 2.0]$.

1.4 Interstellar turbulence

The dynamo amplification of magnetic fields depends on interstellar turbulence. For solving the equation system (1.3)–(1.5) it is necessary to keep in mind that the interstellar medium contains a number of phases of very diverse characteristics. The major phases of the interstellar medium are summarized in the Table 1.4.

ISM phases and turbulent flows. The values in Table 1.4 are highly approximate. We made a merge between similar tables from Spangler (1999) and from

Table 1.4: Summarized parameters for different phases of the interstellar medium: Cold Neutral Medium (CNM), Warm Neutral Medium (WNM), Diffuse Ionized Gas (DIG), Hot Ionized Medium (HIM), coronal gas, molecular clouds and H II envelopes

Phase	Density $[\mathrm{cm}^{-3}]$	Temperature $[\mathrm{K}]$	sound speed $[\mathrm{km\ s}^{-1}]$	ionized fraction	filling factor
Molecular clouds	$\geq 10^4$	≤ 70			0.1
CNM	$20-250$	$10-75$	$0.4-0.8$	2×10^{-4}	0.01
HII envelopes	$5-10$	8000			
WNM	$0.1-0.5$	$5000-8000$	$9-11$	$\sim 10^{-2}$	0.5
DIG	0.06	8000	11	1	0.1
HIM	0.003	$6\times10^5-10^7$	$100-400$	1	0.5
Coronal	10^{-3}	10^6		1	

Sellwood lectures.

Magnetic fields permeate all of gas phases. They are coupled to the gas, even in neutral phases, because of the residual degree of ionization, but are generally too weak to accelerate all but the lowest density gas. The field is therefore dragged around by bulk motions in the gas. It is known to be stronger in regions of higher gas density.

Coronal gas is out of present discussion. The phases of interest for magnetic field tracing consist of warm ionized gas (HII), cool atomic gas (HI), cool molecular gas (H_2) and cool dust. Although extensive surveys have shown the general extent of these phases, their volume filling factors are not well known. These are of interest as many physical processes in the ISM depend on the fraction of space occupied by the various phases. Furthermore, volume filling factors as a function of cloud size and cloud density give information on the size and mass distribution of the clouds if the mass-size relations are known.

From molecular cloud observations over a wide range of masses it is often suggested that there exists a power law scaling between size L and mass M of the form

$$M \propto L^{\kappa}, \tag{1.48}$$

where the slope κ ranges from 2 to 2.5 (Elmegreen & Falgarone 1996). Similarly, the density-size relation is

$$\bar{n} \propto L^{\kappa-3} \ \text{ in cm}^{-3} \text{ with } L \text{ in pc}, \tag{1.49}$$

where $\bar{n}$ is the average density of the cloud.

Table 1.5: Evidence for fractal structure. Abbreviations DZ1, DZ2, SS, EF are the references and the same as in Fig. 1.7. (* observed parameters, others derived)

phase		α_M	α_L	κ^*	D	p
HII	$L > 30\mathrm{pc}$	1.61	1.68	1.12	0.68	-0.70*
	$L < 30\mathrm{pc}$	1.65	2.30	2.0	1.30	-0.70*
HI		2.14	7.0	5.26	6.0	-1.8
Dust	DZ2	1.0	1.0*	2.0	0	-2.0
H_2	DZ1	1.6*	2.2*	2.0	1.2	-0.8
	SS	1.6*	2.26	2.10	1.26	-0.82
	EF	1.6*	2.41	2.41	2.35	-0.91

The *mass distribution* is the number of clouds per unit volume with mass between M and $M + dM$:

$$n(M)dM \propto M^{-\alpha_M} dM, \quad \text{in pc}^{-3} \text{ with } M \text{ in } \mathrm{M}_\odot, \tag{1.50}$$

where $\alpha_M = 1 + D/\kappa$ (see Table 1.5 for the slope α_M), D is the fractal dimension (Elmegreen & Falgarone 1996).

The *size distribution* is the number of clouds per unit volume with size between L and $L + dL$,

$$n(L)dL \propto L^{-\alpha_L} dL \ \text{ in pc}^{-3}, \tag{1.51}$$

where $\alpha_L = 1 - \kappa(1 - \alpha_M)$ (see Table 1.5).

The *volume filling factor* is the fraction of the volume occupied by the (spherical) clouds

$$f_V(L)dL = n(L)dL \frac{4\pi}{3} \left(\frac{L}{2}\right)^3, \tag{1.52}$$

or, using previous equation,

$$f_V(L)dL = q\bar{n}^p dL, \tag{1.53}$$

where q is a coefficient and $p = (2 - D)/(\kappa - 3)$ (Berkhuijsen 1999).

From Fig. 1.7 and Fig. 1.8 one can see, that the slopes in the case of HII and H_2 lines are the same, filling factors are of the same range. This suggests that the warm and the cool phase of the ISM have similar structure. Indices for the power laws (1.46)–(1.51) are listed in Tab. 1.5. The values of α_M are the same for both HII and H_2 and equal 1.6. These values are in a good agreement with the fractional Brownian motion structure proposed by Stutzki *et al.* (1998) for individual molecular clouds. Thus the large cloud samples of HII and H_2 have the same fractal properties as individual H_2 clouds. The atomic hydrogen is known to have the largest filling factor ($\sim 20\%$) and to be distributed almost homogeneously within the disk.

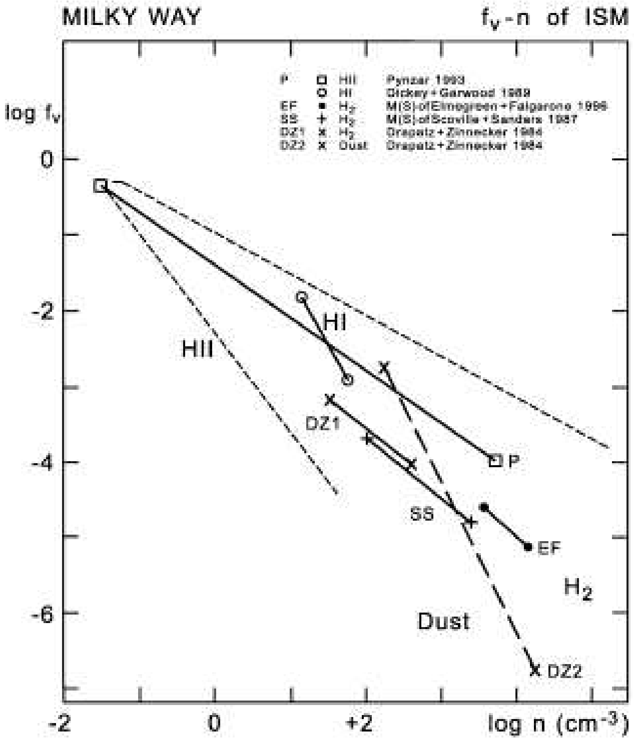

Figure 1.7: Volume filling factor f_V as a function of mean cloud density $\bar{n}$ of HII, HI, H_2 and dust. The full line for HII regions is an eyeball fit through the data in Pynzar (1993), the dashed lines indicate the range of HII regions collected by Berkhuijsen (1998). Notation: P gives HII obtained from Pynzar (1993), HI is from Dickey & Garwood (1989), EF gives H_2 from Elmegreen & Falgarone (1996), SS gives H_2 from Scoville & Sanders (1984), DZ1 and DZ2 give H_2 and dust from Drapatz & Zinnecker (1984)

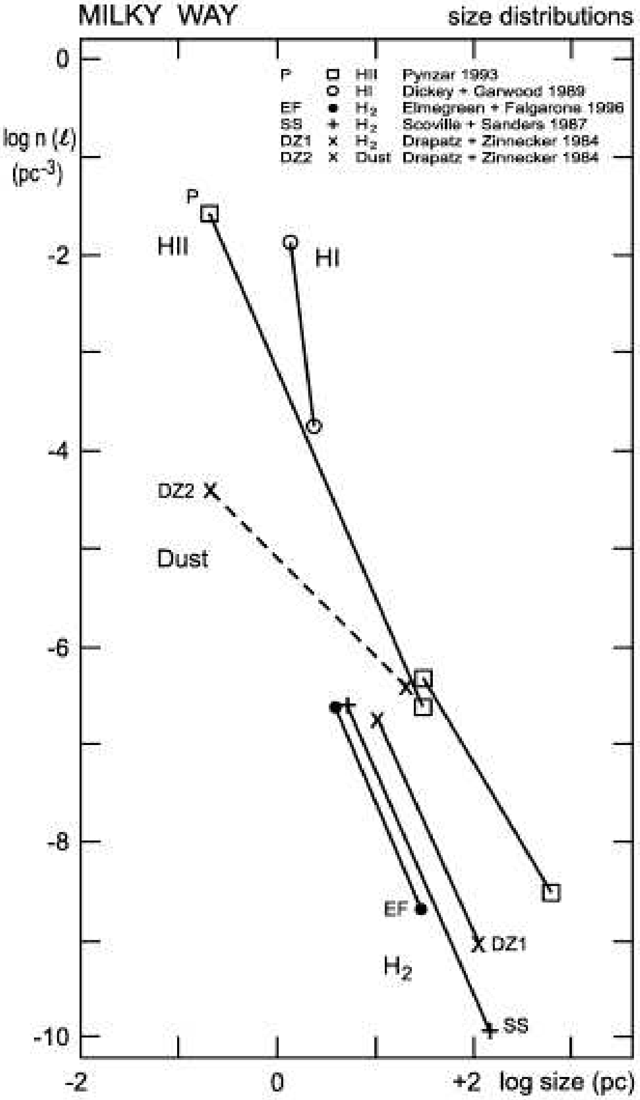

Figure 1.8: Cloud size distribution of HII, HI, H_2 and dust showing the number of clouds per unit volume with size between L and $L + dL$ as a function of L. Notation is the same as in Fig. 1.7

Radio wave scintillation ISM studies. The turbulence primarily responsible for radio wave scintillation resides in the low density ionized phase (DIG) and medium-density ionized (HII regions) envelopes.

The refraction of radio waves has been used to give statistical information on small-scale density inhomogeneities in the ionized gas. The rms scattering angle Θ_{s} results when an electromagnetic wave travels a distance z through a region in which the index of refraction m varies spatially. $\Theta_{\mathrm{s}} \sim \Delta n_e$, therefore the scattering angle gives the information about amplitude of density variations. The main results of radio wave (scintillation) ISM studies are the following ones (Spangler 1999):

- 'The Big Power Law in the Sky'; Density irregularities exist with scale sizes from $\geq 10^{18}\mathrm{cm} \rightarrow 10^{7}\mathrm{cm}$ (or from $\geq 1\mathrm{pc} \rightarrow 100\mathrm{km}$). The spectral index α which characterizes this spectrum is *close to, or equals* the Kolmogorov index $\alpha = 11/3$. This spectrum *suggests* a turbulent cascade in wavenumber through an inertial subrange to the dissipation range.

- *Extreme* variability in C_N^2 in the interstellar medium. C_N^2 is the normalization coefficient of the density power spectrum (Rickett 1990, Spangler 1999). It is directly proportional to the density variance, with a constant of proportionality that depends on the outer scale of the turbulence. Regions of very high C_N^2, termed 'fluctiferous regions' or *fluctifers* seem associated with HII regions and star formation regions. It is still unclear whether these variations represent turbulent intermittency or ISM spatial distribution.

- Irregularities are *anisotropic*, in the sense of being drawn along a symmetry axis, probably *defined by the interstellar magnetic fields*. Axial ratios of the broadened images, which are a lower limit to the axial ratios of the irregularities, are $\simeq 1.5 - 2.0$.

- Turbulent fluctuations in the magnetic field δB are detectable, with $\delta B/B_0 \leq \delta n/n_0$ (Minter & Spangler 1996, 1997). This result has been presented as evidence that the turbulence is highly compressible.

In his work Spangler (1999) had formulated a row of questions which are still not answered in theoretical works:

- Theoretical understanding of interstellar turbulence is missing. Better information about fluctuations in B can be obtained from Faraday rotation, and variations in V can be inferred from the timescale of scintillations. Promising preliminary results: Bondi et. al. 1994, Cordes & Rickett 1998, Rickett et al. 2000.

- It will be of interest to determine if the spectra in all turbulent quantities such as velocity and magnetic field are the same both perpendicular and parallel to the ISM magnetic field. MHD theory strongly indicates that the perpendicular and parallel spectra should be different, whereas no observational evidence of this has yet clearly emerged, either for the solar wind or for the interstellar medium.

- There is a need in ‘Purification of the ISM’ from highly dissipative Fast Mode Magneto-sonic waves. Even a small fraction of interstellar turbulence in Fast Mode waves would overwhelm the cooling capacity of the DIG.
- What generates the turbulence? Possibilities are shear flows, buoyancy-driven turbulence, kinetic plasma instabilities, and ‘star murmuring’. What would be correct explanation for multi-scale phenomena in the interstellar medium? Gravity and star formation affect large scales ($\geq\ 1\ \mathrm{pc}$), MHD nonlinearities cause a cascade to smaller scales.

Velocity dispersion in spiral galaxies. In the Milky Way the line widths of individual molecular and HI clouds and cloud complexes exceed the expected thermal width according to estimated kinematic temperatures. The 21 cm dispersion does not drop below 5–7 km/s, regardless of how low the optical surface brightness becomes. Obviously, interstellar turbulence does not decay in regions without star formation activity. A theoretical investigations of MRI-driven turbulence acting in a disk was applied to the particular case of NGC 1058, a face-on disk galaxy with a well-studied extended HI disk (Sellwood & Balbus 1999). This implied a magnetic field of about 3 μG which well agrees with observed field strengths of many galaxies.

1.5 MRI for galaxies?

Magneto-rotational instability (MRI) is a flexible and fast mechanism to generate the strong (few μG) magnetic fields. MRI is free to appear under most galactic physical conditions with the only requirement: the angular frequency of galactic rotation decreasing outwards, this condition is fulfilled for *any* spiral galaxy. The energy source for MRI is the differential rotation. A very weak external vertical magnetic flux is enough for the seed field.

MRI (see Chapter 5) generates 3D regular magnetic fields with many fluctuations, reversals, mixed dipole with quadrupole structure, and a mixture of m=0, m=1, m=2 modes. Thus, we are answering the most of the open questions posed by observation (field strength, large pitch angle, reversals, quadrupole and axial symmetry).

MRI is not expected to act alone in galaxies. Even when it is disturbed by SN, the seed field driven by MRI has the ideal properties for further dynamo operation. This should lead to the large-scale regular magnetic fields after 1 Gyr.

The feedback of magnetic fields onto the density field and velocity flows can be studied through the action of MRI. The instability is producing the disturbances of all field components. The structure of the turbulence will be analyzed in Chapter 5. MRI will be shown to generate a thin-sheet structures.

Galaxies for MRI to be applied to are following.

- NGC 4414, a flocculent galaxy with only circular velocity flow but great pitch angle.
- NGC 1058 with high velocity dispersion in outer part of the disk (~ 10 kpc).
- M51, the regions between arms. There is a puzzle about the origin of the $\sim 10\mu$G in inter-arm region, which later happens to be compressed along the dust regions up to $\sim 30\mu$G.
- The inter-arms magnetic fields of NGC 6946 were well explained within the dynamo theory, but as we know, there is no clue about the origin of the seed field. MRI may support with turbulent magnetic fields of large values.

Chapter 2

About the rotation laws

As it will be shown in the following chapter, the shape of the galactic differential rotation $\Omega(R)$ and especially the shear value $q = -d\ln\Omega(R)/d\ln R$ are the main parameters on which the growth rate of magneto-rotational instability depends. The dependence of pitch angle, velocity dispersion and other turbulent parameters on the rotation will be shown in the Chapter 5.

The rotation law can be described in two ways. One is a Brandt-type law,

$$u_\phi = \frac{RR_0\Omega_0}{(R^n + R_0^n)^{1/n}}, \tag{2.1}$$

where R_0 is the radius of transition from rigid to differential rotation, parameter n is describing the steepness of the transition, Ω_0 is the angular frequency of rigid galactic 'core' rotation. It is describing well the observed flatness of the rotation law. There is no evidence that the rigid 'core' is a correct way of central region behavior. On the contrary, most galaxies show the high velocity peak in the CO (1-0) emission near the galactic center. Although, there are certain doubts about the origin of these peaks. The decline of the rotational velocity outwards is claimed for some galaxies and cannot be described by Brandt-type law either. The combination of the Plummer model (spheroid)

$$\Psi_\mathrm{P} = -\frac{GM}{\sqrt{R^2+b^2}}, \tag{2.2}$$

with the Kuzmin model (flat disk)

$$\Psi_\mathrm{K} = -\frac{GM}{\sqrt{R^2+(a+|Z|)^2}}, \tag{2.3}$$

gives the potential called Plummer-Kuzmin

$$\Psi_\mathrm{PK} = -\frac{GM}{\sqrt{R^2+(a+\sqrt{Z^2+b^2})^2}}. \tag{2.4}$$

The Miyamoto-Nagai (1975) gravitational potential can be used for the reproduction of the velocity decline outwards and the inner peaks by a superposition of halo, disk, bulge and the spheroid potentials

$$\Psi_{\mathrm{MN}} = -\sum_{i=1}^{N} \frac{GM_i}{\sqrt{R^2 + (a_i + \sqrt{Z^2 + b_i^2})^2}}, \tag{2.5}$$

where M_i, a_i and b_i are the mass, scale radius and scale thickness of the ith mass component of the galaxy.

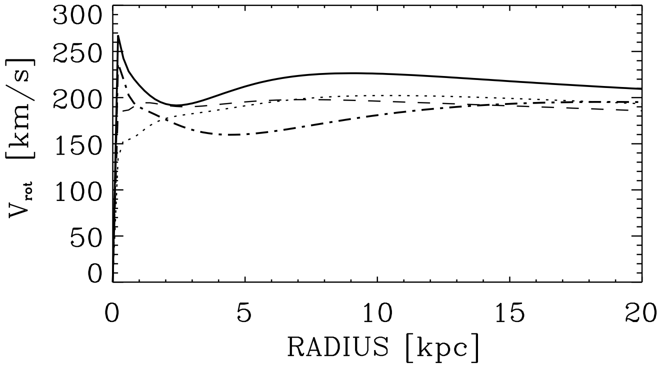

Figure 2.1: Sofue (1996) rotation curves: Solid line for Our Galaxy, dotted is for IC 342, dashed line is for NGC 235 and dash-dot is for NGC 6946

The most complete compilation of the galactic rotation curves were done by Sofue (1996), the examples are shown in Fig. 2.1. The parameters are listed in Tab. 2.1. When the inner peak (nucleus) is taken into account as gravitational effect, the (not normalized) shear strength is about of order 10^3 in the inner part, while without nucleus it is between 20 and 80. The local MRI linear theory estimation gives the growth rates ($\gamma = 0.5q\Omega$) of the high order, up to $10^3\mathrm{Gyr}^{-1}$. Here one should remember the argumentation from Korpi et. al. (2003). From energy considerations it is clear that the MRI will not be important in regions with high stellar activity, or with large stellar populations as it happens in the very inner part of a galaxy. Therefore, one may use a Brandt-type law for the description of rotation without loosing the information about MRI action near the galactic center.

Another important discussion is about the outer rotation of gaseous and stellar disks. From Table 2.1 the most important case for the present work is the example of NGC 4414. It is one of the best studied dynamo candidates. There are no magnetic spiral waves, but a large pitch angle for magnetic fields. Vallejo et al. (2002) and Braine et al. (1993) claimed an unusually small halo and decline of the rotation curve outwards, while the work of Thornley & Mundy (1997) shows no strong evidence for a small halo and their rotation curve is much flatter. The

Table 2.1: Parameters for Miyamoto-Nagai modeling for some spiral galaxies

sample	component	M [10^{11}M$_\odot$]	a [kpc]	b [kpc]	reference
Galaxy	bulge	0.2	1.0	1.0	Binney & Tremaine (1990)
	disk	0.6	0.5	~ 0	
	halo	1.0	~ 0	~ 30	
Galaxy	nucleus	0.05	0.00	0.12	Sofue (1996)
	bulge	0.10	0.00	0.75	
	disk	1.60	6.00	0.50	
	halo	3.00	15.00	15.00	
NGC 6946	nucleus	0.05	0.00	0.15	Sofue (1996)
	bulge	0.14	0.00	1.25	
	disk	1.30	6.00	0.50	
	halo	2.00	10.00	10.00	
NGC 253	nucleus	0.03	0.00	0.16	Sofue (1996)
	bulge	0.15	0.00	1.00	
	disk	0.80	5.00	0.50	
	halo	2.00	10.00	10.00	
IC 342	nucleus	0.03	0.00	0.24	Sofue (1996)
	bulge	0.20	0.00	1.60	
	disk	1.20	7.00	0.50	
	halo	2.00	12.00	12.00	
NGC 4414	nucleus	0.03	0.07	0.09	Vallejo et al. (2002)
	bulge	0.04	0.38	0.03	
	disk	0.86	2.50	0.15	
	halo	0.16	11.00	0.50	

paper of Sakamoto (1996) can cause confusion. The clear rigid-core rotation is demonstrated out to $R = 1.39$ kpc, with the surface density (H_2 & HII) peak at 0.93 kpc. The last rotation curve can be described by a Brandt-type law

$$u_\phi = 140[\mathrm{km/s}] + 1.39[\mathrm{kpc}]58[\mathrm{Gyr}^{-1}]R/\sqrt{R^2 + (1.39[\mathrm{kpc}])^2}, \tag{2.6}$$

where the angular frequency of $58[\mathrm{Gyr}^{-1}]$ is small for fast MRI growth. NGC 4414 rotation curve in Fig. 2.2 is taken from Braine et al. (1993), HII data. The decline of rotation velocity down to 150 km/s is not confirmed by Thornley & Mundy (1997), their rotation curve reaches the value of 180 km/s only at 21 kpc.

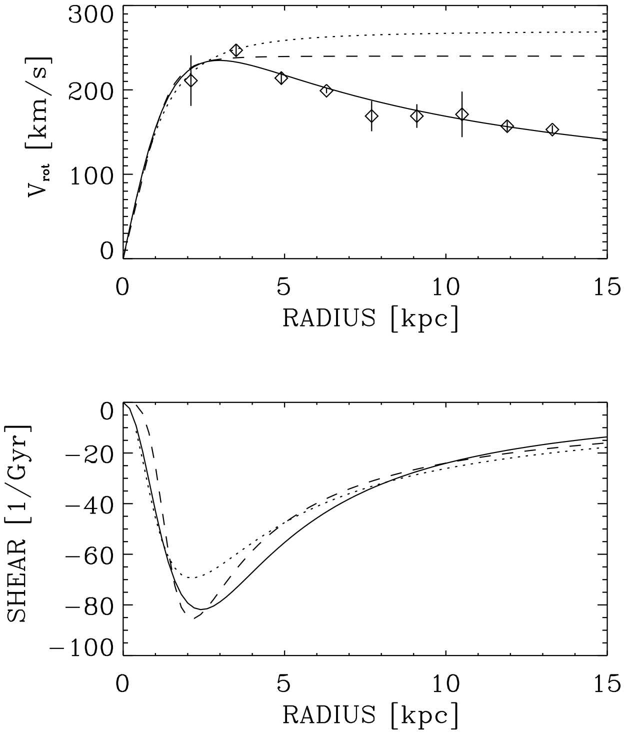

Figure 2.2: NGC 4414 rotation curve. Points with error bars show the results of H II observations by Braine (1993), which eye-fitting (solid line) is obtained using Miyamoto-Nagai gravitational potential (Eq. (2.5)) with only disk ($a_{\mathrm{disk}} = 2.0$, $b_{\mathrm{disk}} = 0.1$, $M_{\mathrm{disk}} = 7 \cdot 10^{10}\ \mathrm{M}_\odot$) and small halo ($a_{\mathrm{halo}} = 12.0$, $b_{\mathrm{halo}} = 12.0$, $M_{\mathrm{halo}} = 10^{10}\ \mathrm{M}_\odot$) components. Dotted line is for Brandt-type law with $n = 2$, $\Omega_0 = 180\ \mathrm{Gyr}^{-1}$ and $r_0 = 1.5$ kpc. Dashed line is a Brandt-type law with $n = 4$, $\Omega_0 = 160\ \mathrm{Gyr}^{-1}$ and $r_0 = 1.5$ kpc

In addition to the confusion about both inner and outer shape of u_ϕ, there are strange results of magnetic pitch angle observation (Soida et al. 2002). Although the galaxy shows no evidence for radial velocity flows or rich SN activity, there are large pitch angles from 0^o to -80^o for radii from $0.69\ \mathrm{kpc}$ to $3.41\ \mathrm{kpc}$. The strongest values belongs to the region of so-called 'rigid' rotation, if to use Sakamoto rotation curve. It means zero shear and no magneto-rotational instability (see Chapter 3), while the surface density is sub-critical for gravitational instability of the gas (Sakamoto 1996). It is an open question then by which mechanism the high turbulence in the inner region is generated. The high pitch-angles can be explained well by a dynamo operating with unusually strong turbulence, $\sqrt{\boldsymbol{u}'^2} \sim 25$ km/s.

The velocity dispersion is behaving mysteriously: it is decaying from 25 km/s to 7 km/s from the central hole up to the radius of 5 kpc. The decay is linear, crossing both 'rigid' transition radius and gravitational instability radius without being affected. This phenomenon should be checked with better resolution for other spiral galaxies. Theoretical explanation is still lacking.

NGC 4414 has unusually high surface density both for molecular and atomic hydrogen. The density is expected to be 10 times higher than for the Milky Way Galaxy. But the higher density of the gas is not changing the viscosity sufficiently, as one can see from later estimations (see Chapter 3).

NGC 4414 is an ideal object for this kind of study, as it is an unperturbed object at high galactic latitude with very extended atomic gas (HI). NGC 4414 is quite axisymmetric, with no bar and poorly defined spiral structure, and the center is seen un-obscured (no CO, HI or thermal dust emission near the nucleus), as in many isolated spiral galaxies. Braine et al. (1993) have developed an axisymmetric analytical gravitational potential model to account for the central light profile, the dynamics of the molecular gas in the highly obscured molecular ring, and the stellar light profile outside the highly obscured region. A single dominant disk component reproduces the disk dynamics and outer stellar light profile such that even if other disk components were present they would not affect our results. The contribution of dark matter is constrained by the extremely extended HI rotation curve. It is small and possibly negligible at distances less than 5–7 kpc from the center.

NGC 4414 is an Sc(sr) late-type spiral that has been classified as flocculent by Elmegreen & Elmegreen (1982, 1987) and put in the same class as the prototype NGC 2841, due to "fragmented arms uniformly distributed around the galactic center". A blue photograph of the galaxy can be found in the NASA atlas from Sandage & Bedke (1988). Very strong CO emission was detected, which did not appear strongly peaked towards the nucleus. The $\mathrm{H}\alpha$ image published by Pogge (1989) indicates a complete lack of massive stars – and hence presumably recent star formation – in the nucleus. Reproducing the central spectrum in both lines is easily possible with a central hole and a quickly rising rotation curve without substantial overshooting of the terminal rotation velocity (Braine et. al 1993).

The neutral gas surface density in the disk is one of the highest known, about 50 $\mathrm{M_{\odot}pc^{-2}}$, comparable to that of the grand design galaxy M51. Chini et. al. (1986) found that this galaxy had the largest cool to warm dust ratio and predicted a neutral gas mass of over 10^{10} $\mathrm{M}_{\odot}$.

The HI disk extends far beyond the optical outlines of the galaxy, and it is quite asymmetric at low column densities. A combined CO(2-1) and HI rotation curve shows that the rotation velocities start declining outside the optical disk, a phenomenon found only in compact galaxies with high rotational velocities. Therefore, no direct evidence for a massive dark halo in NGC4414 is found from the rotation curve, a rare case for a Sc spiral.

Chapter 3

Magneto-Rotational Instability

Magnetic fields are often assumed to be weak and not important for galaxies. The stellar disk exists uninfluenced by the magnetic field. But magnetic fields are in equipartition with the turbulence (Section 1.1). The velocity field of the gas was treated very often as a given flow in simulations and the magnetic field generation by gas flows was studied. This situation is characterized by the inequality

$$\frac{\langle B\rangle^2}{8\pi} \ll \frac{\rho\langle u\rangle^2}{2}, \tag{3.1}$$

where $\langle B\rangle$, $\langle u\rangle$ are the mean magnetic and velocity fields. The observed strength of magnetic fields is not sufficient to change the rotation law ($u_\phi \sim 100 - 200\mathrm{km/s}$), but it will be important on the turbulent scales.

The classical picture for interstellar matter turbulence is that supernovae (SN) and other stellar processes maintain turbulent cloud velocities great enough to survive the dissipative losses. Other source of turbulent velocities can be a Magneto-Rotational Instability (MRI). The instability requires only the presence of weak poloidal component and also requires that the angular velocity be decreasing outward (Balbus & Hawley 1991). Sellwood & Balbus (1999) proposed that MHD instabilities in the differentially rotating gas layers are responsible for a minimum level of turbulence in the differentially rotating gas disks.

3.1 Introduction to MRI

Galactic and Keplerian disks are hydrodynamically stable configurations according to the Rayleigh stability criterion

$$\frac{dj^2}{dR} > 0, \tag{3.2}$$

where R is the radius and $j = R^2\Omega$ is the angular momentum per unit mass. But rotation has not only radial but also vertical dependence. Urpin & Brandenburg (1998) and Arlt & Urpin (2004) consider the destabilizing action of a dependence of Ω on z, which may more than compensate the stabilization due to Eq. (3.2). There is a suggestion by Klahr & Bodenheimer (2003) that the negative radial entropy S stratification in thin Kepler disks may act as destabilization. One finds, however, positive value $\partial S/\partial R$ in the standard α description. The vertical density stratification may have a destabilizing effect, as was reported for Taylor-Couette flows (Molemaker et al 2001). The Schwarzschild criterion

$$\partial S/\partial z > 0 \tag{3.3}$$

is a *sufficient condition for stability* of disks even when combined with vertical density stratification and differential (Keplerian) rotation. Solberg-Høiland criterion is a local *necessary condition for stability,*

$$\frac{\partial g_R}{\partial z} = \frac{\partial g_z}{\partial R}, \tag{3.4}$$

where g_R and g_z are the combined forces terms from momentum conservation equations. Any *conservative force* is a solution of Eq. (3.4). Without external forces this relation is thus always locally fulfilled. Eq. (3.4) have been derived by means of the short-wave approximation. For the Kepler flows with density stratification, the strato-rotational instability arises in the case of the global analysis.

Nevertheless, gaseous disks with sufficiently high conductivity are unstable under the influence of a weak magnetic field. The magneto-rotational instability has been known for more than four decades (Velikhov 1959; Chandrasekhar 1960, 1961), but the importance for accretion disks was first pointed out by Hawley & Balbus (1991). Steven A. Balbus and John F. Hawley obtained a remarkable success in the investigations of a powerful local shear instability in weakly magnetized disks. Balbus & Hawley (1991, 1992 and subsequent works) showed that a broad class of astrophysical accretion disks is dynamically unstable to axisymmetrical disturbances in the presence of a weak magnetic field. Because of the ubiquity of magnetic fields, the result bears upon gaseous differentially rotating systems quite generally.

The instability is extremely powerful. The growth rate is of order of the angular rotation velocity and is *independent* of the strength of the magnetic field. The instability requires only the presence of weak magnetic fields (poloidal component for unstable axisymmetrical mode and the toroidal component for non-axisymmetrical modes), and also requires the angular velocity to be decreasing outward.

In brief, the mechanism of the instability is the following. Consider an outwardly displaced fluid element in a differentially rotating disk threaded by a vertical magnetic field. The fundamental point is that the element is elastically threaded by a magnetic field which is trying simultaneously to enforce rigid rotation by resisting shearing, and to return the element back to its starting point by resisting stretching. The latter is clearly stabilizing, but the first is at the heart of the instability: the field is trying to force the element to rotate too fast for its new radial location. The excess centrifugal force drives the element still further outward. At long wavelengths, the return force is weak, and destabilization wins. The presence of a finite vertical wavenumbers in the disturbance is essential; there can be no axisymmetrical instability otherwise. This allows fingers of high and low angular momentum fluid to interpenetrate. The instability is basically simple.

The linear analysis of MRI can be split in two parts: instability of axisymmetric (m=0) and of non-axisymmetric ($k_\phi \neq 0$) disturbances. The axisymmetric case is more simple to perform. The basic dynamic equations are

$$\frac{D \ln \rho}{Dt} + \nabla \cdot \boldsymbol{u} = 0, \tag{3.5}$$

$$\frac{D\boldsymbol{u}}{Dt} + \frac{1}{\rho}\nabla P + \nabla\Psi - \frac{1}{4\pi\rho}\boldsymbol{B} \times [\nabla \times \boldsymbol{B}] = 0, \tag{3.6}$$

$$\frac{\partial \boldsymbol{B}}{\partial t} - \nabla \times (\boldsymbol{u} \times \boldsymbol{B}) = 0. \tag{3.7}$$

The notation D/Dt indicates the Lagrangian derivative, Ψ is an external gravitational potential, P is pressure. Other symbols have their usual meanings ($\boldsymbol{u}$ for velocity fields, $\boldsymbol{B}$ for magnetic fields and ρ for density).

Simplest derivation of MRI. We consider the $\boldsymbol{u}$ and $\boldsymbol{B}$ fields having mean and fluctuating parts

$$\boldsymbol{u} = \langle \boldsymbol{u} \rangle + \boldsymbol{u}^{'}, \quad \boldsymbol{B} = \langle \boldsymbol{B} \rangle + \boldsymbol{B}^{'}. \tag{3.8}$$

After substitution of Eq. (3.8) in the induction equation (3.7), the averaging over the space and subtracting the equation of the mean fields, we obtain the equation for the fluctuations

$$\frac{\partial \boldsymbol{B}^{'}}{\partial t} = \nabla \times [\langle \boldsymbol{u} \rangle \times \boldsymbol{B}^{'} + \boldsymbol{u}^{'} \times \langle \boldsymbol{B} \rangle]. \tag{3.9}$$

Due to the relations $\nabla \cdot \boldsymbol{B} = 0$ and $\nabla \cdot \boldsymbol{u} = 0$ some terms have been canceled. Fluctuations of the fields are $\boldsymbol{u}^{'}, \boldsymbol{B}^{'} \sim \exp(\mathrm{i}\boldsymbol{k}\boldsymbol{x} + \gamma t)$.

$$\gamma \boldsymbol{B}^{'} = R(\boldsymbol{B}^{'} \cdot \nabla\Omega)\hat{\boldsymbol{e}}_{\boldsymbol{\phi}} + \mathrm{i}(\langle \boldsymbol{B} \rangle \cdot \boldsymbol{k})\boldsymbol{u}^{'}. \tag{3.10}$$

From the substitute of Eq. (3.8) in the momentum equation (3.6), after standard routine of averaging and subtracting the mean-field equation from the Eq. (3.6), one gets the momentum equation for fluctuations

$$\frac{\partial \boldsymbol{u}^{'}}{\partial t} + (\langle \boldsymbol{u} \rangle \nabla)\boldsymbol{u}^{'} + (\boldsymbol{u}^{'}\nabla)\langle \boldsymbol{u} \rangle = -\frac{1}{\rho}\nabla P^{'} + \frac{1}{4\pi\rho}(\boldsymbol{B}^{'} \times [\nabla \times \langle \boldsymbol{B} \rangle] + \langle \boldsymbol{B} \rangle \times [\nabla \times \boldsymbol{B}^{'}]). \tag{3.11}$$

If we consider again the constant mean magnetic field, then this relation can be transformed to

$$\gamma \boldsymbol{u}^{'} + \mathrm{i}(\hat{\boldsymbol{e}}_{\boldsymbol{\phi}}\boldsymbol{k}_{\boldsymbol{\phi}})\Omega \boldsymbol{u}^{'} + 2\boldsymbol{\Omega} \times \boldsymbol{u}^{'} + R(\boldsymbol{u}^{'}\nabla)\Omega\hat{\boldsymbol{e}}_{\boldsymbol{\phi}} =$$

$$= -\frac{\mathrm{i}\boldsymbol{k}}{\rho}P' - \frac{\mathrm{i}}{4\pi\rho}(\boldsymbol{k}(\langle\boldsymbol{B}\rangle\cdot\boldsymbol{B}') - (\langle\boldsymbol{B}\rangle\cdot\boldsymbol{k})\boldsymbol{B}'), \tag{3.12}$$

and assuming the axisymmetrical perturbations we can simplify it to

$$\gamma\boldsymbol{u}' + 2\boldsymbol{\Omega}\times\boldsymbol{u}' + R(\boldsymbol{u}'\nabla)\Omega\hat{\boldsymbol{e}}_{\boldsymbol{\phi}} =$$

$$= -\frac{\mathrm{i}\boldsymbol{k}}{\rho}P' - \frac{\mathrm{i}}{4\pi\rho}(\boldsymbol{k}(\langle\boldsymbol{B}\rangle\cdot\boldsymbol{B}') - (\langle\boldsymbol{B}\rangle\cdot\boldsymbol{k})\boldsymbol{B}'). \tag{3.13}$$

From Eq. (3.10) we see that

$$\boldsymbol{u}' = (\gamma\boldsymbol{B}' - R(\boldsymbol{B}'\nabla\Omega)\hat{\boldsymbol{e}}_{\boldsymbol{\phi}})/(\mathrm{i}\langle\boldsymbol{B}\rangle\cdot\boldsymbol{k}). \tag{3.14}$$

Now we assume for simplicity $\boldsymbol{u}' = \tilde{\boldsymbol{u}}/\mathrm{i}(\langle\boldsymbol{B}\rangle\cdot\boldsymbol{k})$, which makes the equation (3.12) look simpler. We find

$$\gamma\tilde{\boldsymbol{u}}+2\boldsymbol{\Omega}\times\tilde{\boldsymbol{u}}+R(\tilde{\boldsymbol{u}}\nabla)\Omega\hat{\boldsymbol{e}}_{\boldsymbol{\phi}} = (\langle\boldsymbol{B}\rangle\cdot\boldsymbol{k})\left(\frac{\boldsymbol{k}}{\rho}P' + \frac{1}{4\pi\rho}(\boldsymbol{k}(\langle\boldsymbol{B}\rangle\cdot\boldsymbol{B}') - (\langle\boldsymbol{B}\rangle\cdot\boldsymbol{k})\boldsymbol{B}')\right). \tag{3.15}$$

Introducing the Alfvén frequency $\omega_{\mathrm{A}}^2 = (\langle\boldsymbol{B}\rangle\cdot\boldsymbol{k})^2/4\pi\rho$ and Alfvén velocity $\boldsymbol{V}_{\mathrm{A}} = \langle\boldsymbol{B}\rangle/\sqrt{4\pi\rho}$, we change it to

$$\gamma\tilde{\boldsymbol{u}} + 2\boldsymbol{\Omega}\times\tilde{\boldsymbol{u}} + R(\tilde{\boldsymbol{u}}\nabla)\Omega\hat{\boldsymbol{e}}_{\boldsymbol{\phi}} = -\omega_{\mathrm{A}}^2\boldsymbol{B}' + \boldsymbol{k}(\boldsymbol{V}_{\mathrm{A}}\cdot\boldsymbol{k})\tilde{P}, \tag{3.16}$$

where

$$\tilde{P} = \sqrt{4\pi\rho}\left(\frac{P'}{\rho} + \frac{1}{4\pi\rho}(\langle\boldsymbol{B}\rangle\cdot\boldsymbol{B}')\right). \tag{3.17}$$

For further equations we use the notation for $\tilde{\omega}^2 = \gamma^2 + \omega_{\mathrm{A}}^2$, the shear frequency

$$\omega_{\mathrm{sh}} = d\Omega/d\ln R \tag{3.18}$$

and the epicyclic frequency

$$\kappa^2 = \frac{2\Omega}{R}\frac{d(R^2\Omega)}{dR}. \tag{3.19}$$

The relation $4\Omega^2 = \kappa^2 - 2\Omega\omega_{\mathrm{sh}}$ has been used. Substituting of Eq. (3.14) in Eq. (3.16) leads to

$$\tilde{\omega}^2 B_z' = k_z(\boldsymbol{V}_{\mathrm{A}}\cdot\boldsymbol{k})\tilde{P}, \tag{3.20}$$

$$(\tilde{\omega}^2 + 2\Omega\omega_{\mathrm{sh}})B_R' - 2\gamma\Omega B_\phi' = k_R(\boldsymbol{V}_{\mathrm{A}}\cdot\boldsymbol{k})\tilde{P}, \tag{3.21}$$

$$\gamma\left(\frac{\kappa^2}{2\Omega} - \omega_{\mathrm{sh}}\right)B_R' + \tilde{\omega}^2 B_\phi' = 0. \tag{3.22}$$

Substituting Eq. (3.22) and Eq. (3.20) into Eq. (3.21) we arrive at

$$B_R'\left(\tilde{\omega}^4 + \tilde{\omega}^2\kappa^2 - \omega_{\mathrm{A}}^2(\kappa^2 - 2\Omega\omega_{\mathrm{sh}})\right) = \frac{k_R}{k_z}\tilde{\omega}^4 {B'}_z. \tag{3.23}$$

Next, we may use the zero-divergence condition for magnetic fields $B'_z \simeq -B'_R k_R/k_z$, assuming that $k_\phi \sim 1/R \ll k_R$.

$$\tilde{\omega}^4 + \tilde{\omega}^2\kappa^2 - \omega_{\rm A}^2(\kappa^2 - 2\Omega\omega_{\rm sh}) = -\frac{k_R^2}{k_z^2}\tilde{\omega}^4, \tag{3.24}$$

which is the same as

$$\tilde{\omega}^4\left(\frac{k^2}{k_z^2}\right) + \tilde{\omega}^2\kappa^2 - 4\Omega^2\omega_{\rm A}^2 = 0. \tag{3.25}$$

For simplicity, we use the following notations

$$\tilde{\omega}^4 A_0 + \tilde{\omega}^2 A_1 + A_2 = 0. \tag{3.26}$$

The instability condition is the $\gamma^2 > 0$.
i) Case with $A_1 + 2A_0\omega_{\rm A}^2 < 0$ leads to the condition

$$\frac{1}{2A_0}\frac{1}{R}\frac{\partial(R^2\Omega)}{\partial R} + \omega_{\rm A}^2 < 0. \tag{3.27}$$

Comparing Eq. (3.27) with the Rayleigh criterion of Eq. (3.2) we can see that magnetic fields are playing a stabilization role for hydrodynamically unstable disks.
ii) In case where $A_1+2A_0\omega_{\rm A}^2 > 0$, one has to solve $A_1^2-4A_0A_2 > (A_1+2A_0\omega_{\rm A}^2)^2$. It is easy to show that the resulting *instability condition* is

$$A_0\omega_{\rm A}^2 < -\frac{\partial\Omega^2}{\partial\ln R}. \tag{3.28}$$

For the flow with $\Omega \sim \Omega_0 R^{-q}$ ($q = -\partial\ln\Omega/\partial\ln R$ is the normalized shear), one can estimate

$$k < \sqrt{2q}\frac{\Omega_0}{V_{\rm A}}, \tag{3.29}$$

$$\gamma \simeq \sqrt{2q}\omega_{\rm A} \leq 2q\Omega_0. \tag{3.30}$$

Compared to dynamo growth rates (Section 1.2.2), the MRI is a very fast amplification mechanism.

The ratio of the critical wavelength over disk thickness is

$$\frac{\lambda_{\rm crit}}{2H} = \frac{\pi V_{{\rm A}z}}{\sqrt{2q}H\Omega_0} \quad \text{or} \quad \beta = \frac{\pi^2}{2q}\left(\frac{\lambda_{\rm crit}}{2H}\right)^{-2}. \tag{3.31}$$

Instability cannot evolve if the critical wavelength is exceeding the disk thickness. Eq. (3.31) can be used as the restricting condition of the initial field strength, as

$$V_{{\rm A}z}|_{\rm max} = \frac{\sqrt{2q}}{\pi}H\Omega_0. \tag{3.32}$$

For the Keplerian disks the relation $c_{\rm s} = H\Omega_0$ can be easily derived from the point-mass gravitational potential, therefore the Eq. (3.32) can be transformed to

$V_{\mathrm{A}z}|_{\max} \simeq c_{\mathrm{s}}$. The galactic disk is self-gravitating and its thickness is defined by the stellar motions. One can derive a similar relation $c_{\mathrm{s}}^{*} \propto H\Omega_0$ for isothermal stellar disk, using the stellar sound speed c_{s}^{*} (Rüdiger 1990). The sound speed of the gas is not necessarily the same, although it is found to be close to the stellar one. For $\beta < 3$ we do not expect the instability to be excited.

Axisymmetric dispersion relation for adiabatic disks. The adiabatic case differs from the isothermal one by adding more hydrodynamical frequencies. The *axisymmetrical* large-wavenumber Eulerian perturbations $e^{\mathrm{i}(k_R R + k_z z - \omega t)}$ were considered within the Boussinesq approximation (Balbus & Hawley 1991). The equations may be rewritten in a component form, with the largest Fourier amplitudes of perturbed flow $\delta\rho$, δP, δu_z, etc. being only retained. The simplified form of the dispersion relation is

$$\frac{k_z^2}{k^2}\left[\frac{3}{5\rho}\left(\frac{k_R}{k_z}\frac{\partial P}{\partial z} - \frac{\partial P}{\partial R}\right)\left(\frac{k_R}{k_z}\frac{\partial \ln P\rho^{-5/3}}{\partial z} - \frac{\partial \ln P\rho^{-5/3}}{\partial R}\right) - \kappa^2\right]\tilde{\omega}^2 +$$

$$+\tilde{\omega}^4 - 4\Omega^2\frac{k_z^4 V_{\mathrm{A}z}^2}{k^2} = 0, \tag{3.33}$$

where $V_{\mathrm{A}z} = B_z/\sqrt{4\pi\rho}$ is the vertical component of the Alfvén speed, frequency $\tilde{\omega}^2 = \omega^2 - k_z^2 V_{\mathrm{A}z}^2$, wavelength $k^2 = k_z^2 + k_R^2$ and κ is the epicyclic frequency (Eq. (3.19)). A similar dispersion equation was obtained by Fricke (1969), but he was considering the purely toroidal field case which is considerably more restrictive. For further simplification the assumption of constant rotation on cylindrical surfaces was taken

$$\frac{\partial P}{\partial R}\frac{\partial \ln P\rho^{-5/3}}{\partial z} = \frac{\partial P}{\partial z}\frac{\partial \ln P\rho^{-5/3}}{\partial R}, \tag{3.34}$$

what is the same as to assume that isobaric and isochoric surfaces coincide. The final form of the dispersion relation then has a simple form:

$$\frac{k^2}{k_z^2}\tilde{\omega}^4 - \left[\kappa^2 + \left(\frac{k_R}{k_z}N_z - N_R\right)^2\right]\tilde{\omega}^2 - 4\Omega^2 k_z^2 V_{\mathrm{A}z}^2 = 0, \tag{3.35}$$

where N_z^2 and N_R^2 are the parts of Brunt-Väisälä frequency

$$N^2 = \frac{3}{5\rho}(\nabla P)\cdot(\nabla \ln P\rho^{-5/3}) = N_z^2 + N_R^2. \tag{3.36}$$

Note, that only the *vertical* component of the magnetic field enters the dispersion relation, multiplied by the wavenumber k_z. Later nonlinear studies proved that the axisymmetrical disturbances due to MRI are indeed not sensitive to the toroidal component of the initial magnetic field (Hawley & Balbus 1991). The importance of small magnetic fields are easily understood from Eq. (3.35): significant magnetic tension forces can be generated at sufficiently small wavelengths. The value of the wavenumber is proportional to $\Omega/V_{\mathrm{A}z}$. Thus, it does not depends on the magnetic field alone. In the absence of magnetic fields, internal waves propagate with a frequency that depends only on wavenumber direction. Tightly wound internal waves have been suggested as a means of angular momentum transport and dynamo activity in accretion disks (Vishniac & Diamond 1989; Vishniac et al. 1990). But these studies assumed that the magnetic field has a negligible effect on the wave propagation properties, at least if the magnetic pressure is small compared with the thermal pressure. For any weakly magnetized disk the equation (3.35) shows that the assumption was not correct.

For further analysis one has to assume the disk to be hydrodynamically stable, i.e. the epicyclic and Brunt-Väisälä frequencies are real. In case of vanishing Brunt-Väisälä frequency the Eq. (3.35) is identical to Eq. (3.25). Now the stability of the weakly magnetized disk can be analyzed by considering the conditions in the neighborhood of $\omega^2 = 0$, or $\tilde{\omega}^2 = -k_z^2 V_{\mathrm{A}z}^2$. In this limit, equation (3.33) can be written:

$$k_R^2(k_z^2 V_{\mathrm{A}z}^2 + N_z^2) - 2k_R k_z N_R N_z + k_z^2 \left(\frac{d\Omega^2}{d\ln R} + N_R^2 + k_z^2 V_{\mathrm{A}z}^2 \right) = 0. \quad (3.37)$$

The last equation is quadratic in k_R. Its discriminant is negative, there will be no real solutions for k_R and thereby ω^2 is not allowed to pass through zero. This requirement is in fact the stability criterion and expressed as:

$$k_z^4 V_{\mathrm{A}z}^4 + k_z^2 V_{\mathrm{A}z}^2 \left(N^2 + \frac{d\Omega^2}{d\ln R} \right) + N_z^2 \frac{d\Omega^2}{d\ln R} > 0 \quad \text{(stability)}. \quad (3.38)$$

The critical wavenumber can be derived from the same equation

$$(k_z)^2_{\mathrm{crit}} = \frac{1}{2V_{\mathrm{A}z}^2} \left(\left[\left(N^2 + \frac{d\Omega^2}{d\ln R} \right)^2 - 4N_z^2 \frac{d\Omega^2}{d\ln R} \right]^{1/2} - \left[N^2 + \frac{d\Omega^2}{d\ln R} \right] \right). \quad (3.39)$$

For the disks rotating supersonically ($N_R^2 \ll N_z^2$) or if N^2 is negligible we have the condition identical to (3.29),

$$|(k_z)_{\mathrm{crit}}| = V_{\mathrm{A}z}^{-1} |d\Omega^2/d\ln R|^{1/2}, \quad (3.40)$$

whereas the *stability criterion* differs for the case of supersonic rotation velocities

$$N_R^2 + \frac{d\Omega^2}{d\ln R} \geq 0 \quad \text{(stability)}. \quad (3.41)$$

The turbulence in the gaseous disk is subsonic.

The best known density profile is for the Milky Way Galaxy described by Dickey & Lockmann (1990). It is a superposition of Gaussians and exponentials for different gas components. In a simple form one can write

$$\rho = \rho_0 \exp{(-z^2/H^2)}. \tag{3.42}$$

The galactic gaseous disk is not becoming thicker with radius, therefore the external gravitational potential is usually split in two parts $\Psi = \Psi(z) + \Psi(R)$. For hydrodynamical stability, the vertical component of the momentum equation is solved

$$\frac{1}{\rho}\frac{\partial P}{\partial z} = -\frac{\partial \Psi(z)}{\partial z}. \tag{3.43}$$

The potential $\Psi(z)$ is derived in order to fit the observed density distribution. From the known galactic density profile and the rotation, we obtain the $N_R = 0$ and $\kappa^2 = 2\Omega^2$. The epicyclic frequency is $\kappa^2 = \Omega^2$ for Kepler disk and $\kappa^2 = 5\Omega^2$ for outwardly increasing shear. The largest growth rates are expected to match the prediction for Kepler disks $\gamma < 0.5q\Omega$.

Inviscid approximation for galaxies From numerous studies (Kitchatinov & Rüdiger 2004; links in Rüdiger & Hollerbach 2004) we know that the plasma can be assumed to be a 'frozen in' gas for warm neutral medium. The magnetic diffusivity is

$$\eta = 10^{13} T^{-3/2} \left(\frac{\ln \Lambda}{20}\right) \mathrm{cm}^2/\mathrm{s}, \tag{3.44}$$

where $\ln \Lambda \sim 20$ is the Coulomb logarithm (Spitzer 1962). Adopting $T \sim 10^4$ K for the characteristic temperature, we find

$$\eta \simeq 10^7 \mathrm{cm}^2/\mathrm{s}. \tag{3.45}$$

Assuming the typical galactic rotation $\Omega \simeq 3 \times 10^{-15} \mathrm{s}^{-1}$ (Sofue 1996) and half-thickness of $H = 300\mathrm{pc}$, the magnetic Reynolds number will be

$$\mathrm{Rm} \simeq 3 \times 10^{20}. \tag{3.46}$$

The viscosity can be estimated using the expression for a fully-ionized plasma from Spitzer (1962)

$$\nu = 6.5 \times 10^7 \frac{T^{5/2}}{n_\mathrm{p}} \left(\frac{20}{\ln \Lambda}\right) \mathrm{cm}^2/\mathrm{s}, \tag{3.47}$$

where n_p is the number density of protons. The expression was derived for hydrogen ionized matter and can be applied for HII regions. For the warm neutral medium the interaction between neutrals leads to the larger viscosity, $\nu_\mathrm{n} \sim u_\mathrm{t} l_\mathrm{nn}$, where u_t is the thermal velocity and l_nn is a mean free path for neutral-neutral collisions. For proton density $n_\mathrm{p} = 1\mathrm{cm}^{-3}$, one finds

$$\nu \simeq 7 \times 10^{21} \mathrm{cm}^2/\mathrm{s}, \tag{3.48}$$

and the Prandtl number

$$\mathrm{Pm} \simeq 10^{14}. \tag{3.49}$$

Using these values, the linear global theory predicts the minimum magnetic field strength to be an extremely small value (Kitchatinov & Rüdiger 2004)

$$B_{\mathrm{min}} \simeq 10^{-25}\mathrm{G}, \tag{3.50}$$

whereas the predicted maximum magnetic field is surprisingly close to the observed strength of galactic fields

$$B_{\mathrm{max}} \simeq 6\ \mu\mathrm{G}. \tag{3.51}$$

The magneto-rotational instability therefore can be assumed to be a very important mechanism of amplification of the magnetic fields up to the observed values in case of galaxies.

Turbulent magnetic diffusivity. As it was already mentioned for galactic dynamos (Section 1.2.1), supernova explosions and superbubbles are the drivers for interstellar turbulence. The magnetic diffusivity due to such turbulence is estimated to be much higher than the molecular one (Ferrière 1992). It might be critical for MRI operating in the galactic disks, especially for very small initial magnetic fields (Kitchatinov & Rüdiger 2004). A limiting condition for the turbulent magnetic diffusivity η_{T} can be easily derived. Let us consider τ as a typical timescale and l as a typical length-scale of turbulence.

$$u_{\mathrm{T}} = l/\tau, \quad \eta_{\mathrm{T}} = l^2/\tau = u_{\mathrm{T}}^2\tau. \tag{3.52}$$

Under the assumption that the time of decay should be at least longer than one rotation one obtains

$$\tau = \frac{l^2}{\eta_{\mathrm{T}}} > \frac{1}{\Omega}, \tag{3.53}$$

$$\eta_{\mathrm{T}} < l^2\Omega. \tag{3.54}$$

The last equation can be reformulated as $\mathrm{Rm} = l^2\Omega/\eta_{\mathrm{T}} > 1$. As length must be taken the typical wavelength λ_z of instability (cell size), which is directly proportional to the Alfvén speed and the rotation frequency. From the measurements of magnetic fields in clusters of galaxies we know that 'on average' the upper limit of the external magnetic field is $10^{-8}\ \ \mu\mathrm{G}$, which corresponds to an Alfvén speed $V_{\mathrm{A}} = 0.1$ kpc/Gyr and $\lambda_z = 30\ \mathrm{pc}$ (assuming $\Omega = 100\ \mathrm{Gyr}^{-1}$). Then the limit for diffusivity will be $\eta_{\mathrm{T}} = 0.1\,\mathrm{kpc}^2/\mathrm{Gyr} \simeq 3 \times 10^{25}\ \mathrm{cm}^2/\mathrm{s}$. For larger magnetic diffusivities the MRI-driven disturbances shall be suppressed. Comparing the number with (3.45) one can see that the molecular diffusivity is too small to stop the magneto-rotational instability.

3.2 MRI for accretion disks: turbulence characteristics

The angular momentum problem is the main question to answer in star and planetary formation research. During the star formation the specific angular momentum is reduced by more than 4 orders of magnitude, although in any non-dissipative system it is precisely conserved. The dissipation due to molecular viscosity has proved to be negligibly small. Therefore, the investigation of the turbulence development in the accretion disks became a subject of very active research. Unfortunately, the turbulence in pure hydrodynamics has to decay very fast. An exception might be the strato-rotational instability, which is proved to exist in Taylor-Couette flow (Shalybkov & Rüdiger 2004). A study of Kepler flow with the uniform gravitational acceleration has been done by Dubrulle et al. (2004). The magneto-rotational instability is linear and probably the most efficient mechanism that is known to produce the required turbulence and viscosity. Strato-rotational and baroclinic instabilities are known to be quite slow, requiring about 10^2 rotations to saturate. The instability with the Hall effect is known to be not faster then magneto-rotational instability. Most MRI studies were done for the case of Keplerian disks. We shall adopt the terminology of data analysis in order to compare comfortably the results of galactic MRI with MRI in Keplerian disks.

An important outcome of all simulations is the magnitude of the horizontal components of the **Reynolds** and **Maxwell stresses**. They are the terms that lead to angular momentum transport in the radial direction, as it can be seen from inspecting the equation for angular momentum conservation in cylindrical coordinates (z, R, ϕ),

$$\frac{\partial}{\partial t}(\rho R^2\Omega) + \nabla\cdot[R(\rho\boldsymbol{u}u_\phi - \boldsymbol{B}B_\phi/4\pi - \nu\rho R\nabla\Omega)] = 0. \tag{3.55}$$

Various fields can be divided into mean and fluctuating parts denoted as $\boldsymbol{u} = \langle\boldsymbol{u}\rangle + \boldsymbol{u}'$. After averaging of the equation we have

$$\frac{\partial}{\partial t}\langle\rho R^2\Omega\rangle + \nabla\cdot[R\langle\rho\boldsymbol{u}u_\phi - \boldsymbol{B}B_\phi/4\pi - \nu\rho R\nabla\Omega\rangle] = 0. \tag{3.56}$$

The term with molecular viscosity ν is very small. Much larger in comparison is the turbulent viscosity ν_{T}, which comes into play by assuming that averaged Reynolds and Maxwell stresses take a form similar to the viscous stress. So, using the Reynolds rules one can replace ν by ν_{T}, i.e.

$$\frac{\partial}{\partial t}\langle\rho R^2\Omega\rangle + \nabla\cdot[R(\langle\rho\boldsymbol{u}\rangle\langle u_\phi\rangle - \langle\boldsymbol{B}\rangle\langle B_\phi\rangle/4\pi - \nu_{\mathrm{T}}\langle\rho\rangle R\nabla\Omega)] = 0, \tag{3.57}$$

where

$$-\nu_{\mathrm{T}}\langle\rho\rangle R\nabla\Omega = \langle(\rho\boldsymbol{u})'u_\phi' - \boldsymbol{B}'B_\phi'/4\pi\rangle = (\tau_{\phi R}, \tau_{\phi\phi}, \tau_{\phi z}). \tag{3.58}$$

In many applications it is assumed that $\nu_{\mathrm{T}} = \frac{1}{3}u_{\mathrm{T}}l$, where u_{T} is the turbulent rms velocity and l is some suitable correlation length. Neither of these two quantities are known, but if it is possible to assume them to be some fraction of the sound speed and vertical scale height, respectively, then

$$\nu_{\mathrm{T}} = \alpha_{\mathrm{SS}} c_{\mathrm{s}} H, \tag{3.59}$$

which is exactly the Shakura & Sunyaev (1973) prescription for eddy viscosity.

The important result for all applications is that α_{SS} is not a constant. It depends on the strength of magnetic fields:

$$\alpha_{\mathrm{SS}} = \tilde{\alpha}_{\mathrm{SS}}^{0} + \tilde{\alpha}_{\mathrm{SS}}^{B} \frac{\langle \boldsymbol{B} \rangle^4}{B_0^4}, \tag{3.60}$$

where one finds $\tilde{\alpha}_{\mathrm{SS}}^{0} \simeq 0.003$ and $\tilde{\alpha}_{\mathrm{SS}}^{B} \simeq 0.33$ (Brandenburg et al. 1995). Then, α_{SS} fluctuates in time, which may cause not fourth but only quadratic dependence on $\boldsymbol{B}$. α_{SS} depends on density stratification and height, shear and vorticity.

$$\alpha_{\mathrm{SS}} \propto \frac{q}{\omega} = \frac{q}{2-q}, \tag{3.61}$$

where q and ω are the shear and vorticity. In this work we find that the galactic rotation introduces a strong radial dependence on the α_{SS} tensor and other turbulent parameters. Correlation tensors (full normalized Reynolds and Maxwell tensors) allow to see the main directions of the turbulence transport

$$\frac{\langle u_i u_j \rangle}{\langle \boldsymbol{u}^2 \rangle}, \qquad \frac{\langle B_i B_j \rangle}{\langle \boldsymbol{B}^2 \rangle}. \tag{3.62}$$

An illustration of the behavior of the stress tensors can be found in Brandenburg et al. (1995).

The accretion rate M can be calculated as

$$\dot{M} = -(2\pi R)(2L_z)\langle \rho u_R \rangle. \tag{3.63}$$

The influence of the rotation on turbulence is reflected by the inverse Rossby number

$$1/\mathrm{Ro} = l_0 \Omega / V_0 = 2\Omega H / \langle \boldsymbol{u}^2 \rangle^{1/2}. \tag{3.64}$$

It is always above 10 for Keplerian disks.

Fourier spectra for kinetic and magnetic total energies allow to observe the length of energy injection λ_{crit} and the transport of energies to larger and smaller scales, as well as the anisotropy of the turbulence.

Calculation of the turbulent diffusivity and α dynamo effects is a more complicated task. Helicity and the alpha-effect can be calculated, using Eq. (1.10), Eq. (1.14) and Eq. (1.15), if the high-conductivity limit or the condition of Eq. (1.17) is fulfilled.

Chapter 4

ZeusMP 3D code and model description

ZeusMP 3D is a numerical code for the simulation of three-dimensional fluid dynamical flows in astrophysics including a self-consistent treatment of the effects of magnetic fields and radiation transfer. The code was developed by Stone & Norman (1992) and was extended from 2D to 3D and further to the parallelized version ZeusMP 3D which has been used in the present work. The algorithms in Zeus 3D divide naturally into three areas: (1) hydrodynamics (HD), (2) magnetohydrodynamics (MHD), and (3) radiation hydrodynamics (RHD). We have used the HD and MHD parts.

The time-explicit, three-dimensional Eulerian hydro-code is based on the method of finite-differences, characterized by a high degree of robustness and speed. The algorithm for evolving the magnetic field are self-contained and independent of the HD algorithms in the early versions, but this is not the case when using HSMoC CT scheme. Using of HSMoC CT scheme (see Stone & Norman 1992 for further details) ensures the exact fulfilling of $\nabla \cdot \boldsymbol{B} = 0$. The scheme uses the Method of Characteristics (MoC, invented by Stone & Norman (1992)) to evaluate the velocity and magnetic field needed to estimate electro-motive forces that are properly up-winded in the characteristic velocities for the set of equations describing transverse Alfvén waves. This is not the full MHD characteristic problem, but a subset which has been found (reference above) to yield good results for the propagation of Alfvén waves. This routine differs from the previous versions in that the Lorentz forces are computed before the electro-motive forces are estimated. Thus, for the electro-motive forces one now uses the velocities which have been updated with all the source terms, including the transverse Lorenz forces.

Neumann-Richtmeyer artificial viscosities are used to capture shocks. The shock capturing viscosity has two parts: the first (quadratic artificial viscosity) is non-vanishing and proportional to $-\nabla \cdot \boldsymbol{u}$ only in regions with $-\nabla \cdot \boldsymbol{u} > 0$, the second part (linear artificial viscosity) is a damping of turbulence with the term

Table 4.1: ZeusMP 3d code performance

Problem size	CPU	Wall Time
$256 \times 256 \times 256$	8	93.7
$512 \times 512 \times 512$	64	94.2
$1024 \times 512 \times 512$	128	103.8
$1024 \times 1024 \times 512$	256	125.1

$\propto c_\mathrm{s}\, q_\mathrm{lin}$ (where $q_\mathrm{lin} < 1$ is a constant). The last term was introduced after realizing that the ZeusMP 3D code has trouble to preserve the stability of low-resolved hydrodynamic disks with only conservative forces acting (see Chapter 3). From the work of Falle (2002) we can learn about shock errors for earlier versions of Zeus, the description may still be valid for present version. It is reported that the Zeus code is showing good accuracy in case of isothermal hydrodynamics. For MHD one has to combine the isothermal equation of state with linear artificial viscosity in order to reach the accurate treating of shocks. Employing linear artificial resistivity will give even better results for removing the rarefaction shocks in MHD waves. For our isothermal models we have used the combination of quadratic and linear artificial viscosities. We do not expect to obtain the shocks for the formulated problem of global MRI. The code is known to be highly diffusive.

It is known that for the case of turbulence under dominant toroidal velocities, the flow is much smoother in the toroidal direction than in the vertical and in the radial direction. Therefore, we can use a nonuniform grid aspect ratio with $\delta z < \delta R < R\delta\phi$. The viscous term is proportional to the $\nu_i \partial_i u_i$ and therefore depends on the mesh width. It is hard to avoid this dependence for cylindrical geometry, where the mesh size (in azimuth) is permanently growing with a distance from the axis.

Speed and efficiency. The large computational PC cluster ‘Sanssouci’ was established at the Astrophysical Institute Potsdam in the fall of 2003. 256 available CPUs have made possible the testing of parallelization efficiency of large-size problems with ZeusMP 3D. 256 available CPUs are divided in four cabinets with fastest connections within the cabinets. The connection between the cabinets is less efficient because of spatial separation. In the Table 4.1 it is shown that the optimal parallelization is achieved with using up to 64 CPUs, which is the full load for one cabinet. With this optimal number of CPUs, a performance summary from the test run with minimum of output is $3.72325 \cdot 10^6$ zone-cycles per CPU second. The code will consume 38 CPU hour for the simulation with $256 \times 512 \times 256$ zones within 15000 cycles (until saturation, which is roughly 1 Gyr).

To make a conclusion from the paragraphs above, we can claim that the ZeusMP code was the best choice for simulating global MRI action in the galactic disks. The speed of calculation allows us to have the simulations with resolution up to 10 pc to be completed within reasonable time with the use of parallelization. It is the only code which includes the parallelization for cylindrical geometry. Known mistakes and inaccuracies of the shock treatment do not disturb the calculations of global MRI, because the driven turbulence is in the subsonic regime.

4.1 Model description

The system of magneto-hydrodynamical equations

$$\frac{D\rho}{Dt} + \rho \nabla \cdot \mathbf{u} = 0, \tag{4.1}$$

$$\rho \frac{D\mathbf{u}}{Dt} = -\nabla P - \rho \nabla \Psi + \frac{1}{4\pi} (\nabla \times \mathbf{B}) \times \mathbf{B}, \tag{4.2}$$

$$\frac{\partial \mathbf{B}}{\partial t} = \nabla \times (\mathbf{u} \times \mathbf{B} - \eta \nabla \times \mathbf{B}) \tag{4.3}$$

are solved with the help of 3D ZeusMP using the uniform grids. The feedback of magnetic fields $\mathbf{B}$ onto velocity fields $\mathbf{u}$ is included as a Lorentz force in the momentum equation. The isothermal relation $P = c_{\mathrm{s}}^2 \rho$ with the sound speed $c_{\mathrm{s}} = 10$ km/s is used for the interstellar medium. Magnetic diffusivity η has a rather small value for the warm gas component of the ISM (see Chapter 1 and 3). For most of the models it is chosen to be equal zero with only numerical diffusivity acting. The models with non-vanishing magnetic diffusivity will be specially notated.

The resolution is chosen to keep from 8 to 11 grid points for resolving the minimal wavelength, its expected initial value was calculated according to Balbus & Hawley (1991). Artificial viscosity is introduced in every model. It dissipates high-frequency numerical noise and smears out shock fronts if the turbulence becomes supersonic.

3D global simulations in the cylindrical coordinates have been done for a disk of thickness $Z = [-1, 1]\,\mathrm{kpc}$ and $R = [1, 5]\,\mathrm{kpc}$. The gravitation potential Ψ is assumed to be generated by the stellar population, self-gravity of the gas is not included. We have prescribed the potential Ψ for radial and vertical directions separately so that similar shapes in stratification and rotation curve profiles result, following Fröhlich & Schultz (1996). No azimuthal variations like density waves and spirals are introduced. All non-axisymmetric structures in density or flow and fields in the simulations are thus due to MRI. The rotation curves are described via the Brandt-type rotation law

$$u_\phi = \frac{R\,\Omega_0}{(1 + (R/R_0)^n)^{1/n}}, \tag{4.4}$$

where R_0 is the radius of transition from rigid to differential rotation, Ω_0 is the angular frequency of rigid galactic ‘core’ rotation, parameter $n = 2$ or $n = 4$. In case of rotation velocity decreasing with radius one should use the Miyamoto-Nagai (1975) gravitational potential (Chapter 2, Eq. (2.5)) and the corresponding rotation curve which is calculated as in case of pressureless disk,

$$u_\phi = \sqrt{R\frac{\partial \Psi}{\partial R}}. \tag{4.5}$$

For models with the density stratification we adopted

$$\rho = \sum_m \rho_{0,m} \exp\left(-\frac{z^2}{H_m^2}\right) + \sum_k \rho_{0,k} \exp\left(-\frac{|z|}{H_k}\right) \quad . \tag{4.6}$$

Lacking knowledge about the vertical stratification of the gas density in the galaxies considered, we adopt the empirical HI distribution of Dickey & Lockmann (1990) for our Galaxy: a combination of two Gaussians with central densities 0.395 and 0.107 cm^{-3} and scale heights of 212 and 530 pc, respectively, and an exponential with central density 0.064 cm^{-3} and a scale height of 403 pc. The runs with constant density are notated respectively.

Resolution. 3D global calculations in the cylindrical coordinates have been done for a disk of thickness $Z = [-1, 1]\ \mathrm{kpc}$, $R = [1, 5]\ \mathrm{kpc}$, $\phi = [0, 2\pi]$. The equations are solved with the 3D ZeusMP code using uniform grids with dimension up to a maximum of $256 \times 1024 \times 256$ for the largest radial extensions. Most runs are done with $256 \times 512 \times 256$. For testing and demonstrations we have used lower resolution, which saved computing time and space. Pseudo-vacuum and periodical conditions were used for the vertical boundaries. Radial boundaries are set to perfect conductor.

Initial conditions. There are different ways to describe a vertical initial magnetic field. A first case is when the initial magnetic fields are chosen to be homogeneous everywhere in the disk, with a non-zero flux through the disk. The vacuum boundary conditions in vertical direction will preserve the flux during the simulation. Next cases are $B_z = b_0 \sin\phi$ or $B_z = b_0 \sin(2\pi R/(R_{\max} - R_{\min}))$ with vanishing flux through the disk, where b_0 is a constant. The initial density profile has to include a function $\hat{\rho}$ to compensate the magnetic pressure

$$-c_{\mathrm{s}}^2 \nabla\hat{\rho} + \frac{1}{4\pi}\nabla B^2 = 0. \tag{4.7}$$

No supernova or superbubbles produced turbulence is taken into account, only some small random density fluctuations of order $10^{-4}\rho_0$ are assumed in the initial condition.

Normalization in Zeus. Zeus works with the following normalization. Time unit is Gyr, scale unit is kpc. Therefore, for velocity we have to use units $[u] = \mathrm{kpc/Gyr} \simeq \mathrm{km/s}$. Magnetic fields are normalized as

$$B_{\mathrm{zeus}} = \frac{B}{\sqrt{4\pi\rho_0}} \equiv \tilde{V}_{\mathrm{A}}, \tag{4.8}$$

where Alfvén velocity and density units are

$$[\tilde{V}_{\mathrm{A}}] = 10^5[\mathrm{cm\,s^{-1}}], \quad [\rho_0] = 10^{-24}[\mathrm{g\,cm^{-3}}]. \tag{4.9}$$

In order to derive from the simulation data the real value of magnetic fields, one has to use the relation

$$B = \sqrt{4\pi\rho_0}\tilde{V}_{\mathrm{A}} = \sqrt{4\pi}\cdot 10^{-1}\mu\mathrm{G}. \tag{4.10}$$

The Alfvén speed can be restored as $B_{\mathrm{zeus}}/\sqrt{\rho_{\mathrm{zeus}}}$, where $\rho_{\mathrm{zeus}} = \rho/\rho_0$. All these relations have been used during data analysis. All the plots and tables in the next chapters contain physical values, free from Zeus normalization.

4.2 Boundary conditions

In the global disk simulations we have more freedom with choosing the boundary conditions. As we have learned during this project, there is a possibility to choose the size of computational domains so large that most of MRI-driven turbulence is placed well inside without much interaction with radial boundaries. The most suitable for our model are two kinds of reflecting boundaries – pseudo-vacuum and perfect conductor conditions. Perfect conductor condition was permanently used for radial boundaries, while for vertical direction we have the choice to use any of the reflective conditions or even a periodical one. Periodical boundary conditions were applied in azimuthal direction, and in some cases for vertical direction.

The following discussion refers to a cylindrical geometry, but it is easy to remove all geometrical R-factors and infer corresponding conditions for Cartesian geometry.

Cylindrical coordinates. We solve the MHD Eqs. (4.1)-(4.3) for isothermal case. In cylindrical coordinates (z, R, ϕ) the equation of motion for velocity components is

$$\rho\frac{Du_z}{Dt} = -\rho\frac{\partial\Psi}{\partial z} - \frac{\partial p}{\partial z} + j_R B_\phi - j_\phi B_R, \tag{4.11}$$

$$\rho\left(\frac{Du_R}{Dt} - \frac{u_\phi^2}{R}\right) = -\rho\frac{\partial\Psi}{\partial R} - \frac{\partial p}{\partial R} + j_\phi B_z - j_z B_\phi, \tag{4.12}$$

$$\rho\left(\frac{Du_\phi}{Dt} + \frac{u_\phi v_R}{R}\right) = -\frac{\rho}{R}\frac{\partial\Psi}{\partial\phi} - \frac{1}{R}\frac{\partial p}{\partial\phi} + j_z B_R - j_R B_z \tag{4.13}$$

where $\boldsymbol{j} = (1/4\pi)\nabla \times \boldsymbol{B}$ is a current. The Maxwell equation (Appendix 2) with the dissipative term takes the form

$$\frac{\partial B_z}{\partial t} = -\frac{1}{R}\left(\frac{\partial}{\partial R}(RE_\phi) - \frac{\partial E_R}{\partial \phi}\right), \tag{4.14}$$

$$\frac{\partial B_R}{\partial t} = -\left(\frac{1}{R}\frac{\partial E_z}{\partial \phi} - \frac{\partial E_\phi}{\partial z}\right), \tag{4.15}$$

$$\frac{\partial B_\phi}{\partial t} = -\left(\frac{\partial E_R}{\partial z} - \frac{\partial E_z}{\partial R}\right), \tag{4.16}$$

where

$$-E_z = u_R B_\phi - u_\phi B_R + \alpha B_z - \eta\frac{1}{R}\left(\frac{\partial}{\partial R}(RB_\phi) - \frac{\partial B_R}{\partial \phi}\right), \tag{4.17}$$

$$-E_R = u_\phi B_z - u_z B_\phi + \alpha B_R - \eta\left(\frac{1}{R}\frac{\partial B_z}{\partial \phi} - \frac{\partial B_\phi}{\partial z}\right), \tag{4.18}$$

$$-E_\phi = u_z B_R - u_R B_z + \alpha B_\phi - \eta\left(\frac{\partial B_R}{\partial z} - \frac{\partial B_z}{\partial R}\right). \tag{4.19}$$

Terms with α-effect and magnetic diffusion η were included in Zeus during the project.

In the Zeus code the boundary conditions are applied to electric fields instead of magnetic fields. Conditions for velocities are the same both for perfect conductor and for pseudo-vacuum; they can be simply reduced to the reflection. Our cylindrical domain is restricted with $R = R_{\mathrm{in}}$, $R = R_{\mathrm{out}}$ in radial direction and with $|z| = Z_{\mathrm{out}}$ in vertical direction. For radial boundaries (both perfect conductor or pseudo-vacuum) one has

$$\frac{\partial \rho}{\partial R} = 0, \quad \frac{\partial u_z}{\partial R} = \frac{\partial u_\phi}{\partial R} = u_R = 0. \tag{4.20}$$

The same rules are valid for vertical boundaries,

$$\frac{\partial \rho}{\partial z} = 0, \quad \frac{\partial u_R}{\partial z} = \frac{\partial u_\phi}{\partial z} = u_z = 0. \tag{4.21}$$

The idea of conserving the magnetic flux is applied to the boundary conditions of magnetic fields. The Pointing vector $\boldsymbol{E} \times \boldsymbol{B}$ has to vanish on the chosen surface. For example, on the surface $z = Z_{\mathrm{out}}$ it leads to $\boldsymbol{E} \times \boldsymbol{B}|_z = B_R E_\phi - B_\phi E_R = 0$. The last condition can be fulfilled in two ways, they are called the perfect conductor and the pseudo-vacuum boundary conditions.

4.2.1 Perfect conductor

The perfect conductor boundary can be imagined as a conducting metal plate. That means that the tangential component of the electric field and the normal component of the magnetic field are required to vanish at the borders. We have used the perfect conductor boundary condition mostly for radial boundary conditions, for $R = R_{\rm in}$, $R = R_{\rm out}$.

$$\mathcal{E}_z = 0, \quad \mathcal{E}_\phi = 0, \quad \frac{\partial \mathcal{E}_R}{\partial R} = 0 \ \ \text{at} \ \ R = R_{\rm in}, \ R_{\rm out}. \tag{4.22}$$

From Eqs. (4.11)–(4.19) one can see that the boundary conditions for velocities and for electric field lead us to the boundary conditions for magnetic fields. In the simplest case, without magnetic diffusivity and alpha-effect, we have the following radial condition for B:

$$B_R = 0, \quad \frac{\partial B_z}{\partial R} = 0, \quad \frac{\partial B_\phi}{\partial R} = 0 \ \ \text{at} \ \ R = R_{\rm in}, \ R_{\rm out}. \tag{4.23}$$

4.2.2 Pseudo-vacuum

Pseudo-vacuum boundary condition imply the reflection rules for the velocity fields. As there are no currents in vacuum, we may write the condition

$$\nabla \times \boldsymbol{B} = 0. \tag{4.24}$$

The electric fields are reflected mirror-like,

$$\mathcal{E}_z = 0, \quad \frac{\partial \mathcal{E}_R}{\partial z} = 0, \quad \frac{\partial \mathcal{E}_\phi}{\partial z} = 0 \ \ \text{at} \ \ |z| = Z_{\rm out}. \tag{4.25}$$

For the magnetic field we have from Eqs. (4.11)–(4.11)

$$B_R = 0, \quad B_\phi = 0, \quad \frac{\partial B_z}{\partial z} = 0 \ \ \text{at} \ \ |z| = Z_{\rm out}. \tag{4.26}$$

The difference to the previous condition is that a normal component of the magnetic fields is allowed outside of the domain.

The boundary conditions for the non-vanishing alpha-effect are well described in Elstner et. al (1990).

4.3 HD and MHD tests

Before starting the calculations with MRI acting in galactic gaseous disks (Chapter 5), we have done some tests.

In Table 4.2, the notation ‘stable’ means that no magnetic field amplification or flow deviations were obtained. The very first run n1 is one of the hydrodynamical stability tests for the Brandt-type rotation law (Eq. (4.4)). We found that the

Table 4.2: Test models for vertical initial magnetic field

run	$V_{\mathrm{A},0}[\mathrm{km/s}]$	R_0 [kpc]	$\Omega_0[\mathrm{Gyr}^{-1}]$	orbits	
n1	0.0	2.0	100	27	stable
n2	0.9	–	40	80	stable
n3	0.3	100	30	30	stable
b1	11	2.0	100	33	NOT st.
b2	15	2.0	100	30	NOT st.
b3	20	2.0	100	26	stable
b4	36	2.0	100	17	stable
b5	75	2.0	100	35	stable

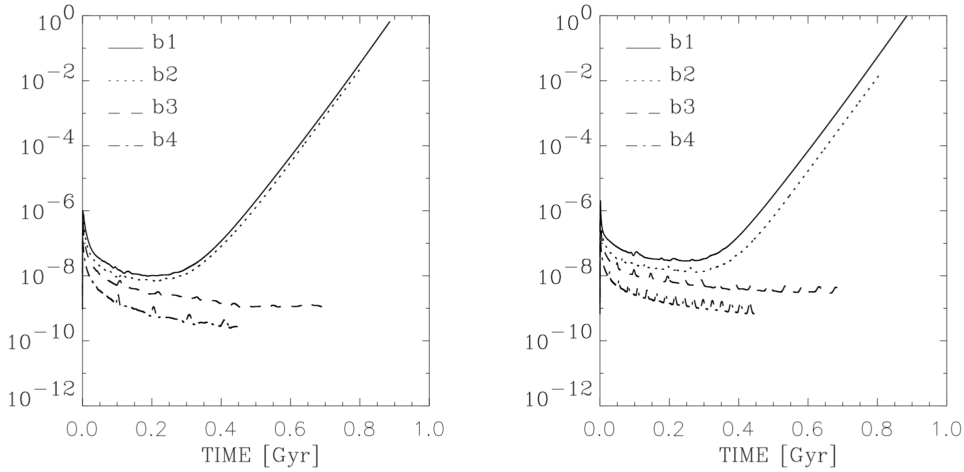

Figure 4.1: The energies of the radial magnetic field component (left) and the azimuthal magnetic field component (right) for different strengths of initial magnetic fields (Table 4.2)

necessary setup for the disk stability both with and without density stratification is reached if the radial resolution is not less than 60 mesh points for radial extension from 1 kpc to 5 kpc.

Models n2 and n3 are the rigid rotation tests for homogeneous initial magnetic fields. Model n2 has the strict rigid rotation law $u_\phi = \Omega_0 R$, whereas model n3 has the Brandt-type rotation law with the rigid part extended to 100 kpc. The initial velocity and density perturbations (Section 5.1.2) have to be set to values not larger than 10^{-4}. MRI is known to exist only with non-zero shear (Section 3.1), so with these runs we made sure there will be no other effects except MRI in our models.

The simulations b1 – b5 in Table 4.2 were done using the Brandt-type rotation law (Eq. (4.4)) with rather large initial homogeneous magnetic fields. No density stratification is assumed. The box size in kpc is $[z : R : \phi] = [(-0.5, 0.5) : (1, 5) : (0, 2\pi)]$ with the resolution of $[128 : 256 : 128]$ mesh points. Numbers of orbits are calculated for the outer radius of the disk. Instability stops to work when the magnetic tension is dominating the centrifugal force for the loops. This happens for an initial field of 7 μG ($V_\mathrm{A} = 20\ \mathrm{km/s}$, with density $10^{-24}\ \mathrm{g/cm^3}$). Four models with large Alfvén velocities are plotted on Fig. 4.1. They show no differences with the theoretical restriction in Eq. (3.31),

$$\frac{\lambda_\mathrm{crit}}{2H}|_\mathrm{b2} \simeq 0.6, \quad \frac{\lambda_\mathrm{crit}}{2H}|_\mathrm{b3} \simeq 1. \tag{4.27}$$

from where model b2 is expected to be unstable while the wavelength is still fitting in the computational domain. From Eq. (4.27) follows, the initial vertical magnetic field must not be stronger than 7μG for given density.

Meinel model test. In order to test the accuracy of MHD calculations with magnetic diffusivity implemented in Zeus (Eqs. (4.11)–(4.11)) we have used the Meinel-model. The α-tensor was implemented in s simplified way and used only for testing.

An exactly solvable global α^2-dynamo model for the disk (Meinel 1990) is an excellent accuracy test. We assume a cylinder (axis inclusive) with $R \le R_\mathrm{out}$, $-H \le z \le H$. The magnetic diffusivity η is fixed to be constant, whereas the α-tensor looks like

$$\alpha_{zz} = \alpha_{rr} = \alpha_{\phi\phi} = \alpha, \tag{4.28}$$

$$\alpha = \begin{cases} \alpha_0, & 0 < z \le H,\ r \le R \\ -\alpha_0, & -H \le z < 0,\ r \le R \end{cases}.$$

Scalars T and S define toroidal and poloidal parts of the magnetic field as

$$\boldsymbol{B} = \boldsymbol{e}_z \times \nabla T + \nabla \times (\boldsymbol{e}_z \times \nabla S). \tag{4.29}$$

The solution of the induction equation for the perfect conductor boundaries is

$$T = \frac{\alpha_0}{\eta} S, \quad S_{n,l} = \sin\left(n\pi \frac{z}{H}\right) J_0\left(y_l^0 \frac{r}{R}\right), \quad n = 1, 2, 3, ...; \quad l = 1, 2, 3, ..., \tag{4.30}$$

where y_l^0 is a first node for the Bessel function J_0 . Critical number is

$$\left(\frac{\alpha_0}{\eta}\right)_{n,l} \geq \left(\left[\frac{n\pi}{H}\right]^2 + \left[\frac{y_l^0}{R}\right]^2\right)^{1/2} . \tag{4.31}$$

Thus, for $n = 1$and $l = 1$, the first critical number can be easily calculated to be

$$\left(\frac{\alpha_0}{\eta}\right)_{1,1} = 4.95495, \tag{4.32}$$

where for $H = 1$ and $R = 1$ the largest mode is with $y_1^0 = 3.8317$.

The accuracy of ZeusMP with implemented terms of α-effect and magnetic diffusivity can be checked with the help of last equations. We have used a quenching function for the α-tensor, $\alpha \sim (1 + E_{\rm mag}/E_{\rm eq})^{-1}$. Calculations were started with the parameter (α_0/η) being over-critical. The magnetic energy is growing due to the α-effect and leads to a reduction of the alpha tensor via quenching until the critical number is reached. At this moment the dynamo is saturated. The new value of alpha can be measured. Our numerical result for resolution (21 : 17 : 5) is $(\alpha_0/\eta)_{1,1} = 5.01179$, for resolution (21 : 17 : 16) we have $(\alpha_0/\eta)_{1,1} = 5.01178$.

As a conclusion of this chapter we may claim that the ZeusMP simulations of HD gaseous disk are stable and reliable. The MHD disk is stable in the case of a homogeneous magnetic field and rigid rotation.

Chapter 5

3D global simulations of MRI for galaxies

5.1 MRI with purely vertical initial magnetic fields

Our MRI simulations have various initial and boundary conditions. The set of these conditions was chosen to assure a stable development for the instability. We split the whole lot of runs in groups. Each group of runs will be analyzed for its positive and negative aspects.

The first group contains the models with homogeneous density. The models have the fixed disk thickness, they allow us to check a correspondence of the typical wavelength to the strength of initial vertical magnetic field. Unfortunately, with reflecting vertical boundary conditions the saturation cannot be reached within a reasonable calculation time. The subgroup of runs with periodical vertical boundaries is saturating. The influence of boundary conditions on the average turbulent parameters will be demonstrated.

The models in the second group have a vertical density stratification included. Here we can see the effect of the density stratification when comparing with the results of the first group. Again, there are some slight differences between subgroups with reflecting and those with periodical vertical boundaries. Fixing the strength of the initial magnetic field and the density stratification, we have varied the rotation curves. Saturated turbulence could not be reached for disk half-thickness of 1 kpc because of too strong a density decrease. For thin disks (0.5 kpc and less) the saturated state can be reached with the periodic vertical boundaries.

The third group contains the models with a sinusoidal initial field, which was widely used for box simulations as a saturating field configuration. Still, the same problem as with the thick disks – no saturation there.

All the models lead to the a common turbulent picture. We may claim that the MRI process is not strongly affected by numerics.

Table 5.1: Models with homogeneous density ($\rho_0 = 0.47 \cdot 10^{-24}$ g/cm^3)

run	B_z [μG]	$V_{\rm A,0}$ [km/s]	λ_z [pc]	$u_{\rm T}$ [km/s]	$B_{\rm T}$ [μG]	$V_{\rm A,T}$ [km/s]	$B_{\rm sat}$ [μG]
hd1	0.11	0.45	130	2.3	1.0	4.1	4
hd2	0.22	0.9	220	4.5	2.8	12	10
$\rm hd2_r$	0.22	0.9	220	8.3	2.3	9.4	-
hd3	0.44	1.8	400	5.8	4.1	20	15
$\rm hd3_r$	0.44	1.8	400	17	4.3	17.6	-
hd4	0.66	2.7	616	22	4.7	19.3	-

5.1.1 Uniform density

In Table 5.1 the runs with identical rotation curves ($\Omega_0 = 100{\rm Gyr}^{-1}$, $R_0 = 2$ kpc, $n = 2$ in Eq. (4.4)), but for different magnetic field amplitudes are presented. The initial magnetic field is purely vertical and homogeneous everywhere in the disk. For the initial magnetic field component B_z the corresponding Alfvén velocity is $V_{\rm A,0} = B_z/\sqrt{4\pi\rho}$. The following columns in the Table 5.1 are the critical wavelength λ_z obtained from simulations, the velocity dispersion $u_{\rm T} = \langle \boldsymbol{u}'^2\rangle^{1/2}$, the amplitude of the turbulent magnetic fields $B_{\rm T} = \langle \boldsymbol{B}'^2\rangle^{1/2}$, the Alfvén velocity dispersion $V_{\rm A,T} = \langle \boldsymbol{V}'^2_{\rm A}\rangle^{1/2}$ and the amplitude of saturated magnetic fields $B_{\rm sat}$. The resolution is $[120 : 105 : 72]$ for the disk with half-thickness $H = 0.8$ kpc and radii from 1 kpc to 4.5 kpc. The perfect conductor boundary condition in radial direction was used for all models. Uniform density allows to use periodical boundary conditions in vertical direction. Models $\rm hd2_r$ and $\rm hd3_r$ are identical to hd2 and hd3 but with reflective (pseudo-vacuum) vertical boundaries.

The common characteristics of the models with both pseudo-vacuum and periodic vertical boundary conditions are the following. One finds that the typical wavelength λ_z grows linearly with the initial magnetic field. This is a well known result of the linear theory (Velikhov 1959; Fricke 1969; Balbus & Hawley 1991). Another two runs with initial Alfvén velocities $V_{\rm A} = 1.8$ km/s and $V_{\rm A} = 2.7$ km/s were done in addition, to confirm the linear theory prediction. From Table 5.1 one can estimate that the wavelength λ_z is $\lesssim 10^{-3}$pc for seed fields of 10^{-12}G. We find that the wavelength should increase with the increasing of magnetic fields during the simulation, transporting the energy from critical to larger scales.

The critical scales for instability are clearly visible in all dimensions in the magnetic energy E spectra, but in particular in the vertical $E_z(\lambda_z)$ component. In Fig. 5.1 the Fourier spectra show the critical wavelengths for the turbulent magnetic energy E for the hd1 model from Table 5.1. The wavelength is normalized to the computational domain size (L_z, L_R, L_ϕ). The slope of the magnetic energy spectrum is much steeper than a Kolmogorov spectrum, especially in the early non-saturated stages due to the peak of fastest unstable mode growth (Fig. 5.1 (a)). In the linear regime the peaks would be delta-functions. The magnetic spectra are broadening with time while the MRI is developing large scale fields (Fig. 5.1 (b)). The energy is transported from small to large scales, which may also be an indication for the alpha-effect. The magnetic Fourier spectra on Fig. 5.1 (b) show the

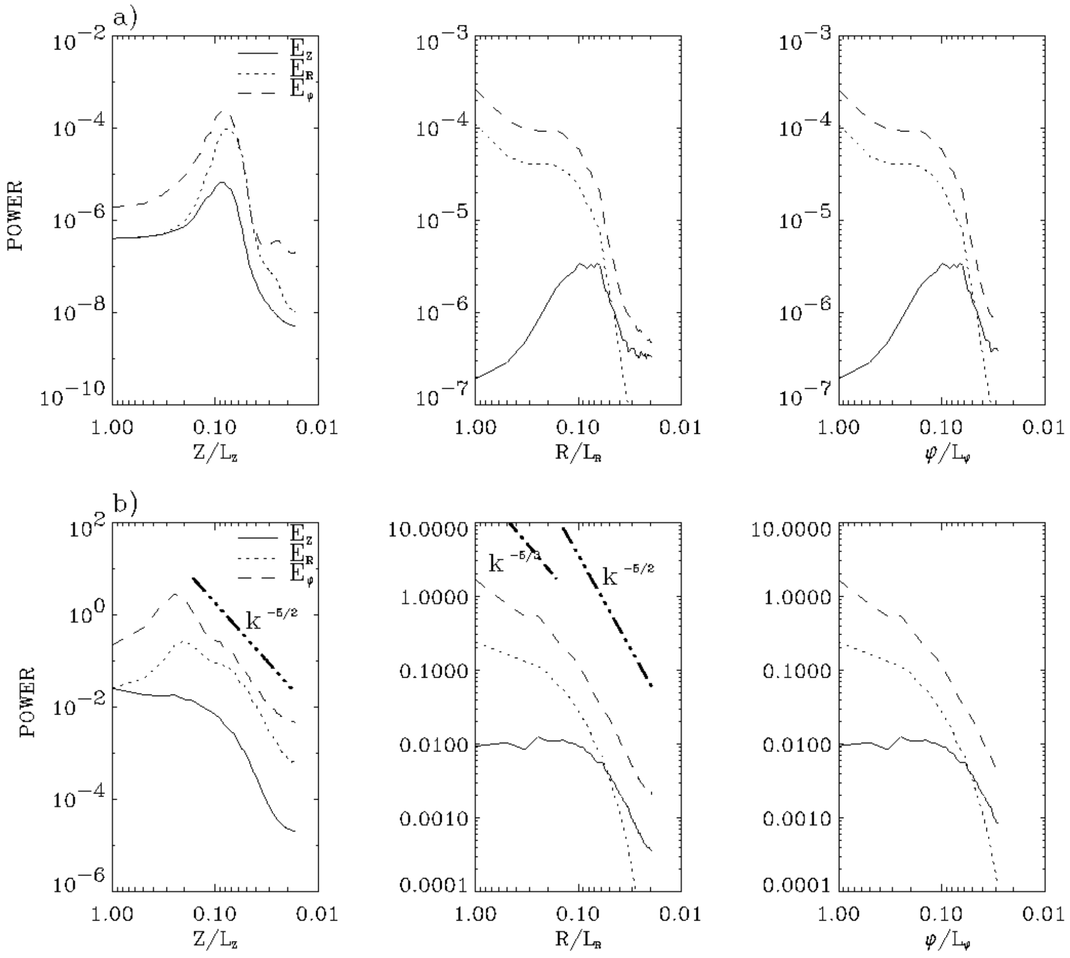

Figure 5.1: Time dependent turbulent 1D magnetic energy spectra $E(\lambda)$ for the model $\mathrm{hd1}$ (no density stratification, $B_0 = 0.11\ \mu$G). Time is $0.8\mathrm{Gyr}$ for case a), and $1.3\mathrm{Gyr}$ for case b)

slope $k^{-5/2}$ both along and perpendicular to the magnetic field direction. Drecker et al. (2000) find a 5/3-law for the kinetic spectrum for the azimuthal wave numbers, but a steeper 5/2-law for the magnetic spectrum with a global MRI-simulation

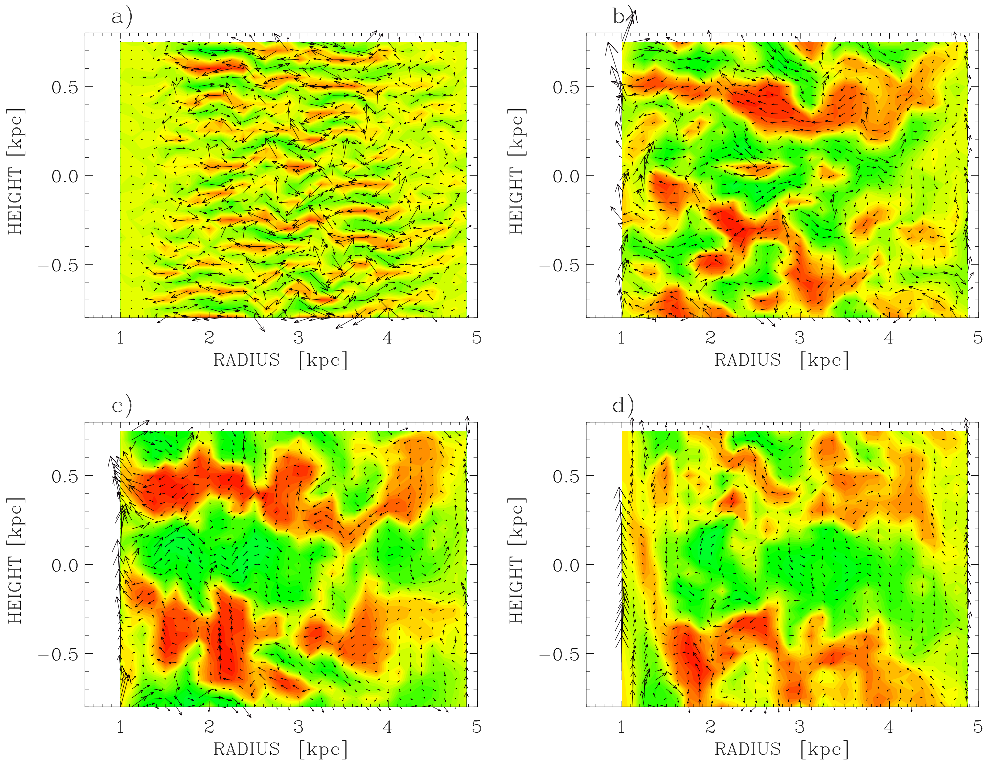

Figure 5.2: The time evolution of the ‘thin sheets’ turbulent structures driven by MRI, model $\mathrm{hd2}$. (B_R, B_z) are plotted with arrows. The change of B_ϕ sign is shown with red-green color contours. Case a) corresponds to the time $1.1\mathrm{Gyr}$, case b) to $1.6\mathrm{Gyr}$, case c) to $2.0\mathrm{Gyr}$, case d) to $3.0\mathrm{Gyr}$

in a sphere. Haugen et al. (2003) find magnetic spectra between $k^{-5/3}$ and $k^{-3/2}$ for forced-turbulence without helicity. It is not clear whether the steepness of the spectra in Fig. 5.1 is an intrinsic feature or only an indication for the restricted nonlinearity of our simulation. From magnetic field observation (Beck 1999) it is known that the synchrotron emission energy has a slope of $k^{-5/2}$ (see Section 1.1). Cosmic rays are tracers of magnetic fields but they do not tell us whether these magnetic fields have an energy spectrum slope $k^{-5/2}$ too.

During MRI operating in the disk the generated azimuthal component of the field might become unstable as well. The resulting toroidal magnetic field is anyway not purely axisymmetrical, although the m=0 is clearly dominant in the energy spectra. Comparing the energies of different field components in Fig. 5.1 we derive the following relation for amplitudes: $\delta B_z \ll \delta B_R < \delta B_\phi$.

Fig. 5.2 shows the time slices of MRI action in the disk in edge-on view. Arrows are used for the directions of (B_R, B_z) vectors. Time after 1 Gyr corresponds to the saturation process of MRI in the model hd2. Magnetic energy growth and saturation is plotted in Fig. 5.3 for all models. One can see from Fig. 5.2, that

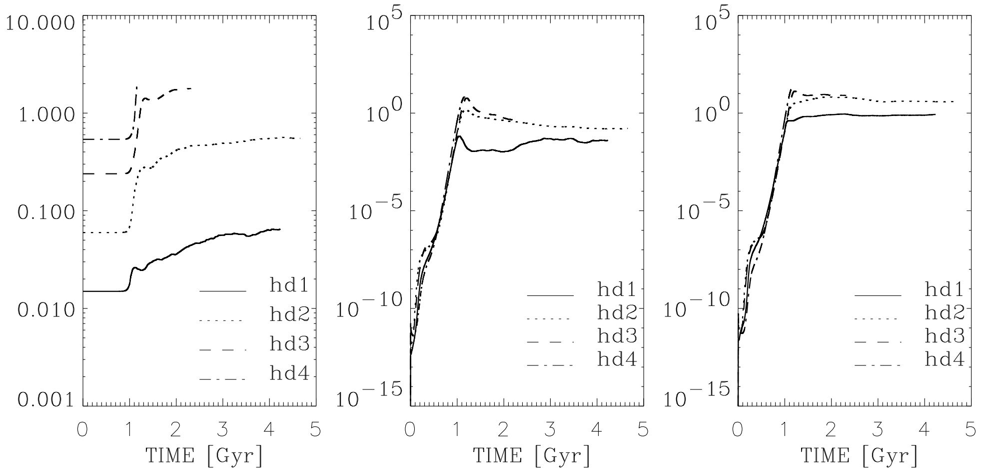

Figure 5.3: Magnetic energy densities of vertical (left), radial (middle) and azimuthal (right) field components

during the MRI action the turbulence has a thin-sheet structure with the $k^{-5/2}$ energy spectrum slope. During the saturation process the magnetic fields become large-scale and seemingly quadrupolar.

The horizontal velocity $u_{\rm T} = (\langle u_R'^2\rangle + \langle u_\phi'^2\rangle)^{1/2}$ grows with the initial magnetic field (Table 5.1). For the given examples it reaches the values of a few km/s while the small-scale magnetic fluctuation $B_{\rm T} = (\langle B_R'^2\rangle + \langle B_\phi'^2\rangle)^{1/2}$ is of the order of a few μG. Its Alfvén velocity exceeds the Alfvén velocity of the external field by a factor of 10 but its value is comparable to $u_{\rm T}$. Approximate equipartition $V_{\rm A,T} \simeq u_{\rm T}$ results for models with relatively small initial magnetic flux (hd1). Models with larger fluxes develop the turbulent Alfvén velocities which are $3-4$ times larger compared to $u_{\rm T}$. The velocity dispersion $u_{\rm T}$ does not depend on vertical direction z. In the next subsection we see that the density stratification is important for the vertical distribution of velocity dispersion.

The magnetic energy curves are identical for different boundary conditions. In Fig. 5.3 the curves of magnetic energy are plotted. Energies were calculated as normalized integral of the squared magnetic field (in μG) over the volume, $E_{\rm mag} = V^{-1}\int dV B^2 \sim 10^{-12}{\rm G}^2$. The radial and azimuthal fields components are amplified within the first Gyr. The amplification of the vertical magnetic field component becomes visible when the generated turbulence has developed an amplitude δB_z larger than initial vertical field.

The upper limit for initial magnetic fields for MRI will be the value where the corresponding wavelength of instability will exceed the disk thickness (Eq. (3.31) and tests in Chapter 4). For given model parameters, the upper limit should be 15 μG. The simulations lead to an upper limit of the magnetic field amplitude of 4 μG, 10μG and 15 μG the disk thickness of $H = 0.8\,{\rm kpc}$. As one can see from Table 5.1, the magnetic field amplitude in the saturation regime does depend not only on the disk thickness but also on the value of the initial ‘seed’ field. A similar effect was observed for the α-dynamo operation, where the resulting magnetic fields depend on the closeness of a system to the marginal stability. If one starts the turbulence close to the marginally stable state, the nonlinear effects are weak. Turbulence far from stability have stronger nonlinearity. Large and weak nonlinearities can cause some differences in saturated regime of turbulence.

Four models (hd1, hd2, hd3, hd4) were done for periodical boundary conditions with the vertical direction. In these runs saturation has been reached, except for the model with the largest magnetic flux (hd4). This is probably due to the fact that the critical wavelength in the model hd4 is comparable to the disk half-thickness, which leads to numerical difficulties in time stepping. The time step shortens by a factor 10^2 or even 10^3 because the turbulence with high or supersonic Alfvén velocities is fully developed. The models $\mathrm{hd2_r}$ and $hd3_r$ with pseudo-vacuum vertical boundary conditions have a similar time-development. These simulations did not reach saturation because of the shortening of the time-step. The code did not crash, but we had to terminate the calculations when they became too time consuming. A way out consist in changing the type of vertical boundary conditions to periodic, which results in slight differences in the turbulence and allows the models to saturate.

Critical wavelength and resolution. What will happen if the resolution is not good enough to resolve the fastest-growing MRI waves? We have observed, that the lack of resolution slows down the growth rate. The reason is that the larger wavelengths are growing slower, while the small and fast scales were cut away by poor resolution. In order to obtain the correct results of the turbulent parameters and the growth rates, we have pre-estimated the critical wavelengths to ensure the requested resolution.

5.1.2 Nonuniform density

The model can be improved by adopting the density stratification. We have used the density profile described in the previous chapter with Eq. (4.6) (Dickey & Lockmann 1990). The maximum density is $\rho_0 = 10^{-24}$ g/cm^3 in the galactic midplane. The improved models are collected in Table 5.2. The variations of the Brandt-type rotation curve parameters R_0, Ω_0 and n (see Eq. (4.4)) are given in the first columns. The initial magnetic field is purely vertical and homogeneous everywhere in the disk. For the initial magnetic field B_z the corresponding Alfvén velocity is $V_{\mathrm{A,0}} = B/\sqrt{4\pi\rho(z)}$ at the galactic midplane. The following columns are the same as in the Table 5.1, the velocity dispersion u_{T}, the amplitude of the turbulent magnetic fields B_{T}, the Alfvén velocity dispersion $V_{\mathrm{A,T}}$. The resolution is $[256 : 512 : 256]$ for the disk with half-thickness $H = 1\,\mathrm{kpc}$ and radii from $1\,\mathrm{kpc}$ to $5\,\mathrm{kpc}$. An exception is the model U4, for it has extended radii from $1\,\mathrm{kpc}$ to $11\,\mathrm{kpc}$ with $[256 : 1024 : 256]$ mesh points of resolution. The perfect

Table 5.2: Density-stratified models with different rotation laws

model	R_0 [kpc]	Ω_0 [Gyr^{-1}]	n	B_z [μG]	u_T [km/s]	B_T [μG]	$V_\mathrm{A,T}$ [km/s]
m1	2.3	75	2	0.11	2.7	0.4	9
m2	2.3	75	2	0.32	5.8	1.4	24
m3	2.0	100	2	0.32	7.8	2.0	43
U1	2.00	76	2	0.32	5.8	1.4	24
U2	1.00	152	2	0.32	4.2	0.9	19
U3	1.52	100	4	0.32	6.7	1.2	34
U4	2.80	53	4	0.32	4.3	1.5	15
F1	1.50	160	4	0.11	2.6	0.4	8

Table 5.3: Rotation time $2\pi/\Omega_0$ is given for most models of Table 5.2. The simulations gave a global e-folding time of magnetic field, τ_g, the ratio of magnetic to kinetic energy, and the ratio of Maxwell to Reynolds stresses

model	$2\pi/\Omega_0$ [Myr]	τ_g [Myr]	$E_\mathrm{mag}/E_\mathrm{kin}$	MS/RS
m1	83	86	4.7	15
m2	83	86	3.8	120
m3	63	60	3.5	452
U1	82	81	3.6	240
U2	41	44	4.6	305
U3	63	46	3.0	256
U4	119	96	2.9	-

conductor boundary condition in radial direction was used for all models, with reflective (pseudo-vacuum) vertical boundaries.

Parameters R_0, Ω_0 and n were varied. Results of the models with $n = 2$ can be compared with the linear global model of Kitchatinov & Rüdiger (2004). Model $\mathrm{m1}$ works with a weak magnetic field which is increased in the models m2 and m3. Models m2 and m3 differ by the rotation laws. Models U[1-4] are made to fit the rotation curve of NGC 1058, the galaxy with an extended HII disk and a badly defined rotation law (Chapter 1). Models U4 and U1 are the best fits (Fig. 5.4). Still, keeping in mind a possible warping of the disk, we calculated the rotation curves with the different behavior of the shear inside the radius $R = 7$ kpc. For for the galaxies shear is a function of radius. Model F1 is made to fit the rotation curve of the flocculent NGC 4414 (Table 2.1), an example of a fast rotating galaxy with large shear. In Fig. 5.4 we plot the observation data of the rotation of the NGC 4414 (Braine 1993) and its fitting with Eq. (2.5) with only disk ($a_{\rm disk} = 2.0$ kpc, $b_{\rm disk} = 0.1$ kpc, $M_{\rm disk} = 7 \cdot 10^{10}$ $\mathrm{M}_{\odot}$) and the small halo ($a_{\rm halo} = 12.0$ kpc, $b_{\rm halo} = 12.0$ kpc, $M_{\rm halo} = 10^{10}$ $\mathrm{M}_{\odot}$).

Topology and global symmetries. The MRI-driven turbulence appears to have a sheets-like structure in edge-on disks (Fig. 5.5). The vertical length of the turbulent cells is smaller by an order of magnitude compared to the radial one. Both length-scales vary during the simulations. The cells evolve from small to large structures. The influence of the density stratification is visible both in initial and final stages: the smallest scales belong to the region of maximal density at the equatorial plane $z = 0\,\mathrm{kpc}$ and they are most visible at earlier times, whereas at the last stage of MRI development the turbulence is present at all heights with slight differences in cell thickness. The sheets are lying parallel to the disk plane almost without mixing vertically. Comparing the edge-on plots for models U2 and U3, one can point out the transition radius R_0 for every model because the instability starts to operate at $R \simeq R_0$. The steepness of rotation curves, or the change from $n = 2$ (model U2) to $n = 4$ (model U3) affects the radial extend of the turbulence. Fig. 5.6 shows the magnetic vectors and the color contour of density fluctuations. The face-on slide is taken as an equatorial cut of the simulated gaseous galactic disk. Fluctuations of density in radial direction are not great, its maximum is up to 50% from the initial value. No radial or azimuthal dependence of the density was prescribed. As one can see, the instability works only in the region of $R > R_0$, i.e. in the region of non-zero shear. Inside the ring with the radius $R < 2\,\mathrm{kpc}$ no radial or azimuthal magnetic fields components are generated. Dark-green regions are the minima of density. Maxima of magnetic fields are mostly correlated with dark-green regions. The plot was made after a local averaging procedure. One can see close-spiral or almost ring structures created by MRI, because the cells of instability were stretched along the azimuth due to rotations.

We have shown in Chapter 1 that the quadrupolar symmetry of the global mag-

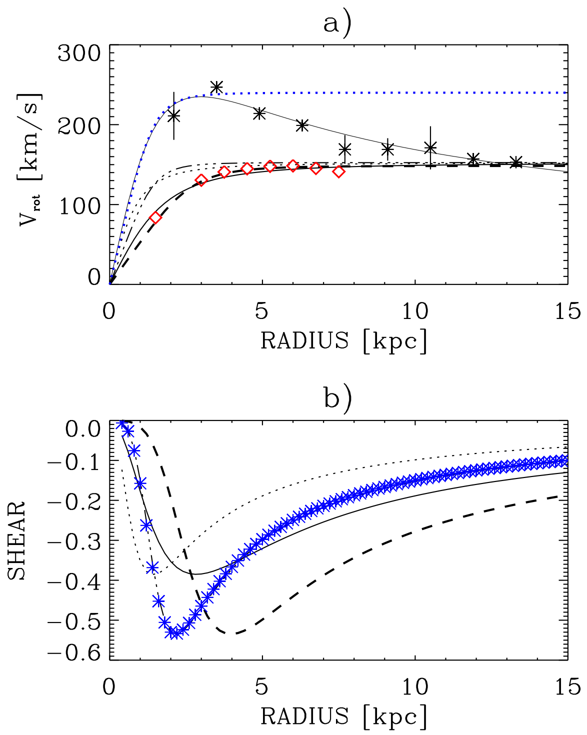

Figure 5.4: The rotation curves (a) and derived shears $\Omega_0^{-1}\partial\Omega/\partial\ln R$ (b) are given for models from Table 5.2. Models U1, U2, U3 and U4 are fits for NGC 1058 case. Solid lines are for velocity and shear in model U1, dotted lines are for model U2 and dash-dotted lines are for model U3, thick dashed lines are for U4. Rhombs shows the NGC 1058 rotation curve for inclination $\sin i = 0.1$ (Dickey et al. 1990). The NGC 4414 (model F1) rotation curve (blue dots) and derived shear (blue stars) are plotted using Eq. (4.4). Stars with error bars show HII data for NGC 4414 (Braine 1993), it is fitted with Eq. (2.5) (solid line)

netic fields needs to be explained by dynamo or MRI. The parity $\mathcal{P}$ is defined with

$$\mathcal{P} = \frac{E^{\mathrm{Q}} - E^{\mathrm{D}}}{E^{\mathrm{D}} + E^{\mathrm{Q}}} \tag{5.1}$$

where E^{D} and E^{Q} are the energies of the modes with dipole and quadrupole symmetry. The value of parity (5.1) is -1 for a strict dipolar field structure and it is $+1$ for quadrupole. The linear global model of Kitchatinov & Rüdiger (2004) predicts the quadrupolar magnetic fields to result due to MRI. Comparison of stability diagrams for the dipole and quadrupole modes shows that the quadrupolar solution has somehow wider branches. It means that this symmetry can be easier excited for smaller minimum magnetic fields, and it needs larger maximum fields for instability termination. Still, the stability diagrams show the large parameter space of co-existing dipole and quadrupole modes, so one could not exclude the

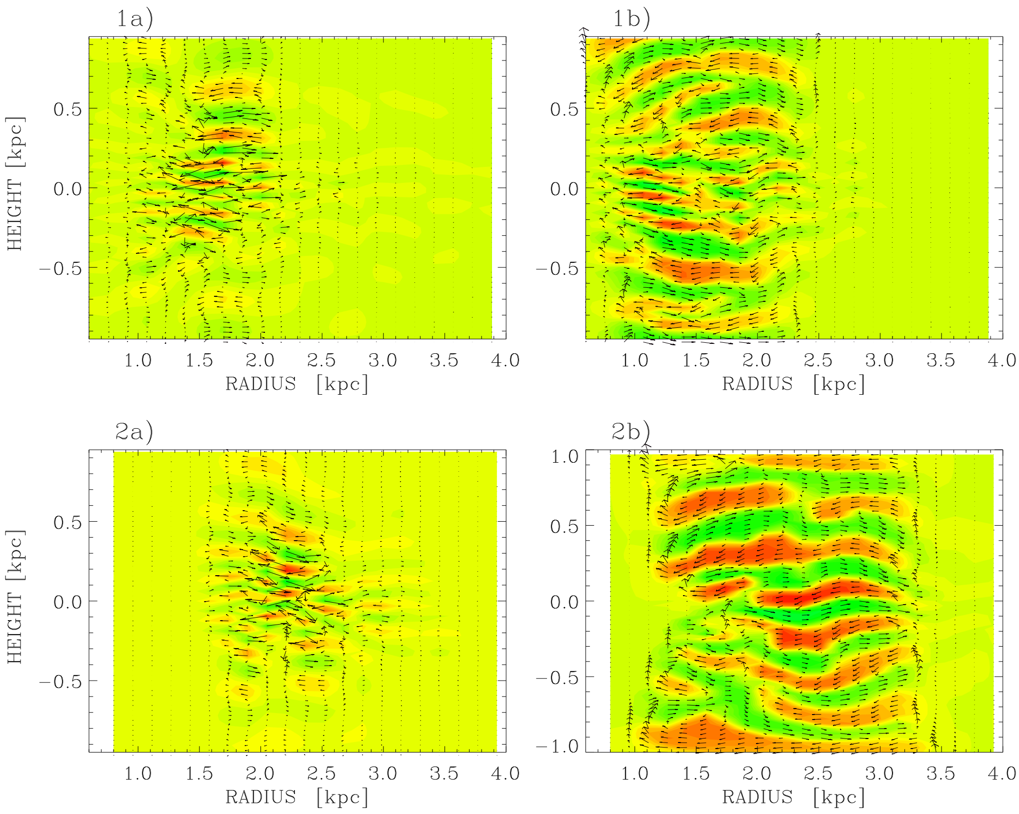

Figure 5.5: Plots 1a) and 1b) represent the model U2 for time slices $t = 0.5\mathrm{Gyr}$ and $t = 0.7\mathrm{Gyr}$. Plots 2a) and 2b) represent the model U3 for time slices $t = 0.6\mathrm{Gyr}$ and $t = 0.9\mathrm{Gyr}$. The minima and maxima of the B_ϕ components are shown in green and red colors, yellow is a mark of vanishing B_ϕ component. Over-plotted arrows show radial and vertical components of the magnetic field for same time slices

mixed parity to appear in nonlinear regime. Fig. 5.7 gives the results of our global non-linear simulations for the symmetry of the MRI-amplified magnetic field. As the initial field B_0 is antisymmetric with respect to the midplane the magnetic field parity starts in all cases with a strong dipolar part but it approaches zero after a few rotations. Indeed, we demonstrate that the final solution is a mixed mode, i.e. the magneto-rotational instability can produce the quadrupolar magnetic fields from the purely vertical seed field.

Growth rates. MRI is present if a disk is differentially rotating with a rate decreasing with distance from the center and has a weak poloidal magnetic field component (magnetic Mach number < 1). The linear global analysis of MRI-generated magnetic field disturbances shows an exponential growth $B \sim \exp(\gamma t)$ with the

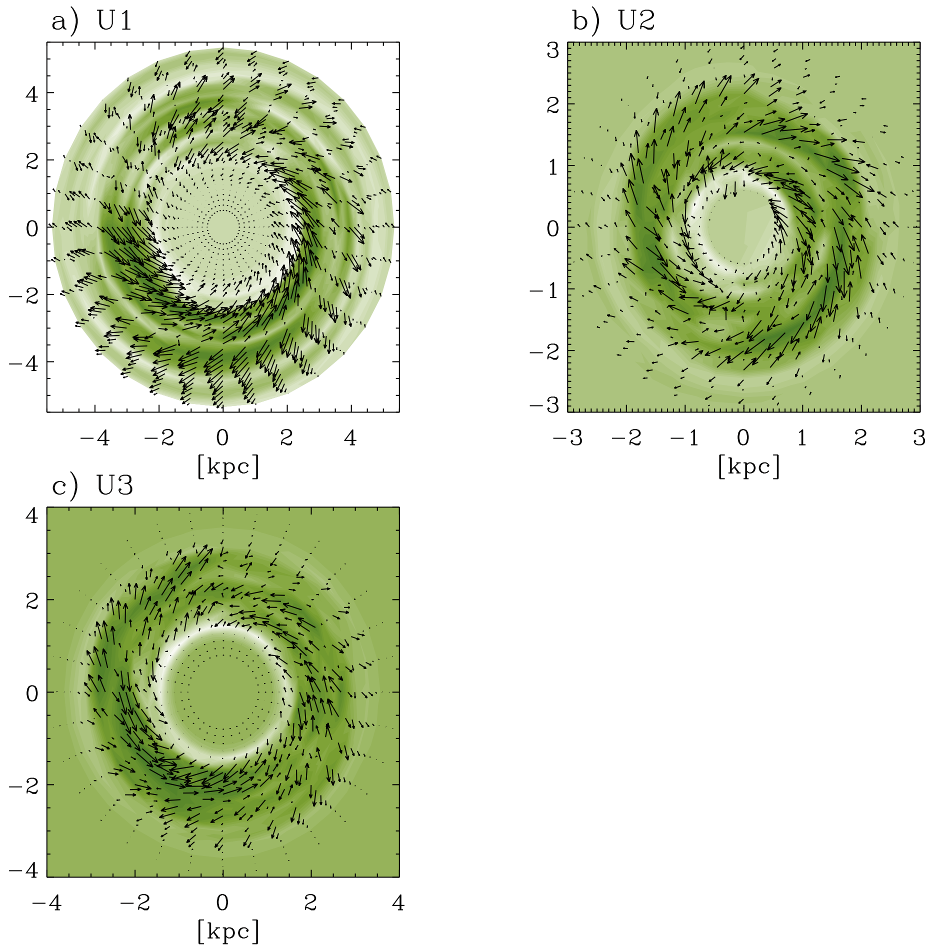

Figure 5.6: The density minima are shown in dark-green with over-plotted arrows of the magnetic field, for time slices $t = 1.2$ Gyr for U1, $t = 0.8$ Gyr for U2 and $t = 0.9$ Gyr for U3

growth rate $\gamma \simeq \tau_{\rm rot}^{-1}$, where $\tau_{\rm rot} = 2\pi/\Omega_0$ is a rotation time at the transition radius to differential rotation (Kitchatinov & Rüdiger 2004). The result was derived for a Brandt-type rotation law (Eq. (4.4)) with $n = 2$. As an example, for a rotation time of 70 Myr (NGC 6946, Sofue 1996) MRI can amplify a seed field of 10^{-12} G to the observed value of 10^{-6} G during 1 Gyr. Notice that the local analysis predicts $\gamma = 0.5q\Omega_0$ with normalized shear $q = -(R/\Omega_0)\partial\Omega/\partial R$. Since Ω_0 is $75{\rm Gyr}^{-1}$ and $100{\rm Gyr}^{-1}$ for models m2 and m3 (Table 5.3) with the maximal shear $q_{\rm max} = 0.4$, it is clear that the *local growth rates* are $15{\rm Gyr}^{-1}$ and $20{\rm Gyr}^{-1}$ respectively. The corresponding *local e-folding times* are 67 and $50{\rm Myr}$ for models m2 and m3. As will be shown below, the e-folding times are larger in the global case (compare with Table 5.3).

The instability is very fast: its e-folding time is only 44–86 Myr depending on

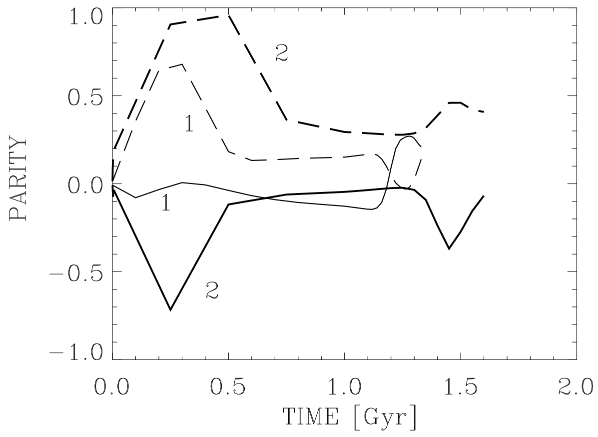

Figure 5.7: The magnetic parity $\mathcal{P}$ of the axisymmetric components of the magnetic fields of models m1 and m2 of Table 5.2 (solid). Dipole and quadrupole seem to balance. The parity of the axisymmetric components of the flow (dashed). The existence of mixed modes is evident for both magnetic field and flow

the strength of the rotation (Table 5.3). The global e-folding time $\tau_{\rm g}$ of the magnetic fields agrees with the global linear analysis prediction $\tau_{\rm g} \simeq \tau_{\rm rot}$ ($\tau_{\rm rot}$ is $84{\rm Myr}$ for model m2 and $63{\rm Myr}$ for model m3 in Table 5.2). These times are longer than the local theory predictions above. The reason is a decrease of the shear absolute value from 0.4 to 0.3 with the radius. Notice, that the magnetic field in model 3 will be amplified by a factor of 10^6 per Gyr in the global model, whereas the local prediction gives an amplification by a factor of 10^8 per Gyr.

The fastest growing instability we get for model U2, which has the highest $q\Omega_0$. Global e-folding time is about 44 Myr (Table 5.3). As we can see from Table 5.2 and Table 5.3, the equation $\gamma_{\rm global} = 1/\tau_{\rm rot} = \Omega_0/2\pi$ is valid only if the model has the $n = 2$ for rotation law. Models U1 and U2 do fit in it, while models U3 and U4 show some other behavior for growth rates.

We have calculated the radial dependence of the MRI growth rates from our global simulations. The growth rates for models U1 – U4 are shown in Fig. 5.8. The maximal growth rate of $25{\rm Gyr}^{-1}$ (model U2) appears at the radius $1.2\ {\rm kpc}$, which is very close to the transition radius $R_0 = 1\ {\rm kpc}$.We find that the growth rate radial dependence is reflecting the behavior of shear for all models. The Fig. 5.8 shows that the radial and azimuthal components of magnetic field are developing at any point in the disk although at a slower rate towards the outside.

Velocity dispersion. It is not surprising then that the velocity dispersion also appears to be strongly dependent on radius. Nevertheless, from observations of NGC 1058 we know that it drops from $12{\rm km/s}$ to $6{\rm km/s}$ at the inner part ($1 \leq R \leq$

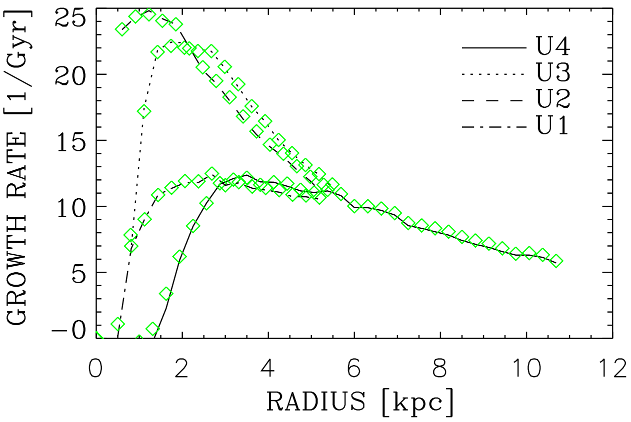

Figure 5.8: The growth rates of magnetic field components B_ϕ (lines) and B_R (rhombs) for the models in Table 5.2

$5\ \mathrm{kpc}$), then out to $R \simeq 11\ \mathrm{kpc}$ u_{T} remains almost fixed at about $5.7\mathrm{km/s}$. MRI appears to be the mechanism to explain the magnitude of velocity dispersion. From the radial behavior of growth rates we are now able to estimate the 'working' times for instability. For example, in our best-fit model U4 the disk part with radii between 3 and 6 kpc has a developed turbulence after 1.3 Gyr, whereas the outer part $>$ 10 kpc will need 2.7 Gyr to reach the same amplitudes. Therefore, the constancy of velocity dispersion might be explained by MRI. It may well be that the outer part of the rotation curve $u_\phi(R)$ of the NGC 1058 is in a reality not flat but a falling one as in the case of NGC 4144 (Braine 1993), Fig. 5.4. Then the turbulent dispersion ought to be closer to constant. Although the turbulent magnetic fields and the velocity dispersion are no constant values in the system with decreasing shear during the MRI evolution, the shape of the turbulent velocity radial distributions in Fig. 5.9 will change with time towards widening and flattening of the profile.

The average turbulence intensity slightly exceeds the value of 5 km/s. The characteristic amplitude of the magnetic field fluctuations is about 1 μG or, if expressed as Alfvén velocity, this corresponds to more than 20 km/s.

Fig. 5.10 presents the vertical profiles of the turbulent flow and magnetic field intensities. Both the flow and the magnetic field fluctuations show a minimum at the equator. This result agrees with the observation of strong turbulence in the galactic halos (Pietz et al. 1998; Kalberla et al. 1998; see Fletcher & Shukurov 2001) and with the computations by Fröhlich & Schultz (1996). Opinions are divided about the vertical distribution to be expected, if the interstellar turbulence would be driven by SN-explosions (Ferrière 1992; Kaisig et al. 1993; Ziegler 1996; Korpi et al. 1999). In a simple thinking, the SN-driven turbulence ought to have same distribution as the SNs themself, i.e. with the maximum at the galactic midplane. The profiles of the vertical turbulence in our 3D simulations provide a

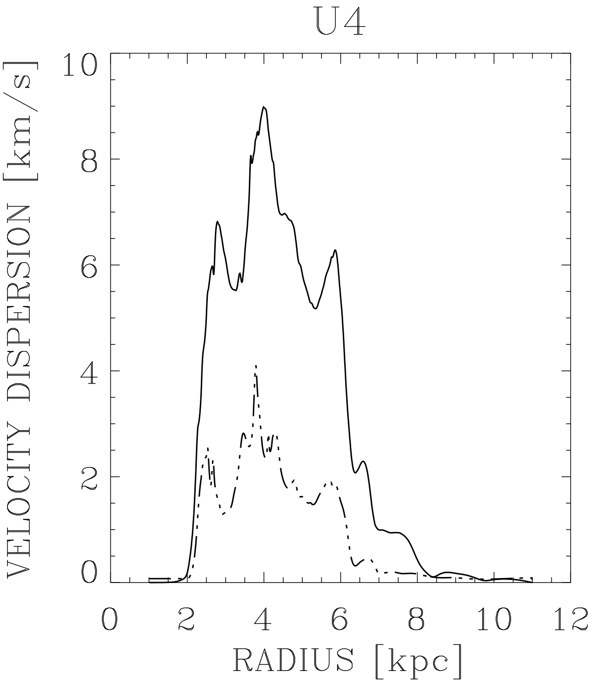

Figure 5.9: The radial dependence of the turbulent intensity $u_{\rm T}$ (solid line for horizontal and dashed line for the vertical dispersion) for model U4. The peaks correspond to the waves of the strong magnetic fields

good support to the α-dynamo theory. As it was discussed in Section 1.2.1, the sign of the turbulent velocity gradient is contributing to the sign of the α-tensor components (Eq. (1.34)). Outwardly increasing turbulent velocities are necessary for α-generation of the quadrupolar *regular* magnetic fields in a spiral galaxy.

Pitch angles: temporal and spatial behavior. The observed regular magnetic fields have the pitch angles $p = \tan^{-1}(B_{\rm R}/B_\phi)$ from $-10^{\rm o}$ to $-40^{\rm o}$ (Section 1.1.1, Fig. 1.1). In our global simulations, the magnetic fields have the pitch angle of about $-30^{\rm o}$ (Fig. 5.11). Comparing U1 and F1 models which have almost same pitch angles but large differences in shear, we see that there is no evidence for a pitch angle dependence on the shear strength. The averaged pitch angle $\langle\alpha\rangle_{Z,\phi}$ is shown in Fig. 5.12 with green for averaged values over northern hemidisk, pink for averages over southern hemidisk and blue for total average (dashed lines). There is no difference in pitch angle behavior above or below the equator. The magnetic field strength (red point) has strong dependence on radius, having its maximum near the transition radius R_0 while the pitch angles decrease in absolute value at $R \simeq R_0$. It is interesting, that high pitch angles are existing only for non-saturated MRI regime. 1–2 Gyr is a typical time for MRI to saturate in a galaxy. This is also

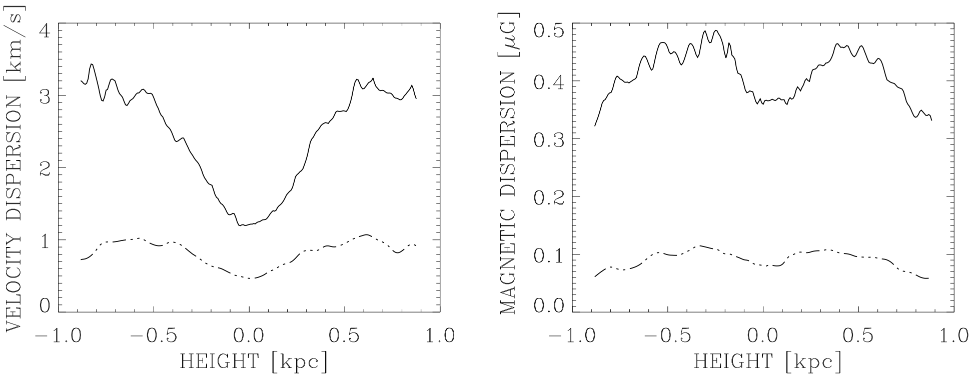

Figure 5.10: The turbulent intensity u_{T} (left) and the magnetic dispersion B_{T} (right) for model m1 have a minimum at the disk midplane after 1.33 Gyr. The same holds for u_z and B_z (dashed)

an average time between galactic encounters. Thus, the observed high pitch angles might well be due to MRI, as there is not sufficient time between two encounters to reach the saturation. After MRI saturates the pitch angles drop to values of -1°.

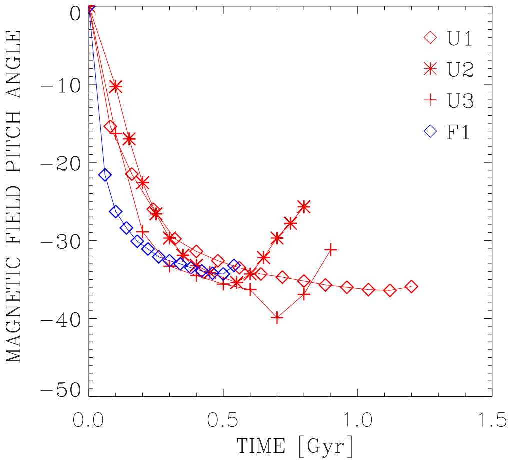

Figure 5.11: Pitch angles time evolution plotted for all models

Density radial profile. The MRI-driven density fluctuations in the Fig. 5.13 are not large enough to be of importance for the stellar formation in galaxies. The interesting point about density perturbations is the fact that they do not travel in radial direction. This might be very important for MRI in proto-planetary disks and planet formation. The dust grains until 1 meter size have a tendency to follow the

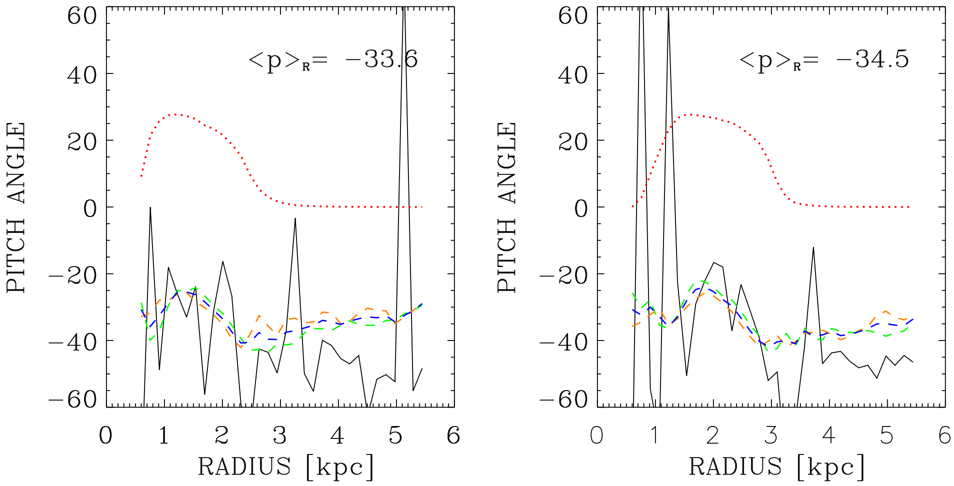

Figure 5.12: Left: model U2 at the time 0.7 Gyr. Right: model U3 at the time 0.9 Gyr. The averaged pitch angles $\langle p\rangle_{Z,\phi}$ are shown with green (average over northern hemidisk), pink (average over southern hemidisk) and blue (full average) dashed lines. The red dotted line represents the absolute value of the magnetic field $\left(10\times\langle B_R^2+B_\phi^2\rangle_{Z,\phi}^{1/2}\,\mu\mathrm{G}\right)$

dense regions in accretion disks (Johansen et al. 2004; Hodgson & Brandenburg 1998). The stable high density regions due to MRI might be important for the formation of rocky planetesimals.

Maxwell and Reynolds stresses. An important outcome of all simulations is the magnitude of the horizontal components of the Reynolds and Maxwell stresses. They are the terms that lead to angular momentum transport in the radial direction, as it can be seen from Eq. (3.58).

Our result is that the MRI-driven turbulence is magnetic-dominated: its magnetic energy exceeds the kinetic energy by a factor of 4 (Table 5.3). More dramatic is the situation concerning the angular momentum transport. The Reynolds stress is small and less than 1% of the Maxwell stress. The angular momentum transport is thus completely dominated by the magnetic field fluctuations.

The ratio of Maxwell to Reynolds stresses gives also the information about the pitch angles. Using the radial component of the Eq. (3.58), we have the relation

$$\frac{\mathrm{MS}}{\mathrm{RS}}=-\frac{\langle B'_R B'_\phi\rangle}{4\pi\langle\rho u'_R u'_\phi\rangle}, \tag{5.2}$$

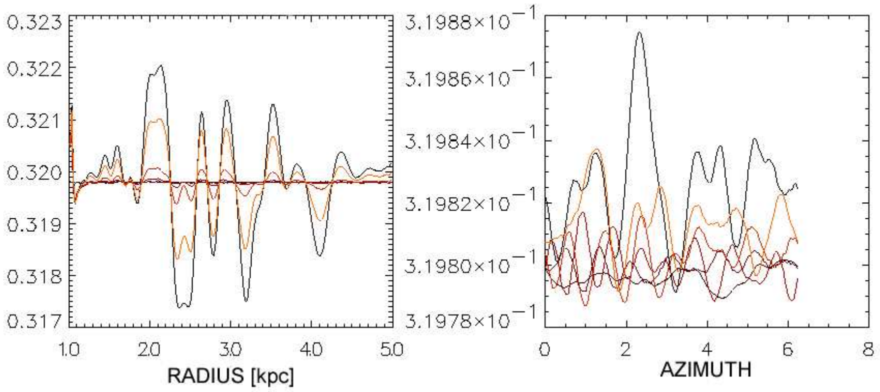

Figure 5.13: Radial dependence of the ϕ-averaged density field (left), ϕ dependence of the R-averaged density field (right), model U1. Density is plotted in $10^{-24}\ \mathrm{g/cm^3}$ units. The line at 0.320 corresponds to the initial state density at the galactic midplane $z = 0$. Black solid line corresponds to the density radial profile after 1.5 Gyr. Orange lines are show the density changes for the time slices between initial and final state

which can easily be rewritten as

$$\frac{\mathrm{MS}}{\mathrm{RS}} = -\frac{E_R^{\mathrm{mag}}}{E_R^{\mathrm{kin}}} \frac{\tan p^{\mathrm{kin}}}{\tan p^{\mathrm{mag}}}, \tag{5.3}$$

where within the current paragraph we adopt the notations of p^{kin} and p^{mag} for kinetic and magnetic pitch angles, E_R^{kin} and E_R^{mag} for kinetic and magnetic energies of the radial components.

We know that the $\tan p^{\mathrm{mag}} \to 1$ and $E_R^{\mathrm{mag}}/E_R^{\mathrm{kin}} \to 4$ while the ratio of stresses gives 400. We estimate then the kinetic pitch angle $p^{\mathrm{kin}} \simeq \pi/2$ for the $\tan p^{\mathrm{kin}} \to 100$. The ratio of Maxwell to Reynolds stresses provides us the information about the outward directed radial flows.

Table 5.4: Simulation results for models with magnetic diffusivity $\eta_{\rm T}$. Parameters of the rotation curve are common to all runs and correspond to those of model U3 in Table 5.2

model	$\eta_{\rm T}$ $[{\rm kpc}^2/{\rm Gyr}]$	T [Myr]	λ_Z [kpc]	λ_R [kpc]
U3	0.0	46	0.27	1
U3v1	0.01	45	0.3	1
U3v2	0.05	55	0.4	2
U3v3	0.1	66	0.5	4
U3v4	0.2	93	0.8	4

5.2 Influence of turbulent diffusivity

The molecular Ohmic dissipation is negligibly small in the galactic gaseous disks. Still, the turbulent dissipation driven by SN explosions can play some role for MRI. The models with magnetic diffusivity from $\eta = 0.01\ {\rm kpc}^2/{\rm Gyr}$ till $\eta = 0.2\ {\rm kpc}^2/{\rm Gyr}$ are presented in the Table 5.4 and at the Figs. 5.14- 5.18. The input parameters for the models, such as the rotation law, density stratification and resolution, are chosen to be identical to the model U3 in Table 5.2.

The e-folding time is found to grow with increasing magnetic diffusivity, as we have shown in Table 5.4. We found that increasing $\eta_{\rm T}$ leads the magnetic field saturation times longer than 2 Gyr (Fig. 5.14). That might be critical for the MRI application to galaxies. Still, we have started our calculations with an extremely small initial magnetic energies of horizontal field components (see Fig. 5.14). In reality, taking into account frequent collisions and interactions between galaxies, the initial magnetic field for MRI might be a few orders higher and have the a form of very distorted and partly dissipated former regular fields. Equally, the growth of MRI to the saturation will take less time with higher initial rms velocities. In addition, external magnetic fields for a galaxy are not necessary small, they may be up to a few μG (Section 1.2.2). In case when the magnetic fields need to be restored only a few orders, even MRI with higher ($\eta_{\rm T} > 0.2\ {\rm kpc}^2/{\rm Gyr}$) is of interest.

With increasing of turbulent diffusivity the critical wavenumbers are larger than the predicted in Eq. (3.29) numbers. The impact of magnetic diffusivity is that the small scales are dissipated away. The larger is $\eta_{\rm T}$ the larger is be the ‘shortest possible’ unstable wavelength λ_z, which are given in Table 5.4. The turbulence on larger scales requests more time to be excited.

Model U3v1 with $\eta_{\rm T} = 0.01\ {\rm kpc}^2/{\rm Gyr}$ is hardly different from the non-diffusive U3 both in e-folding time and the critical wavelength. To see the impact of turbulent diffusivity in this case one needs to increase the resolution. The broadening of the turbulent energy spectra is demonstrated in Figs. 5.15 – 5.16. Magnetic turbulent energies are much less peaked not at critical MRI wavelength

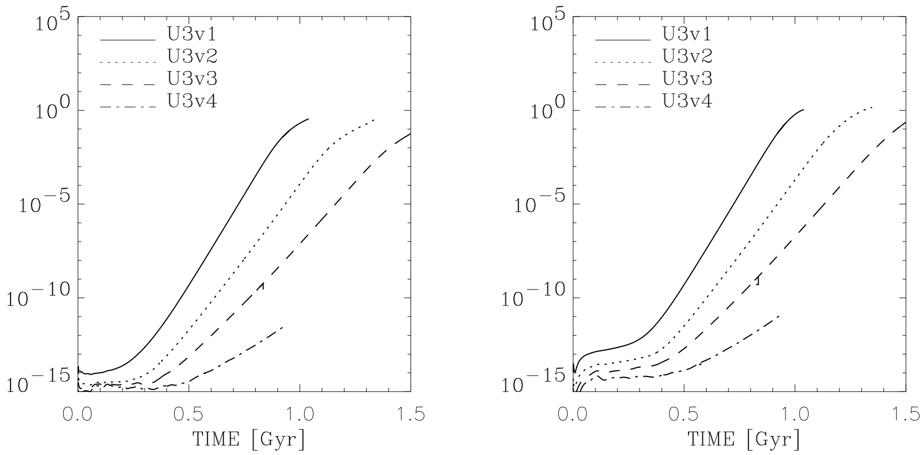

Figure 5.14: The magnetic energy of radial (left) and azimuthal (right) field components for models with non-vanishing magnetic diffusivity

during the simulation comparing to non-diffusive models. With approaching the saturation regime the magnetic spectra become of the $k^{-5/2}$ slope. For velocities a different behavior is observed. The kinetic spectra of horizontal flows are close to the $k^{-5/3}$ Kolmogorov spectrum and do not evolve much during the calculation.

For larger diffusivities, the diffusive cut-off is clearly visible both on magnetic and kinetic energy spectra (Fig. 5.17, Fig. 5.18). From the comparison of the magnetic energy for different scales, MRI leads to the appearance of large-scale fields with dominating B_ϕ component. Both velocity and magnetic spectra are showing an anisotropic behavior of the turbulence.

Our results are consistent with the description of the shear instability behavior with non-vanishing Ohmic dissipation, considered in both the linear (Jin 1996) and nonlinear (Sano et al. 1998) regimes. The models correspond to the top-right corner of stability diagram (Fig.1, Kitchatinov & Rüdiger 2004). For the initial magnetic fields which are close to the cut-off value (Eq. (3.54)) or, in terms of magnetic Reynolds numbers $\mathrm{Rm} = 1$, the presence of turbulence diffusion leads to the stability of the system. It happens due to the growth of the critical wavelength over the disk height. On the example of U3v4 model, we would need to employ $\eta_\mathrm{T} > 7\ \mathrm{kpc}^2/\mathrm{Gyr}$ for the magneto-hydrodynamical stability of the disk.

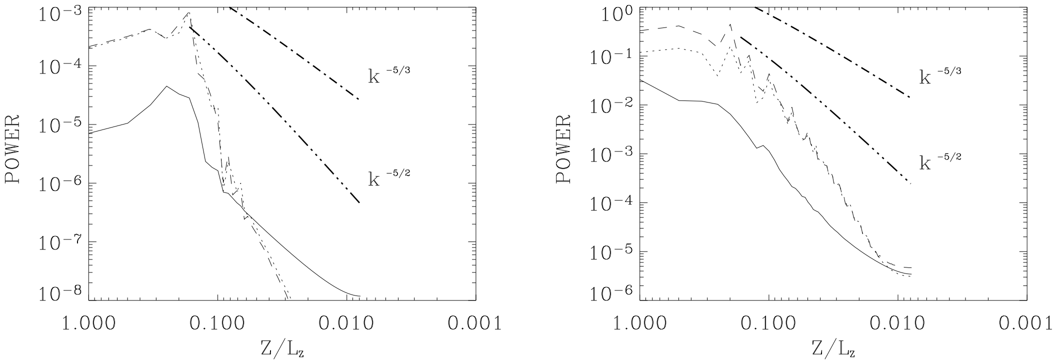

Figure 5.15: Magnetic spectra, model U3v1 ($\eta_T = 0.01\ \mathrm{kpc}^2/\mathrm{Gyr}$) for time 0.8 Gyr (left) and 1.0 Gyr (right). Vertical, radial and azimuthal energy components are plotted as solid, dotted and dashed lines

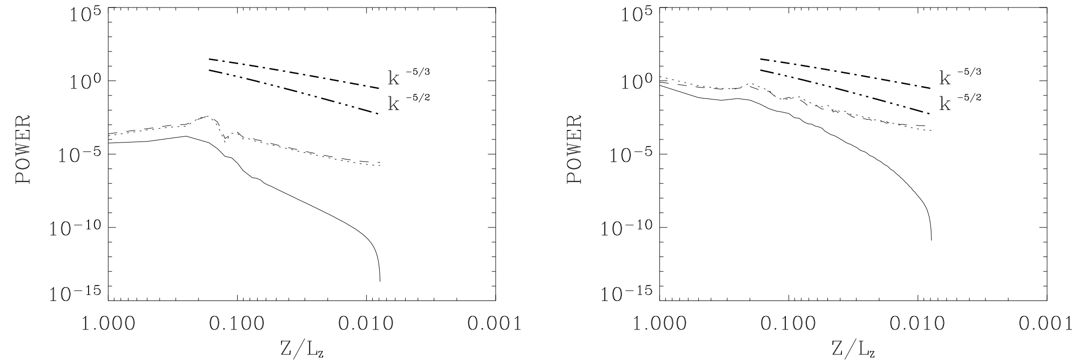

Figure 5.16: Kinetic spectra, model U3v1 ($\eta_T = 0.01\ \mathrm{kpc}^2/\mathrm{Gyr}$) for time 0.8 Gyr (left) and 1.0 Gyr (right). Vertical, radial and azimuthal energy components are plotted as solid, dotted and dashed lines

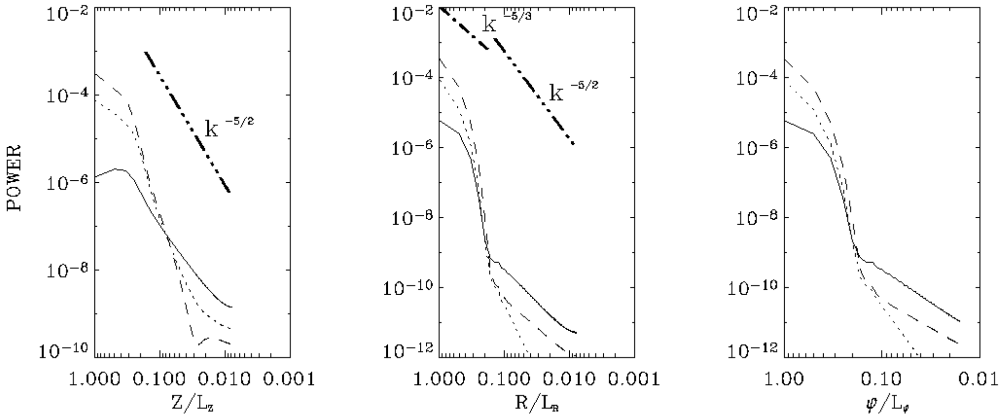

Figure 5.17: Magnetic spectra of the model U3v4 ($\eta_{\rm T} = 0.2\,{\rm kpc}^2/{\rm Gyr}$, time is 1.7 Gyr). Vertical, radial and azimuthal energy components are plotted as solid, dotted and dashed lines

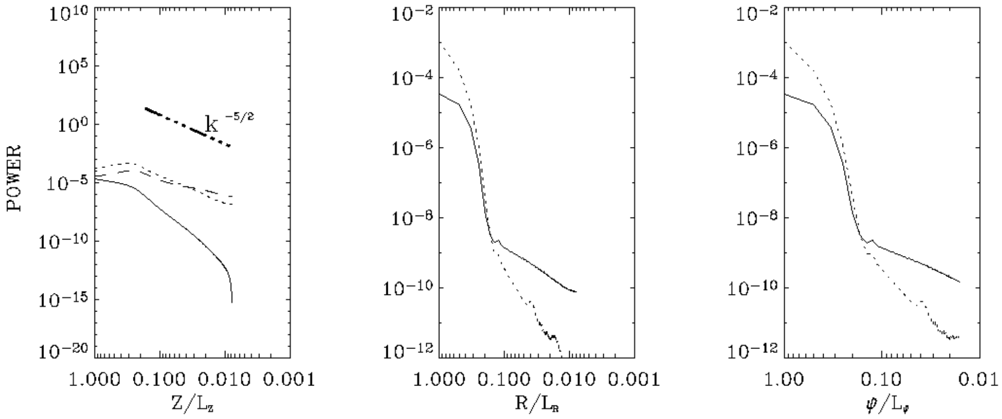

Figure 5.18: Kinetic spectra of the model U3v4 ($\eta_{\rm T} = 0.2\,{\rm kpc}^2/{\rm Gyr}$, time is 1.7 Gyr). Vertical, radial and azimuthal energy components are plotted as solid, dotted and dashed lines

Table 5.5: Density-stratified models with zero-flux initial magnetic field. Last model ($\mathrm{zflux2_d}$) has non-zero magnetic diffusivity $\eta_{\mathrm{T}} = 0.05\mathrm{kpc}^2/\mathrm{Gyr}$. Parameters of the rotation curve are common to all runs and correspond to those of the model m3 (see Table 5.2)

Models	$V_{\mathrm{A,in}}$ $[\mathrm{km/s}]$	u_{T} $[\mathrm{km/s}]$	orbits (outside)	λ_z [kpc]	B_{sat} μG
zflux1	0.9	2.2	189	0.22	2.2
zflux2	0.3	1.25	74	0.07	1.1
$\mathrm{zflux2_d}$	0.3	1.4	85	0.2	1.3

5.3 MRI with flux-free initial magnetic field

It is known that non-zero magnetic flux models for MRI are problematic in a sense of not reaching the saturation regime. With the scheme remaining stable over the calculation, the turbulent Alfvén velocities are strongly increasing in the outer parts of disk with the decrease of density. This leads to a drastic reduction in the length of the time step. In this situation, reaching the saturation in MRI in the outer disk is practically impossible because it becomes too time consuming. An easy way out is the non-zero flux model with no density stratification and periodical boundary conditions in vertical direction, which we have used in Section 5.1.1.

Another way to avoid the numerical difficulties is to use zero-net magnetic flux as initial condition, although the assumption of magnetic fields being proportional to $\sin(\phi)$ (Section 4.1) is not a very realistic one. The runs with the initial zero-net magnetic flux can be easily saturated, but, compared to results of the net-flux models, the resulting magnetic fields have smaller amplitudes. A reason of smaller turbulent amplitudes may lay in the mechanism of saturation. At first, the initial $\sin\phi$ magnetic field is acting as a bar. After some time the ‘arms’ of the field are wound up. At a certain moment the two magnetic ‘arms’, which have the opposite sign in B_z, will merge. The merging is giving us the situation when the initial B_z is removed. The observed saturation in turbulence does not occur because of arriving at the critical physical parameters or instability termination conditions. The saturation occurs because of vanishing vertical fields from which the instability loops are formed. The resolution of our models is not sufficient to get the MRI working from turbulent B_{T} or from the toroidal component of the magnetic field.

Saturated magnetic fields have smaller magnitudes compared to the cases with a homogeneous initial vertical field. But they do not depend on the strength of the initial magnetic field so clearly as in case with non-zero initial flux. This is shown in the last column in Table 5.5 when comparing the models zflux1 and zflux2. It is interesting, that only radial and azimuthal components are growing exponentially,

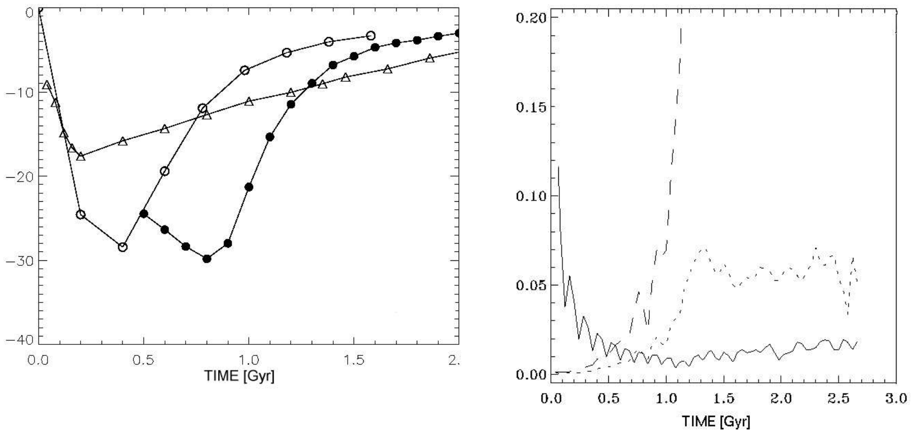

Figure 5.19: Left: Magnetic pitch angle time behavior is shown for zero-flux models (Table 5.5). Filled circles are for model zflux1, empty circles are for zflux2 and triangles are used for model $\mathrm{zflux2_d}$. Right: Time development of vertical (solid line), radial (dotted line) and azimuthal (dashed line) components of the magnetic field (absolute values after averaging), model zflux1

while the vertical magnetic field decreases, Fig. 5.19 (right). Comparing the behavior of the saturated magnetic fields given in Section 5.1.1 (Fig. 5.3) with the zero-net flux solution (Fig. 5.19, right) suggests that there are two different global MRI solutions leading to different states of saturation.

Unfortunately, we can not answer the question of α-dynamo operating together with MRI with the simulations in Section 5.1.3. First, all three components of the magnetic field should show an exponential growth when α-dynamo was operating. Second, a stable dynamo solution should survive in the disk at least for a few longer diffusion times. In the presented models the diffusivity is mostly zero, which means the infinite diffusion time. In the case of $\eta_\mathrm{T} = 0.05\ \mathrm{kpc^2/Gyr}$ in the $\mathrm{zflux_d}$ model, the diffusion time is still huge, $\sim$ 200 Gyr. Applying the larger magnetic diffusivities decreases the MRI growth rate drastically (Sect. 5.2.), which therefore will cost a lot of computational time.

For the models in Table 5.5, the magnetic pitch angles reach the observed value -30^o within 1 Gyr, its maxima correspond to the system reaching saturation. Soon afterwards there is a decrease of the pitch angles, which become quite small (-1^o) in 1.5 – 2 Gyr. Fig. 5.19 (left) is demonstrating how the difference in the initial magnetic field affects the saturation time (models zflux1 and zflux2). The presence of magnetic diffusivity (model $\mathrm{zflux2_d}$, empty triangles on Fig. 5.19, left) is not only prolonging the time requested for MRI saturation, as we have demonstrated in previous section, but it is also decreasing the absolute value of the pitch angle from 30^o to 18^o.

The velocity dispersion does not seem to be affected by the magnitude of the initial magnetic field or the presence of magnetic diffusivity. It remains comparable to the observed velocity dispersion within an order of magnitude (see Section 1.5), although the numbers are smaller compared to the average $5\ \mathrm{km/s}$ in net-flux models (Table 5.2).

Chapter 6

Conclusions

The origin and symmetry of the observed global magnetic fields in galaxies are not fully understood. In this thesis we intend to clarify the question of the magnetic field origin. For that purpose we investigate the global action of the magneto-rotational instability (MRI) in galactic disks with the help of 3D global magneto-hydrodynamical (MHD) simulations. The calculations were done with the time-stepping ZEUS 3D code, using massive parallelization. Our nonlinear simulations provide both, expected as well as unexpected aspects of the global action of MRI.

The $\alpha\Omega$-dynamo is known to be one of the most efficient mechanisms to reproduce the observed global galactic fields. The presence of strong turbulence is a pre-requisite for the $\alpha\Omega$-dynamo generation of the regular magnetic fields. The observed magnitude and spatial distribution of turbulence in galaxies still presents unsolved problems to theoreticians. Magneto-rotational instability is known to be a fast and powerful mechanism to generate MHD turbulence and to amplify magnetic fields.

We confirm the linear theory prediction that the critical wavelength of the instability is proportional to the initial magnetic field strength. We find that the wavelength should increase with the increasing magnetic fields during the simulation, transporting the energy from critical to larger scales. The final structure, if not disrupted by supernovae explosions, is the structure of ‘thin layers’ of thickness of about 100 pcs. The amplitudes of the turbulent magnetic fields are related as $\delta B_z \ll \delta B_R < \delta B_\phi$. It might be possible to observe these structures with high resolution radio polarization data.

The resulting turbulence pattern exhibits either spiral or more ring-like structures, but the Maxwell stress $\langle B_R^{'} \cdot B_\phi^{'} \rangle$ is always negative, so that the angular momentum is always transported outwards. An important outcome of all simulations is the magnitude of the horizontal components of the Reynolds and Maxwell stresses. The result is that the MRI-driven turbulence is magnetic-dominated: its magnetic energy exceeds the kinetic energy by a factor of 4 (Table 5.3). More dramatic is the situation concerning the angular momentum transport: The Reynolds stress is small and less than 1% of the Maxwell stress. The angular momentum transport is thus completely dominated by the magnetic field fluctuations. We have demonstrated that there is evidence for radial flows within the growth time of the MRI.

Although the magnetic fields have reversals between the ‘rings’, the volume-averaged pitch angle is always negative with a magnitude of about -30°. The non-saturated MRI regime lasts sufficiently long to fill the time between galactic encounters, independently of strength and geometry of the initial field. Therefore, we may claim the observed pitch angles can be due to MRI action in the gaseous galactic disks.

MRI is also shown to be a very fast instability with e-folding time of $\tau_{\rm rot} = 2\pi/\Omega_0$, for the Brandt type rotation law with $n = 2$, and with nearly doubled growth rate in case of the rotation law $n = 4$. The local estimation of the growth rates 0.5Ω holds at any fixed radius in the global models of the magnetic field evolution. Steep rotation curves imply a stronger growth for the magnetic energy due to MRI. The global e-folding time of MRI is from 44 Myr to 100 Myr depending on the rotation profile. Therefore, MRI explains the existence of rather large magnetic fields in very young galaxies.

We also successfully reproduced the observed rms values of velocities in the interstellar turbulence, as it was observed in NGC 1058. We have also confirmed the prediction of Sellwood & Balbus (1999), that the turbulent velocity dispersion is linked to the Alfvén speed. In addition, we have shown with the simulations that the averaged velocity dispersion of about 5 km/s is a typical number for the magneto-rotational instability in galaxies, which again agrees with observations.

Another important property of the MRI-driven turbulence is that the dispersion increases outside of the disk plane, whereas supernovae-driven turbulence is found to be concentrated within the disk. The velocity turbulence increasing outwards is quite important for deciding the question how the galactic dynamo is driven. In our simulations the velocity dispersion increases a few times with height. This effect does not appear, however, in the models with homogeneous density profile.

An additional support to the dynamo α-effect in the galaxies is the ability of the MRI to produce a mix of quadrupole and dipole symmetries from the purely vertical seed fields.

We have shown that in order to stop the MRI, there should be unrealistically high magnetic diffusivity. High magnetic diffusivity makes the instability evolve very slowly and on large scales. This situation may appear in freshly distorted or disrupted galactic disks.

A surprising outcome is the dependence of the strength of saturated fields on the initial magnetic field strength. This dependence occurs in the net-flux models with large initial magnetic fields in the vicinity of marginally stable states, and it is much weaker in the zero-net flux models . We suggest that this dependence is due to the restricted nonlinearity of the simulations with large initial fluxes.

The interaction of magneto-rotational instability and random supernovae explosions remains an open question. It would be desirable to run the simulation with the supernovae explosions included. They would disrupt the calm ring structure produced by global MRI, may be even to the level when we can no longer blame MRI to be responsible for the turbulence.

A further massive improvement could be obtained by including the spiral waves in the gravitational potential. They would influence the spatial behavior of the pitch angles, flows and also, of course, the angular momentum transport. We might then obtain the global magnetic field picture which is much closer to the observed one. We hope, that growing computing power will allow us to avoid the diffusivity time scale problem in the near future. We could then obtain the global $\alpha\Omega$-dynamo operating together with both MRI and supernovae driven turbulence.

Appendix

A.1 Derivative operators in cylindrical coordinates

In cylindrical coordinates (z, R, ϕ) the derivative operators have the form

$$\frac{D}{Dt} = \frac{\partial}{\partial\, t} + u_z \frac{\partial}{\partial z} + u_R \frac{\partial}{\partial R} + \frac{u_\phi}{R} \frac{\partial}{\partial \phi},$$

$$\mathrm{div}\boldsymbol{B} = \frac{\partial B_z}{\partial z} + \frac{1}{R} \frac{\partial R B_R}{\partial R} + \frac{1}{R} \frac{\partial B_\phi}{\partial \phi},$$

$$\mathrm{grad}\Psi = \hat{\boldsymbol{e}}_{\boldsymbol{z}} \frac{\partial \Psi}{\partial z} + \hat{\boldsymbol{e}}_{\boldsymbol{R}} \frac{\partial \Psi}{\partial R} + \hat{\boldsymbol{e}}_{\boldsymbol{\phi}} \frac{1}{R} \frac{\partial \Psi}{\partial \phi},$$

$$\mathrm{curl}\boldsymbol{B} = \hat{\boldsymbol{e}}_{\boldsymbol{z}} \frac{1}{R} \left(\frac{\partial}{\partial R}(R B_\phi) - \frac{\partial B_R}{\partial \phi} \right) + \hat{\boldsymbol{e}}_{\boldsymbol{R}} \left(\frac{1}{R} \frac{\partial B_z}{\partial \phi} - \frac{\partial B_\phi}{\partial z} \right) + \hat{\boldsymbol{e}}_{\boldsymbol{\phi}} \left(\frac{\partial B_R}{\partial z} - \frac{\partial B_z}{\partial R} \right).$$

A.2 Basic electrodynamic equations

Ohm's law is

$$\boldsymbol{j} = \sigma(\boldsymbol{E} + \boldsymbol{u} \times \boldsymbol{B} + \alpha \boldsymbol{B}), \tag{1}$$

where σ is a conductivity. Maxwell equation is

$$\frac{\partial \boldsymbol{B}}{\partial t} = -\nabla \times \boldsymbol{E}, \tag{2}$$

where $\boldsymbol{E}$ can be taken from Ohm's law

$$\boldsymbol{E} = \frac{\boldsymbol{j}}{\sigma} - \boldsymbol{u} \times \boldsymbol{B} - \alpha \boldsymbol{B}. \tag{3}$$

The combination leads to the induction equation.

Table 1: Test models for MRI with homogeneous vertical magnetic field. u_{T} stands for initial rms velocity strength. q_{lin} and q_{square} are the linear and square artificial viscosities. $B_0 = 0.11\,\mu\mathrm{G}$. $u_{\mathrm{T}}|_{\mathrm{min}}$ [km/s] is the value at which the code will smooth down the initially given velocity dispersion u_{T}

run	u_{T} [km/s]	q_{square}	q_{lin}	$u_{\mathrm{T}}\|_{\mathrm{min}}$ [km/s]	stabilization
t1	0.06	2.0	0.2	0.034	no
t2	0.12	2.0	0.2	0.07	no
t3	0.26	2.0	0.2	0.16	no
t4	10	2.0	0.2	0.42	no
t5	28	2.0	0.2	0.53	no
t6	28	0.0	0.0	0.66	no

A.3 MRI with initial free-decaying turbulence

In Table 1 we give those models, in which the calculation starts with high free-decaying random velocities . The box size and resolution are the same as in Section 4.3. In the fifth column of the Table 1 we have placed $u_{\mathrm{T}|\mathrm{min}}$ which is a minimum value of velocity dispersion during the simulation. Numerical dissipation is responsible for the decrease of rms velocities till the $u_{\mathrm{T}|\mathrm{min}}$ value within a time of about 0.05 – 0.10 Gyr. On these examples one can see how diffusive Zeus code is.

The energy plots are shown in Fig. A.1. The MRI-generated horizontal magnetic fields starts to grow from the sufficiently higher energy levels, comparing Fig. A.1 with Fig. 5.3.

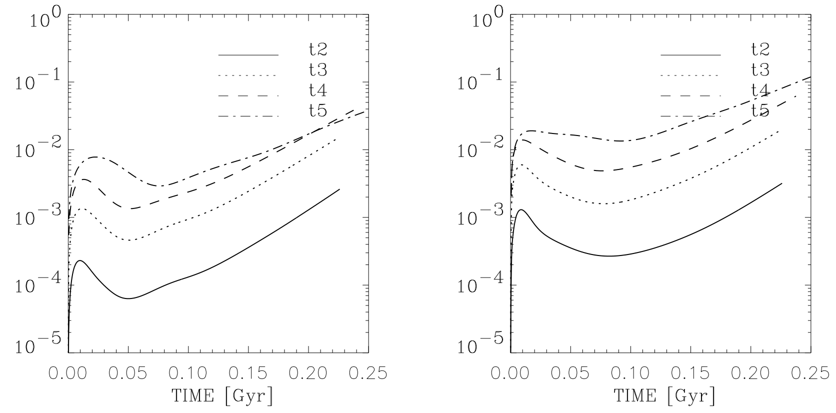

Figure A.1: The magnetic energies of the radial component (left) and the azimuthal component (right)

Bibliography

[1] Arlt, R., Urpin, V.A., 2004, A&A, 426, 755

[2] Balbus, S.A., Hawley, J.F., 1991, ApJ, 376, 214

[3] Balbus, S.A., Hawley, J.F., 1992, ApJ, 400, 595

[4] Beck, R., 1993, *The Cosmic Dynamo*, Eds: F. Krause et al., Kluwer, p. 283

[5] Beck, R., Poezd, A. D., Shukurov, A., Sokoloff, D. D., 1994, A&A, 289, 94

[6] Beck, R., Hoernes, P., 1996, Nature, 379, 47

[7] Beck, R., Berkhuijsen, E. M., Uyaniker, B., 1999, *Plasma Turbulence and Energetic Particles in Astrophysics*, Proc. of International Conference Cracow, Eds.: M. Ostrowski et al., Obserwatorium Astronomiczne, Uniwersytet Jagiellonski Kraków, p. 5

[8] Beck, R., 2000, Phil. Trans. R. Soc. Lond. A., 358, 777

[9] Berger, M.A., Field, G.B., 1984, J. Fluid Mech., 147, 133

[10] Berkhuijsen, E.M., Bajaja, E., Beck, R., 1993, A&A, 279, 359

[11] Berkhuijsen, E.M., 1998, Lecture Notes in Physics, 506, *The Local Bubble and Beyond* Proc. of the IAU Colluquium No. 166, Garching (Germany), Eds.: D. Breitschwerdt et al., Springer, p. 301

[12] Berkhuijsen, E.M., 1999, *Plasma Turbulence and Energetic Particles in Astrophysics*, Proc. of International Conference Cracow, Eds.: M. Ostrowski et al., Obserwatorium Astronomiczne, Uniwersytet Jagiellonski Kraków, p. 61

[13] Binney, J., Tremaine, S., 1990, *Galactic dynamics*, Princeton University Press

[14] Bondi, M., Padrielli, L., Gregorini, L., Mantovani, F., Shapirovskaya, N., Spangler, S. R., 1994, A&A, 287, 390

[15] Braine, J., Combes, F., van Driel, W., 1993, A&A, 280, 451

[16] Brandenburg, A., Moss, D., Tuominen, I., 1992, A&A, 256, 328

[17] Brandenburg, A., Nordlund, Å., Stein, R. F., Torkelsson, U., 1995, ApJ, 446, 741

[18] Brandenburg, A., Nordlund, Å., Stein, R. F., Torkelsson, U. 1996, *Physics of Accretion Disks*, Eds: S. Kato et al., Gordon and Breach Science Publishers, p. 285

[19] Brandenburg, A., Schmitt, D., 1998, A&A, 338, L55

[20] Brandenburg, A., Dobler, W., 2001, A&A, 369, 329

[21] Brandenburg, A., Dobler, W., Subramanian, K., 2002, Astron. Nachr., 323, 99

[22] Brown, J.C., Taylor, A.R., Jackel B.J., 2003, ApJS, 145, 213

[23] Cattaneo, F., Vainshtein, S.I., 1991, ApJ Lett., 376, L21

[24] Chandrasekhar, S., 1960, Proc. Nat. Acad. Sci., 46, 53

[25] Chandrasekhar, S., 1961, *Hydrodynamic and hydromagnetic stability*, International Series of Monographs on Physics, Oxford: Clarendon

[26] Chini, R., Kruegel, E., Kreysa, E., 1986, A&A, 167, 315

[27] Cordes, J.M., Rickett, B.J., 1998, ApJ, 507, 846

[28] Dickey, J.M., Garwood, R.W., 1989, ApJ, 341, 201

[29] Dickey, J.M., Hanson, M.M., Helou, G., 1990, ApJ, 352, 522

[30] Dickey, J.M., Lockman, F.J., 1990, ARA&A, 28, 215

[31] Drapatz, S., Zinnecker, H., 1984, MNRAS, 210, 11

[32] Drecker, A., Rüdiger, G., Hollerbach, R., 2000, MNRAS, 317, 45

[33] Dubrulle, Laval, J.-P., Nazarenko, S., Zaboronski, O., 2004, J. Fluid Mech., 520, 1

[34] Elmegreen, D.M., Elmegreen, B.G., 1982, MNRAS, 201, 1021

[35] Elmegreen, D.M., Elmegreen, B.G., 1987, ApJ, 314, 3

[36] Elmegreen, B.G., Falgarone, E., 1996, ApJ, 471, 816

[37] Elstner, D., Meinel, R., Rüdiger, G., 1990, Geophys. Astrophys. Fluid Dyn., 50, 85

[38] Elstner, D., Golla, G., Rüdiger, G., Wielebinski, R., 1995, A&A, 297, 77

[39] Elstner D., Rüdiger G., Schultz M., 1996, A&A, 306, 740

[40] Elstner, D., Otmianowska-Mazur, K., von Linden, S., Urbanik, M., 2000, A&A, 357, 129

[41] Falle, S.A.E.G., 2002, ApJ, 577, L123

[42] Ferrière, K., 1992, ApJ, 389, 286

[43] Ferrière, K., 1993a, ApJ, Part 1, 404, 1, 162

[44] Ferrière, K., 1993b, ApJ, Part 1, 409, 1, 248

[45] Ferrière, K., 1996, A&A, 310, 438

[46] Ferrière, K., 1998, A&A, 335, 488

[47] Ferrière, K., Schmitt, D., 2000, A&A, 335, 488

[48] Fitt, A.J., Alexander, P., 1993, MNRAS, 261, 445

[49] Fletcher, A., Shukurov, A., 2001, MNRAS, 325, 312

[50] Fricke, K., 1969, A&A, 1, 388

[51] Fröhlich, H.-E., Schultz, M., 1996, A&A, 311, 451

[52] Green, D.A., 1993, MNRAS, 262, 328

[53] Golla, G., Wielebinski, R., 1994, A&A, 286, 733

[54] Han, J.L., Manchester, R.N., Lyne, A.G., Qiao, G.J., 2002, ApJ, 570, L17

[55] Hanasz, M., Lesch, H., 1993, A&A, 278, 561

[56] Hanasz, M., Lesch, H., 1997, A&A, 321, 1007

[57] Hanasz, M., Lesch, H., 1998, A&A, 332, 77

[58] Hanasz, M., Lesch, H., 2000, A&A, 543, 235

[59] Hanasz, M., Kowal, G., Otmianowska-Mazur, K., Lesch, H., 2004, ApJ, 605, L33

[60] Haugen, N.E.L., Brandenburg, A., Dobler, W., 2003, ApJ, 597, L141

[61] Hawley, J., Balbus, S., 1991, ApJ, 376, 223

[62] Hodgson, L.S., Brandenburg, A., 1998, A&A, 330, 1169

[63] Jin, L., 1996, ApJ, 457, 798

[64] Johansen, A., Andersen, A.C., Brandenburg, A., 2004, A&A, 417, 361

[65] Kaisig, M., Rüdiger, G., Yorke, H.W., 1993, A&A, 274, 757

[66] Kalberla, P.M.W., Westphalen, G., Mebold, U., 1998, A&A, 332, L61

[67] Kitchatinov, L.L., Rüdiger, G., 1992, A&A, 260, 494

[68] Kitchatinov, L.L., Rüdiger, G., 2004, A&A, 424, 565

[69] Klahr, H., Bodenheimer, P., 2003, ApJ, 582, 869

[70] Korpi, M.J., Brandenburg, A., Shukurov, A., 1999, ApJ, 514, L99

[71] Korpi, M. J., Mac Low, M.-M., 2003, Astron. Nachr. Suppl., 324, 67

[72] Krause, F., Beck, R., 1998, A&A, 335, 789

[73] Krause, F., Rädler, K.-H., 1980, *Mean-Field Magneto-hydrodynamics and Dynamo Theory* , Akademie Verlag Berlin

[74] Kronberg, P.P., Perry, J.J., Zukowski, E.L., 1992, ApJ, 387, 528

[75] Lesch, H., Hanasz, M., 2003, A&A, 401, 809

[76] Lyne, A. G., Smith, F. G., 1989, MNRAS, 237, 533

[77] Meinel, R., 1990, Geophys. Astrophys. Fluid Dyn., 50, 79

[78] Minter, A.H., Spangler, S.R., 1996, ApJ, 458, 194

[79] Minter, A.H., Spangler, S.R., 1997, ApJ, 485, 182

[80] Miyamoto, M., Nagai, R., 1975, Astron. Soc. of Japan Publ., 27, 4, 533

[81] Moffatt, K.H., 1970, J. Fluid Mech., 28, 571

[82] Molemaker, M.J., McWilliams, J.C., Yavneh, I., 2001, Phys. Rev. Letters, 86, 5270

[83] Otmianowska-Mazur, K., Chiba, M., 1995, A&A, 301, 41

[84] Otmianowska-Mazur, K., Elstner, D., Soida, M., Urbanik, M., 2002, A&A, 384, 48

[85] Otmianowska-Mazur, K., 2003, A&A, 408, 817

[86] Parker, E.N., 1971, ApJ, 164, 491

[87] Parker, E.N., 1979, *Cosmical Magnetic Fields: Their Origin and Their Activity*, Oxford University Press

[88] Parker, E.N., 1992, ApJ, 401, 809

[89] Pietz, J., Kerp, J., Kalberla, P.M.W., 1998, A&A, 332, 55

[90] Poezd, A., Shukurov, A., Sokoloff, D., 1993, MNRAS, 264, 285

[91] Pogge, R.W., 1989, ApJS, 71, 433

[92] Pynzar, A.V., 1993, Astron. Rep., 37, 245

[93] Rand, R. J., Lyne, A. G., 1994, MNRAS, 268, 497

[94] v. Rekowski M., Rüdiger G., Elstner D., 2000, A&A, 353, 813

[95] Rickett, B.J., 1990, ARA&A, 28, 561

[96] Rickett, B.J., Coles, W.A., Markkanen, J., 2000, ApJ, 533, 304

[97] Rohde, R., Elstner., D., 1998, A&A, 333, 27

[98] Rohde, R., Beck, R., D. Elstner, D., 1999, A&A, 350, 423

[99] Rüdiger, G., 1978, Astron. Nachr., 299, 4, 217

[100] Rüdiger, G., 1990, Geophys. Astrophys. Fluid Dyn., 50, 53

[101] Rüdiger, G., Elstner, D., Schultz, M., 1993, *The Cosmic Dynamo*, IAU Symp. 157, Eds.: F. Krause et al., 321

[102] Rüdiger, G., Kitchatinov, L.L., 1993, A&A, 269, 581

[103] Rüdiger G., Elstner D., Stepinski T.F., 1995, A&A, 298, 934

[104] Rüdiger, G., Primavera, L., Arlt, R., Elstner, D., 1999, MNRAS, 306, 913

[105] Rüdiger, G., Pipin, V.V., 2000, A&A, 375, 149

[106] Rüdiger G., Pipin V.V., Belvedere G., 2000, Solar Phys., 198, 241

[107] Rüdiger, G., Hollerbach, R., 2004, *The Magnetic Universe. Geophysical and Astrophysical Dynamo Theory*, Wiley

[108] Ruzmaikin, A.A., Shukurov, A.M., Sokoloff, D.D., 1988, *Magnetic Fields of Galaxies*, Kluwer

[109] Sakamoto, K., 1996, ApJ, 471, 173

[110] Sandage, A., Bedke, J., 1988, *Atlas of Galaxies Useful for Measuring the Cosmological Distance Scale*, NASA SP-496, US. Govt. Printing Off., Washington D.C.

[111] Sano, T., Inutsuka, S.I., Miyama, S.M., 1998, ApJ, 506, L57

[112] Sellwood, J.A., Balbus, S.A., 1999, ApJ, 511, 660

[113] Shakura, N.I., Sunyaev, R.A., 1973, A&A, 24, 337

[114] Shalybkov, D., Rüdiger, G., 2004, *MHD Couette Flows: Experiments and Models*, Proc. of the conference in Acitrezza (Catania, Italy), Eds.: R. Rosner et al., New York: American Institute of Physics, 733, p. 165

[115] Simard-Normandin, M., Kronberg, P. P., 1979, Nature, 279, 115

[116] Sofue, Y., 1996, ApJ, 458, 120

[117] Soida, M., Beck, R., Urbanik, M., Braine, J., 2002, A&A, 394, 47

[118] Spangler, S.R., 1999, *Plasma Turbulence and Energetic Particles in Astrophysics*, Proc. of the International Conference Cracow, Eds.: M. Ostrowski et al., Obserwatorium Astronomiczne, Uniwersytet Jagiellonski Kraków, p. 388

[119] Spangler, S.R., 1999, ApJ, 522, 879

[120] Spitzer, L.J., 1962, *Physics of fully ionized gases*, New York Interscience Publishers (2nd edition)

[121] Stone, J.M., Norman, M.L., 1992, ApJS, 80, 791

[122] Stutzki, J., Bensch, F., Heithausen, A., Ossenkopf, V., Zielinsky, M., 1998, A&A, 336, 697

[123] Thierbach, M., Klein, U., Wielebinski, R., 2003, A&A, 397, 53

[124] Thornley, M., Mundy, L.G., 1997, ApJ, 490, 682

[125] Torkelsson U., Brandenburg A., 1994a, A&A, 283, 677

[126] Torkelsson U., Brandenburg A., 1994b, A&A, 292, 341

[127] Tüllmann, R., Dettmar, R.J., Soida, M., 2000, A&A, 364, L36

[128] Urpin, V.A., Brandenburg, A., 1998, MNRAS, 294, 399

[129] Vainshtein, S.I., Cattaneo, F., 1992, ApJ, 393, 165

[130] Velikhov, E., 1959, Sov. Phys. JETP, 9, 995

[131] Valleé, J. P., 1997, Fundamentals of Cosmic Physics, 19, 1

[132] Vallejo, O., Braine, J., Baudry, A., 2002, A&A, 387, 429

[133] Vishniac, E.T., Diamond, P., 1989, ApJ, 347, 435

[134] Vishniac, E.T., Jin, L., Diamond, P., 1990, ApJ, 365, 648

[135] Ziegler, U., 1996, A&A, 313, 448

Acknowledgments

It is a pleasure for me to thank all those who made this work possible: Prof. Dr. G. Rüdiger for offering me the opportunity to work on this subject; Prof. Dr. G. Rüdiger and Dr. D. Elstner for the excellent school in physics and numerical research; Dr. R. Beck for the impressive radio data, as well as for the discussions in Bonn from which I gained most of my knowledge of the galactic magnetic fields; Prof. Dr. L. Kitchatinov and Prof. Dr. K. Otmianowska-Mazur for many fruitfull hours of discussions which we had; Dr. H.-E. Fröhlich for being a patient and carefull editor; all my colleagues and many others for helping and motivating me in creating this work.

I thank Dr. H. Klahr and Prof. Dr. Th. Henning for their support at MPIA Heidelberg.

I thank Merlin for strong spiritual support during the last four years.

The research has been done with financial support from DFG grant EL 18412.